INVESTIGATION OF BIODEGRADABLE IRON-MANGANESE ALLOYS WITH VARIOUS POROSITY

by

Sabrina Huang

A Dissertation

Submitted to the Faculty of Purdue University

In Partial Fulfillment of the Requirements for the degree of

Doctor of Philosophy

School of Materials Engineering

West Lafayette, Indiana

August 2019

THE PURDUE UNIVERSITY GRADUATE SCHOOL
STATEMENT OF COMMITTEE APPROVAL

Dr. Lia Stanciu, Chair

> School of Materials Engineering

Dr. Carlos Martinez

> School of Materials Engineering

Dr. Eric Nauman

> School of Mechanical Engineering

Dr. Meng Deng

> School of Agricultural & Biological Engineering

Approved by:

> Dr. David Bahr
>
> > Head of the Graduate Program

In dedication to my strong and beautiful Mom, Who loves me with no return.

ACKNOWLEDGMENTS

First, I would like to acknowledge my advisor Dr. Lia Stanciu for all her support and encouragement throughout my entire Ph.D. life. The flexibility I received allowed me to explore a variety of research directions and broaden my horizons. Thank you for guiding me to plan the research goals and inspiring me all the way. I also want to thank Dr. Carlos Martinez for giving me advices in future career and always welcoming me when we ran into each other. Special thanks to Dr. Eric Nauman for his valuable insights into my research. To Dr. Meng Deng, thank you for instructing me the class material and challenging me in critical thinking. I also would like to thank all the other professors and staff in the MSE department and in the Birck Nanotechnology Center for training me or providing me help for my research work.

Furthermore, I want to thank all my friends and colleagues I have met in Greater Lafayette. Without your sincere support, cheer, and consolation, I could not even make to this far. To Azi, Shikhar, Hector, Xiaolong, and Ramazon, I am so grateful we got to know one another since the first year of my Ph.D. and throughout the years we all developed strong skills in our specific area of research. I know the bonding between us would never go away and I wish you all the best after graduation. To Hyungyung, Sri, Tongjun, and Jaehun, I enjoy saying "good morning" to you in Korean, Hindi, and Chinese that always delighted me in the beginning of the day, and I am grateful to have so many pleasant daily interactions with you that for sure I will miss a lot. To Michael, Ana, Pengyu, and Susana, thank you for constructive suggestions and assistance in my research work and we all made our lab clean and well organized together.

Last but not least, I would like to thank my church family for all prayers and encouragement that pump me up through the stressful but joyful moments along my adventures in the graduate school. To Elaine, Tiffany, Teresa, Kaoling, Abby, Shenrui, Gyenam, Katherine, and Joann, thank you for all moral and physical supports! Finally, I would like to thank my entire family, especially my mother Mei-Fen, for always being my strong hold backing me up whenever and wherever I go, encouraging me during the hard time and hurrah for me even on a simple tiny thing that I accomplished. Nothing else I can do in return. To everyone else, I am proudly present my thesis.

TABLE OF CONTENTS

LIST OF TABLES

LIST OF FIGURES

NOMENCLATURE

α	ferrite (BCC) phase
α	rake angle
α-MEM	alpha minimum essential medium eagle modification
γ	austenite (FCC) phase
ε	martensite (HCP) phase
ρ	density (g/cm^3)
ACR	accumulative cryo-rolling
ANOVA	analysis of variance
A_S	austenite start temperature
ASTM	American Society for Testing and Materials
BCC	body-centered cubic crystal structure
BMSC	bone marrow stromal cell
BSE	back scattered electron
CR	corrosion rate
CR_{i30}	corrosion rate obtained from the immersion mass loss test after 30 days of incubation
CR_p	corrosion rate obtained from the potentiodynamic polarization test
DD	drop deposition
ECM	extracellular matrix
E_{corr}	corrosion potentials
EDS	energy dispersive (x-ray) spectroscopy
EW	equivalent weight
FBGCs	foreign body giant cells
FBS	fetal bovine serum
FCC	face-centered cubic crystal structure
FTIR	Fourier-transform infrared spectroscopy
GPa	gigapascal (109 N/mm^2)
HA	hydroxyapatite
HBSS	Hank's balanced salt solution

HCP	hexagonal-closed packed crystal structure
i_{corr}	corrosion current density
IL-1β	interleukin-1β
IL-6	interleukin 6
INT	iodonitro-tetrazolium violet
ISO	International Organization for Standardization
K_1	3.27×10^{-3} mm g μA^{-1} cm^{-1} yr^{-1}
K_2	8.76×10^4 mm hr cm^{-1} yr^{-1}
LDH	lactate dehydrogenase
LSM	large-strain machining
MC3T3-E1	murine calvarial preosteoblast cell
MG63	human fibroblast cell
mmpy	millimeters per year (unit of corroded surface erosion rate)
MPa	megapascal (106 N/m^2)
MRI	magnetic resonance imaging
M_S	martensite start temperature
MTS	3-(4,5-dimethylthiazol-2-yl)-5-(3-carboxymethoxyphenyl)-2-(4-sulfophenyl)-2H-tetrazolium, inner salt
NH$_4$HCO$_3$	ammonium bicarbonate
NIH3T3	murine fibroblast cell
OD	optical density
PBS	phosphate-buffered saline
pH	(p[H]) negative logarithm of the hydrogen ion activity compared to hydroxide activity
PM	powder metallurgy
RDA	recommended dietary allowance
ROS	reactive oxygen species
rpm	revolutions per minute
SBF	simulated body fluid
SC	spin coating
SCE	saturated calomel electrode

SEM	scanning electron microscopy
SS316L	medical grade stainless steel (16-18.5 wt.% Cr, 10-14 wt.% Ni, 2-3 wt.% Mo, < 2 wt.% Mn, < 1 wt.% Si, < 0.045 wt.% P, < 0.03 wt.% S, and < 0.03 wt.% C, balance Fe)
TC50	ion concentration at which cellular activity remains in half
TCPS	tissue culture polystyrene
Ti6Al4V	medical grade titanium alloy composed of 6 wt.% aluminum, 4 wt.% vanadium, balance titanium
TNF-α	tumor necrosis factor-α
UL	tolerable upper intake level
XRD	x-ray diffraction

ABSTRACT

Author: Huang, Sabrina, M. PhD
Institution: Purdue University
Degree Received: August 2019
Title: Investigation of Biodegradable Iron-Manganese Alloys with Variable Porosity
Committee Chair: Lia Stanciu

Bioresorbable iron-manganese (Fe-Mn) alloys are considered as a new class of biomaterials for the development of orthopedic fixation devices due to their promising mechanical properties, comparable to the human cortical bone, and the ability to degrade in the physiological environment and release small quantities of metallic ions/particles that are absorbable by the host. The greatest challenge for developing an ideal resorbable Fe-Mn alloy is to increase the degradation rate of the alloy without compromising the alloy biocompatibility, that is, causing zero or minimal local and systemic toxicity to the tissue. Another challenge is to improve osteo-integration through inducing a cascade of events leading to tissue ingrowth.

The incorporation of porosity into the Fe-Mn alloys aimed to increase the corrosion rate and to provide the three-dimensional structure for cellular activity and nutrient transport. The Fe-30wt.%Mn alloys with 0-, 5-, 10-, and 60-volume percent porosity were produced through the space holder technique in powder metallurgy. The space-holder material, ammonium bicarbonate (NH_4HCO_3), was sieved to a particle size ranging 355~500 µm. The microstructures and mechanical properties of the alloys, as well as the influence of the degree of porosity on the alloy corrosion rates comparing to the concentrations of the degraded metal ions were investigated. Although the Fe-30Mn alloys containing 60-vol% porosity exhibited the lowest average ultimate compressive strength of 381 MPa among the tested groups, they were still mechanically stronger

than a typical human wet compact bone. Furthermore, the alloys had the highest average corrosion rate of 0.98 ± 0.20 mm/year, compared to 0.13 ± 0.07 mm/year for the non-porous Fe-30Mn alloys. Nevertheless, the extract from the 60%-pore group had a cytotoxicity effect to the bone marrow stem cells (BMSCs) at an average normalized cell viability of 58%, which was below the standard viability of 70%, considered as cytotoxic in the indirect cytotoxicity study. The cytotoxicity study also corresponded to the highest level of transition metal ions Mn^{2+} released into the media for the 60%-pore group at an average ion released rate of 7 mg/day, compared to the other groups presenting similar Mn^{2+} released rates about 4 mg/day after 1 day of incubation. The extreme case of the 60%-pore group demonstrated the tradeoff between the corrosion rates and biocompatibility. On the other hand, the 10%-pore group showed an average ultimate compressive strength of 737 MPa comparable to the stainless steel 316L, an average corrosion rate of 0.260 ± 0.09 mm/year, which was 2-fold higher than the non-porous group, and an average cell viability of 86% close to the non-porous group. It is promising based on the above results, however, the osteo-integration of the 10%-pore group in terms of cell-to-cell and alloy-to-cell interactions was not ideal.

It is hypothesized that coating collagen on the Fe-30Mn alloys can improve osteo-integration or biochemical events promoting cell adhesion, migration, and proliferation, as the alloy degrades. After preparing collagen coating on the Fe-30Mn alloys via spin coating with the spin speed of 4250 rpm for 30 seconds, a potentiodyanmic polarization test and a direct cytotoxicity test on four Fe30Mn groups: non-porous and 10% porosity, with and without collagen coating, were conducted. The average cell count and size for the experimental Fe-30Mn and control Ti6Al4V groups over 72 hours were also evaluated. There was no significant difference between the collagen-coated and non-coated groups in corrosion rates, yet a significant decrease from the porous non-coated group

to the porous collagen-coated group in the cytotoxicity level (15% to 9%, respectively) was found. The cell morphology on the porous non-coated Fe-30Mn group displayed round shape, whereas that on the porous collagen-coated Fe-30Mn group displayed flattened spreading. Furthermore, the porous collagen-coated Fe30Mn group showed significant increase in the average cell count (2376 $\pm$ 401 cell/mm^2) and size (66 $\pm$ 10 µm) within 24 hours, nearly three-fold in count and 1-fold in size compared to the porous non-coated Fe-30Mn group. The study showed that the collagen coating significantly increased the initial cell viability and adhesion for both the porous and non-porous groups without impeding their degradation rates.

With the incorporation of porosity and surface coating with Type I collagen, Fe-30Mn alloys could become the next generation transient load-bearing medical devices. However, investigations of alloy processing, including powder production, powder size and shape for porosity control, as well as spin coating parameters (spin speed and spin time for homogeneous coating), and the qualitative and quantitative evaluation of the corrosion particles are encouraged in the future. Also, long-term *in vivo* studies to mimic human physiological environment are encouraged.

CHAPTER 1.   INTRODUCTION

1.1   Metallic Implants in Biomedical Fields

For over a century, metals have been primarily used for implants in the medical fields of cardiovascular, orthopedic, dentistry, craniofacial, and otolaryngology [1]. Their capability of providing extensive strength and ductility after implantation, normally undergoing cyclic or static loading, marks their superiority over ceramics and polymers, especially for some orthopedic applications. Numerous studies have evolved metallic implants that are non-toxic and allergy-free *in vivo* [2–7]. Typically, metallic biomaterials are high in density to support sequential loads and non-magnetic to be compatible with magnetic resonance imaging (MRI) and X-ray imaging. Classical metallic implants include stainless steel SS316L, cobalt (Co) alloys (i.e. CoCrMo), titanium (Ti) alloys (i.e. Ti6Al4V), gold (Au) and silver (Ag) that have been used since antique times. 316L stainless steel is strong and resistant to corrosion when alloyed with about 18 wt.% chromium (Cr), 8 wt.% nickel (Ni), and a little amount of molybdenum (Mo) [8]. Stainless steel 316L is often considered as a standard when compared with new developing biomaterials since it is vastly practiced in clinical use for various implant fields. Other metallic materials target different applications. Co alloys are specifically used for orthopedic joint implants as they display excellent wear resistance. Lightweight Ti alloys are generally employed as bone fixation devices (plates, screws, pins) because they are tough and more flexible than SS316L, which reduces bone loss from the effect of stress shielding [9]. Alloys combined of Au and Ag with a little amount of zinc (Zn) and tin (Sn) exhibit great ductility and castability in dentistry [10]. Besides commercial metallic implants, biodegradable metals have been more recently proposed for use in temporary implants.

1.2   Biodegradable Metals

Biodegradable, or bioresorbable, materials are temporary, nontoxic, and capable of being degraded and reabsorbed in human body within a designated period. Some of these degradable materials are suitable for fracture repair and fixation devices, as well as for temporary cardiovascular stents. Due to an increasing elderly population and number of road accidents, the market for orthopedic trauma fixation devices has increased tremendously [11]. Scholars are working at the frontier of medical science to develop bioresorbable materials that require no secondary implant-removal surgery after healing to reduce persistent pain from material stress shielding and fatigue failure.

The ideal bioresorbable metal requires: (1) zero or minimal toxicity, (2) strong structural support, (3) adequate degradation and resorption rates, and (4) native tissue ingrowth. Other than mechanical properties, corrosion behavior, and biocompatibility of materials, biological environment parameters such as body temperature, level of pH, and local or systemic inclusions also affect the performance of materials after implantation. For fixation devices that require significant mechanical properties, biodegradable metals are more suitable than biodegradable polymers owing to their strong structural support and high fatigue limit. Present biodegradable metals investigated are either iron-based or magnesium-based alloys [2,12–16].

Iron and magnesium (Mg) already exist in minor quantities within the human body, which highlights them as highly biocompatible at low concentrations [12]. Pure iron is more attractive than Mg due to its superior mechanical properties and stability when contacted with human plasma; Mg corrodes and reacts with water rapidly, creating undesirable hydrogen gas that prolongs tissue inflammation after implantation [13,17]. Iron also serves as a component of hemoglobin, a complex protein in erythrocytes, which plays a vital role in transporting oxygen from plasma to

surrounding tissues [18]. Previous *in vivo* studies of stents composed of pure iron displayed no pronounced inflammation or significant toxicity at local or systematic tissues, making pure iron a feasible material for a degradable medical implant [14,15]. Nevertheless, degradation rates of pure iron *in-vivo* were slower than those expected *in vitro*, in research concentrated on developing new methods to improve their corrosive behaviors. An effective solution is to alloy manganese (Mn), an essential element for bone formation and calcium absorption, with pure iron to accelerate the overall degradation rate [12,19].

1.3   Structure, Properties and Processing of Fe-Mn Alloys

Pure iron is ferromagnetic and exhibits a body-centered cubic (BCC) structure known as α-iron or ferrite. With the addition of Mn, its BCC structure transforms into a face-centered cubic (FCC) structure, known as γ phase or austenite. In the Fe-Mn binary system, as shown in Figure 1.1, a martensitic transformation between the γ phase and the metastable hexagonal closed-packed (HCP) structure, also called ε phase or martensite, is of most interest [20]. This martensitic transformation is reversible at starting temperatures upon cooling M_S (i.e. $\gamma \rightarrow \varepsilon$) and heating A_S (i.e. $\varepsilon \rightarrow \gamma$) [21,22].

Both M_S and A_S decrease as Mn content increases between the composition of 13 wt% and 27 wt% Mn [23]. Alloys with over 30 wt.% Mn are completely austenitic, however, the diffraction peaks of the ε phase can be observed after plastic deformation [24]. When plastic deformation occurs, stacking faults in the γ matrix act as nucleation sites for the ε phase [25]. Upon plastic deformation of quenched Fe-Mn alloys, new ε phase forms and the grains of the existing ε phase grow. Hermawan et al. evaluated Fe-Mn alloys with Mn content that ranged from 20 wt.% to 35 wt.% as potential candidates for use in biodegradable stents. In Figure 1.2, Fe-Mn with 20 wt.% and 25 wt.% Mn content reveal a duplex structure of γ and ε phases after quenching but turned into a

single ε phase after cold rolling with 20% thickness reduction, whereas Fe-30Mn and Fe-35Mn contained a single γ phase after quenching but after cold rolling, both γ and ε phases are observed [24].
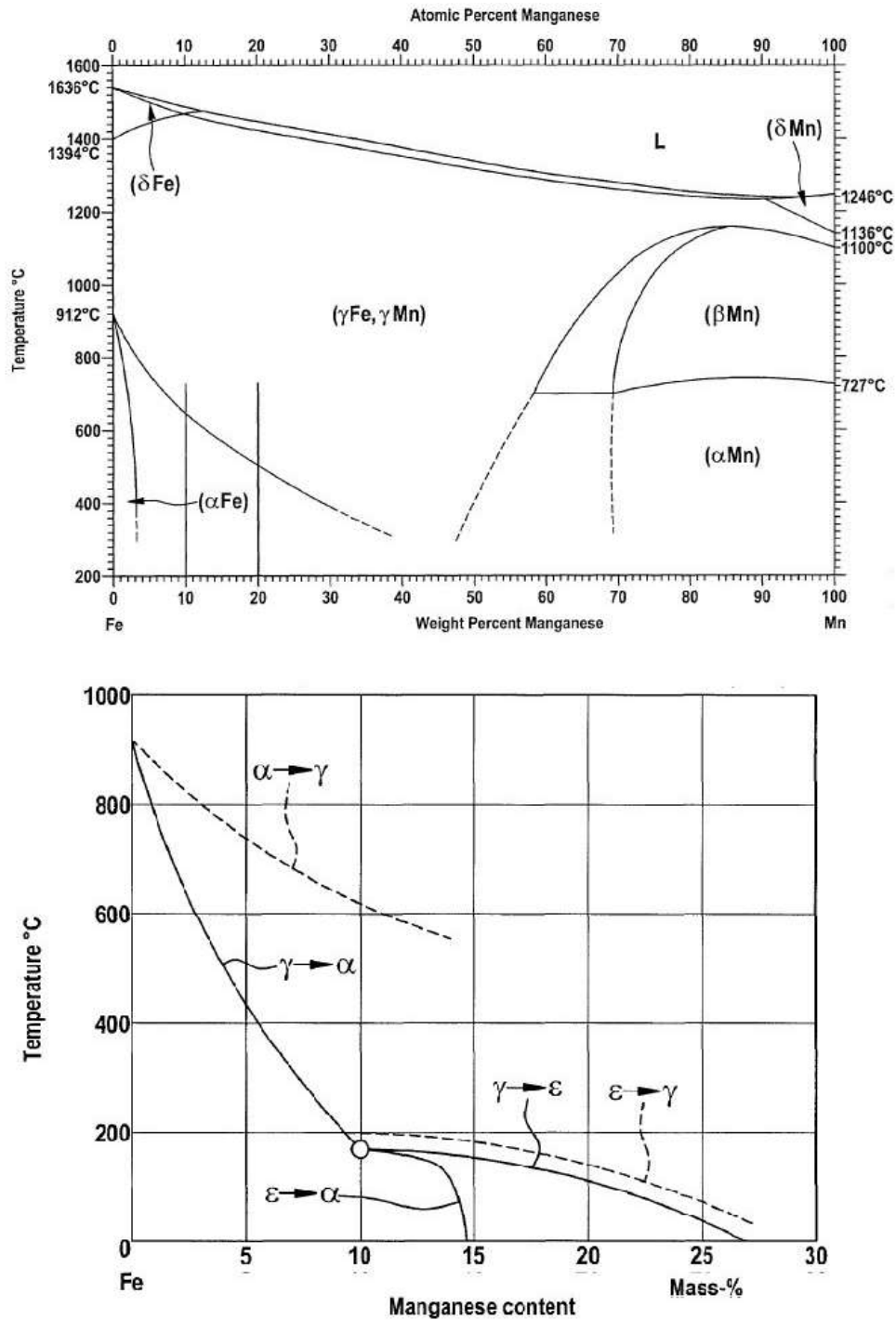
Figure 1.1 Phase Diagram of Fe-Mn Binary System [20]
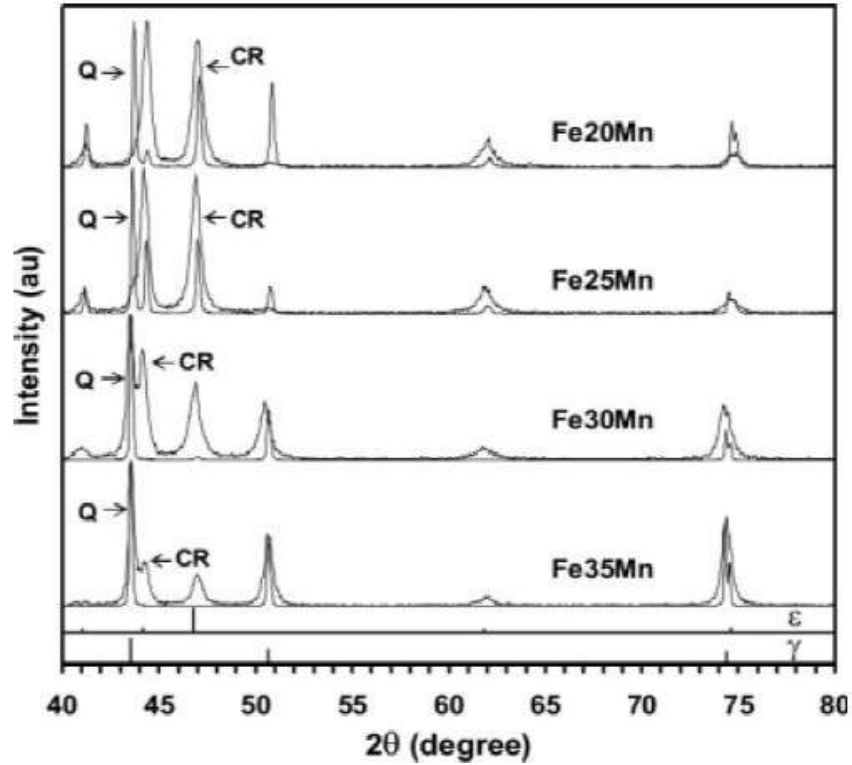
Figure 1.2 X-ray diffraction patterns of Fe-Mn alloys after quenching (Q) and 20% cold rolling (CR) [24]

The microstructure of those specimens showed that the γ phase is prevalent in alloys having a higher Mn content (30 wt.% and 35 wt.%) while in alloys with 20 wt.% and 25 wt.% Mn, only the ε phase exists. The ε phase is well known for its highest density among all phases in the Fe-Mn system [26]. Since this martensitic phase is harder and denser than the γ phase, one can explain the increasing ductility with the increasing Mn composition. In Table 1.1, the yield strength of Fe-Mn alloys ranged from 234 MPa for Fe-35Mn to 421 MPa for Fe-20Mn and the elongation at break ranged from 7.5% for Fe-20Mn to 32% for Fe-35Mn. There is a slight increase of ductility of Fe-20Mn alloys, compared to Fe-25Mn alloys, where stress relaxation mechanism takes place via plastic deformation as well as the formation of α^0 phase [27]. Large grains of martensitic ferrite induce stress relaxation, and hence enhance the elongation of Fe-20Mn alloys.

Table 1.1 Mechanical properties of Fe-Mn alloys in comparison to SS316L and Ti4Al4V alloys. The values in parenthesis are standard deviation. Data adapted from Heramawan et al. [24] and ASTM handbooks [28, 29]

Material	Phase	Ultimate Strength (MPa)	Yield Strength (MPa)	Maximum Elongation (%)	Hardness (Rockwell A)
Fe-20Mn	$\gamma + \varepsilon$	702 (11)	421 (27)	7.5 (1.5)	59 (1)
Fe-25Mn	$\gamma + \varepsilon$	723 (19)	361 (33)	4.8 (0.4)	56 (1)
Fe-30Mn	γ	518 (14)	239 (13)	19.0 (1.4)	40 (1)
Fe-35Mn	γ	428 (7)	234 (7)	32.0 (0.9)	38 (2)
SS316L [28]	γ	490	190	40	–
Ti6Al4V [29]	$\alpha + \beta$	860	795	10	–

When alloyed with more than 29 wt.% Mn, Fe-Mn alloys exhibit antiferromagnetic behavior [26, 30]. This can be a great advantage for magnetic resonance imaging in clinical use. Furthermore, alloys of Fe-30Mn and Fe-35Mn have similar mechanical properties compared to SS316L, which marks them as good candidates for biodegradable materials. Fe-Mn alloys can be fabricated either through traditional ingot metallurgy such as casting with subsequent cold/hot working and mechanical machining [16, 31] or powder metallurgy (PM) such as sintering and metal injection molding (MIM) [19, 32, 33]. PM is a modern state-of-the-art technique to create alloys or composites through metallic powders and is economically used for large manufacturing of complex structures [34]. The beauty of using PM is that porous structures of Fe-Mn alloys can be obtained. These open pores serve as a good platform for cell migration and proliferation on the material scaffold, which in turn improves bone ingrowth for orthopedic fixation devices [32,33]. However, impurities such as manganese oxide (MnO) and the inferior weak mechanical properties induced by porosity need to be considered when developing Fe-Mn alloys through PM [19,32].

1.4   Degradation Behavior of Fe-Mn Alloys

Biodegradable metallic materials are designed to resorb over an appropriate period of time at specific implanted sites. For cardiovascular resorbable scaffolds, the desired controlled degradation time is within 6 to 12 months, and for orthopedic resorbable scaffolds, the desired controlled degradation time requires at least 6 months [35, 36]. When an Fe-Mn alloy is in contact with a physiological environment, the physiological environment acts as an electrolyte in which electrochemical reactions take place; this process is also known as corrosion. The electrochemical mechanism between the Fe-Mn alloy and the electrolyte involves the anodic reaction of metals (Eqs. 1-2) and the cathodic reaction (Eq. 3) of the electrolyte. These corrosion reactions result in the formation of oxides, hydroxides as well as other inorganic products (Eq. 4).

$$Fe \rightarrow Fe^{2+} + 2e^{-} \qquad (1)$$

$$Mn \rightarrow Mn^{2+} + 2e^{-} \qquad (2)$$

$$2H_2O + O_2 + 4e^{-} \rightarrow 4OH^{-} \qquad (3)$$

$$M^{n+} + nOH^{-} \rightarrow M(OH)_n \qquad or \qquad nMO.nH_2O \qquad (4)$$
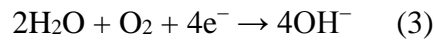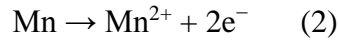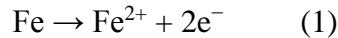
At the surface of an Fe-Mn alloy, galvanic corrosion occurs due to potential differences between the matrix interface (grain boundaries) and the alloy/electrolyte interface. Electrons released from anodic reactions (Eqs. 1 and 2) are depleted by the dissolved oxygen from the electrolyte that undergoes the reduction (cathodic) reaction (Eq. 3) where hydroxyl ions form. Positive metallic ions released from Eqs. 1 and 2 subsequently react with the hydroxyl groups and create a layer of

hydroxides on the surface of the alloy Eq. 4). This passive layer is often an inhibitor of further degradation of the implant material. However, since the hydroxide layers cover the surface unevenly, pitting corrosion takes place. This localized pitting results from the hydrolysis of metal chlorides, which are products of metal ions from the alloy and chlorine ions (Cl^-) from the aggressive physiological environment. Equation 5 depicts the reaction between iron ions and Cl^- during pitting because iron is the primary material of the Fe-Mn alloy. Composites of hydroxide and hydrogen chloride form when pitting proceeds.

$$Fe^{2+} + 2Cl^- \rightarrow FeCl_2 + H_2O \rightarrow Fe(OH)_2 + HCl \qquad (5)$$
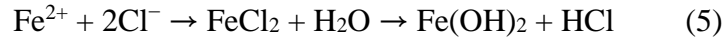
Inorganic composites, such as calcium and phosphorus, also accumulated on the surface of the alloys after pitting because of localized alkalization [37]. These agglomerates display an amorphous coral structure that are similar to hydroxyapatite (HA), which is a fundamental component of the bone matrix that conducts the ingrowth of hard tissues.

Since corrosion is an electrochemical reaction between anode and cathode, electrons flow between the grain boundary of the alloy (anode) and the immersed electrolyte (cathode), resembling the degradation behavior of Fe-Mn alloys. Consequently, the corrosion current density (i_{corr}) can be measured via conducting a potentiodynamic polarization experiment in which the degradation rate of the specimen can then be calculated from the ASTM G59-97 standard (Eq. 6) [38]:

$$CR = K_1 \frac{i_{corr} EW}{\rho} \qquad (6)$$

where CR is the degradation rate of the alloy in millimeters per year (mmpy), $K_1 = 3.27 \times 10^{-3}$ mm g μA^{-1} cm^{-1} yr^{-1}, i_{corr} stands for the current density in mA/cm^2, ρ is the density of the sample in g/cm^3 and EW is the equivalent weight of the sample in grams.

Static impedance measurement can also determine the corrosion rate of Fe-Mn alloys based on the mass loss of alloys after immersion over a period of time. Followed by the ASTM G31-72 standard [39], the mass loss equation is:

$$CR = K_2 \frac{W}{At\rho} \qquad (7)$$

where CR is the corrosion rate (mmpy), $K_2 = 8.76 \times 10^4$ mm hr cm^{-1} yr^{-1}, W stands for the mass loss in grams, A is the surface area of the alloy exposed to the tested solution in cm^2, t is the immersed time in hours, and ρ is the density of the alloy in g/cm^3.

By utilizing both polarization and immersion corrosion tests, the degradation rate of Fe-Mn alloys varies based on the weight percentage of Mn content, the processing technique, as well as the immersion solution. In Table 1.2, the average corrosion rate of sintering Fe-20Mn alloys and Fe-35Mn alloys is 1.3 mmpy and 0.7 mmpy, respectively, when tested in a Hank's balanced salt solution (HBSS) [24]. The higher degradation rate observed in Fe-20Mn alloys is predictable because Fe-20Mn alloys contain both ε and γ phases while Fe-35Mn alloys contain only the γ phase. This duplex structure intensifies the initiation of galvanic corrosion and also the intergranular corrosion at grain boundaries, which increases the corrosion rate.

Table 1.2 Corrosion rates of Fe-Mn alloys in comparison to pure iron

Material	Processing	Solution	i_{corr} (μA/cm^2)	CR (mmpy)
Fe-20Mn [31]	cast	osteogenic media	75.8	0.9
Fe-20Mn [24]	sintering	HBSS	113	1.3
Fe-33Mn [31]	cast, LSM α=0°	osteogenic media	72.5	0.8
Fe-33Mn [31]	cast	osteogenic media	30.2	0.3
Fe-35Mn [24]	sintering	HBSS	55	0.7
Fe-35Mn [32]	sintering, 20 vol% spacer	SBF	284	5.26
Pure Iron [31]	annealed	osteogenic media	4.38	0.05
Pure Iron [24]	annealed	HBSS	16	0.2

LSM = large-strain machining, α = rake angle, SBF = simulated body fluid. Data adapted from [24, 31, 32]

Even within the same composition, the degradation rate of Fe-Mn alloys can be greatly improved through plastic deformation and porosity incorporation. It is found that Fe-33Mn alloys degrade from 0.3 mmpy to 0.8 mmpy after being subjected to large strain machining (LSM) with a rake angle (α) of 0° [31]. Fe-35Mn alloys with 20 vol.% porogen, ammonium bicarbonate (NH_4HCO_3), present an average corrosion rate of 5.26 mmpy, a much higher degradation rate compared to non-porous sintered Fe-35Mn alloys (0.7 mmpy) [32]. However, the increased corrosion rate lowers the mechanical properties of the alloy. Balancing both the degradation rate and mechanical properties of Fe-Mn alloys requires further investigation to optimize a fracture fixation device. One can notice that the degradation behavior of Fe-Mn alloys also depends on the solution being immersed in. The average corrosion rate of cast Fe-20Mn alloys is 0.9 mmpy when tested in an osteogenic cell culture medium [40], while the average corrosion rate of sintered Fe-20Mn alloys is 1.3 mmpy when tested in HBSS [24]. The osteogenic media contain 10-vol.% of fetal bovine serum (FBS) that hinders the degradation rate of the alloy because the alloy surface is covered by the proteins from FBS. Nevertheless, no evaluation of proteins deposition on Fe-Mn alloys has been studied so far to the author's knowledge.

Notice that the lowest degradation rate of Fe-Mn alloys is still larger than the degradation rate of pure iron in Table 1.2. Adjusting the level of Mn content and the amount of porosity, along with plastic deformation of the alloy can optimize the degradation rate of Fe-Mn alloys and allow for a desired time frame of mechanical stability. According to their microstructure, mechanical properties, and degradation behaviors, Fe-Mn alloys are promising implant candidates for metallic biodegradable fixation devices.

1.5   Biological Interactions between Fe-Mn Alloys and Cells

In the mid-20th century, biomaterials that elicit zero or little host response after implantation were considered biocompatible. Such bioinert materials were selected because they were functionally matched with the host tissue and were widely used for industrial applications. However, material being bioinert is not sufficient reason for clinical use, since implant failure due to other issues unrelated to reactivity has catastrophic results in terms of the effect on the host tissues and the performance for the intended application. Therefore, the biocompatibility of a material was redefined as "the ability to fulfill a proper host response in a specific application," which has been widely accepted since introduced by Dr. Williams in 1987 [41].

There are several reactions that occur following implantation that proceed according to a sequential time-line of events, including thrombus formation, acute and chronic inflammation, immune response, foreign body reactions, and fibrous capsule formation [42]. The first host response starts from plasma proteins adsorption onto the surface of the implant immediately after the injury. The cascade of protein adsorption and desorption, known as the Verman effect [43], is the initiator of thrombus formation resulting from platelet adhesion and accumulation, and in turn triggering the migration of neutrophils and monocytes that portray inflammation. Macrophages, the phagocytic

cells derived from monocytes, infiltrate the inflammatory site and fuse into foreign body giant cells (FBGCs). These FBGCs are great indicators of the foreign body response because they attack the implant surface by releasing reactive oxygen species (ROS), which consist of hydroxyl radicals (OH·) and superoxide anions ($O_2^-·$) [44]. Notice that ROS are surplus oxidative agents that facilitate the oxidation process upon corrosion. Consequently, metal ions released due to the cathodic reaction accelerates, which, once absorbed into cells, alternates cellar behaviors including their morphology, proliferation, and differentiation. The high level of metal ions may ultimately result in necrosis. Cellular activity is strongly affected by the physical and chemical characteristics of the metal implant. Different compositions of manganese contents as well as processing of Fe-Mn alloys are of most importance to invoke positive cellular responses. It was found that the murine fibroblast cells (NIH3T3) expressed the highest relative metabolic activity when they were exposed to Fe-30Mn powders at a concentration of 1 mg/ml, as shown in Figure 1.3 [37]. However, the study measured cellular metabolic activities with the presence of alloys in powder forms, which may cause discrepancies when practiced in bulk. Standards such as American Society for Testing and Materials (ASTM) and International Organization for Standardization (ISO) are necessary to conduct cytotoxicity tests for Fe-Mn alloys in vitro and in vivo [45].
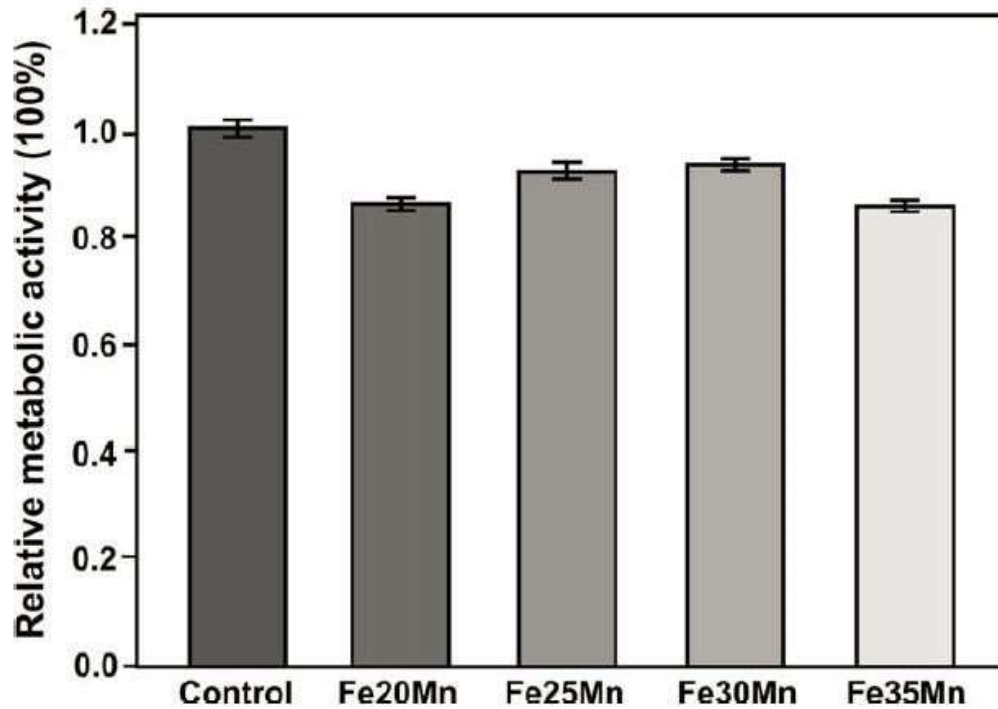
Figure 1.3 Relative metabolic activities of 3T3 fibroblasts in the presence of Fe-Mn alloy powders with various manganese contents [37]

Chou et al. observed a higher murine calvarial osteoblastic cell (MC3T3-E1) density after 3 days of direct culture with 3-D printed Fe-30Mn specimens compared to that of culture with culture plastic, as shown in Figure 1.4, indicating good biocompatibility of Fe-30Mn alloys [33]. Nevertheless, difficulties in controlling parts shrinkage and open porosity during sintering hindered the mechanical properties and manufacturing consistency of 3-D printed Fe-30Mn. It is necessary to develop controllable porosity of Fe-Mn alloys to improve cell migration and proliferation without mechanical failure, as the interconnected porosity enhances continuous bone in-growth vital to tissue regeneration.
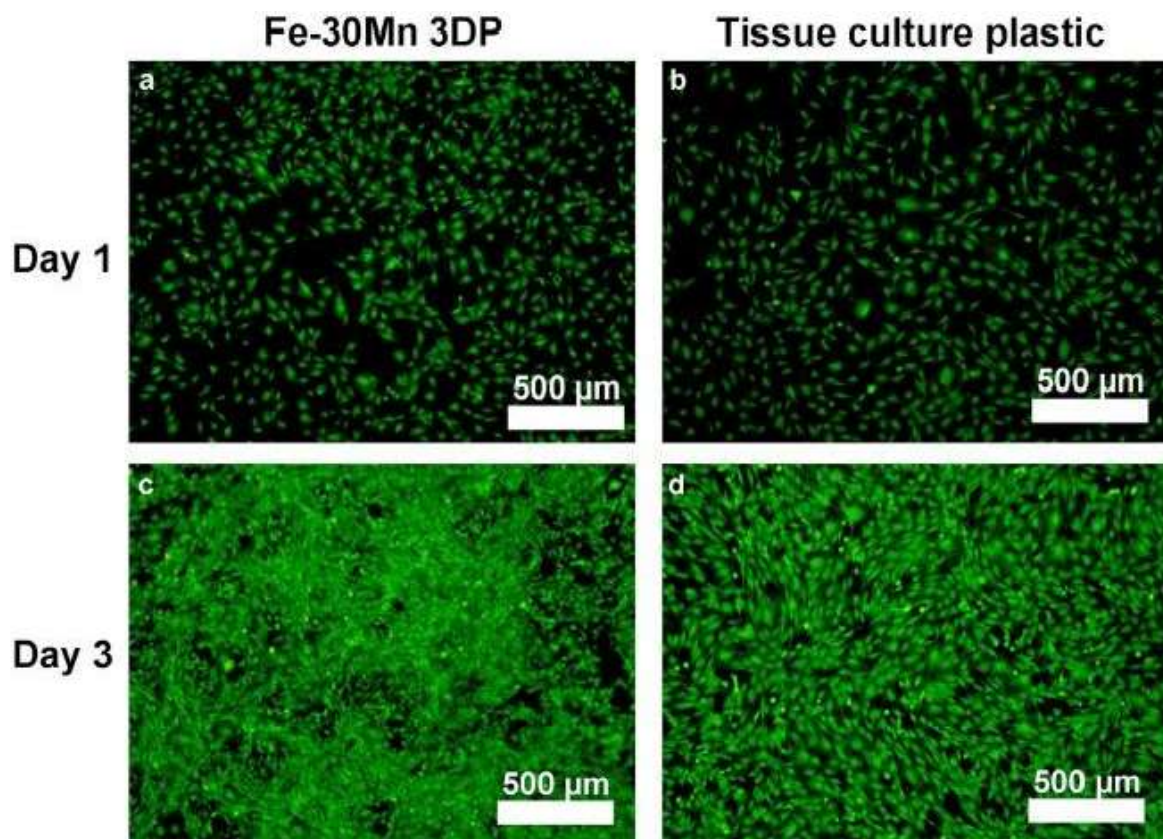
Figure 1.4 Fluorescent images of MC3T3-E1 cells attached after 1 and 3 days culture on (a,c) 3-D printed Fe-30Mn and (b,d) tissue culture plastic [33]

Besides porosity, cellular activity such as releasing small molecules like growth factors and enzymes, as well as interacting with proteins and the material matrix also influences the degradation rate of a biomaterial. Some types of cells such as macrophages and osteoclasts can even resorb ions/particles leaching from the bulk matrix, adding complexity of degradation parameters in the biological environment. The definition of biocompatibility of a material thereafter refers to "the ability to induce proper cellular activity such as cellular adhesion, proliferation, migration, and distribution of inter/intra-cellular molecular signaling systems that promote tissue ingrowth without eliciting undesirable local or system host responses" from the tissue engineering standpoint [46]. A combination of matrix structure, degraded ions/particles, and

cellular activities cooperated within the matrix-host environment needs to be well investigated to obtain the optimum degradation rate of Fe-Mn alloys.

Currently, there is no cell-based study of Fe-Mn alloys regarding matrix resorption through osteoclasts, derived from monocyte/macrophage lineages, and to hard tissue mineralization through osteoblasts, derived from bone marrow stem cell lineages. Active osteoclasts prevail as the matrix exhibits a rough surface compared to smooth topography [47]. There are two types of metal degraded products: particles and soluble (ionic) debris. Metal wear particles typically range with size less than 1 um, which can be swallowed by cells (pinocytosis) without phagocytosis and hinder the differentiation of macrophages into osteoclasts [47–50]. Soluble metal ions with ion concentrations expressed in mol per liter (mol L^{-1}) or parts per million (ppm) bind to serum proteins and disseminate into local and systemic environments. A high concentration of metal ions elicits tissue inflammation, immunologic response, and cell necrosis. It is important to control metal ion release below the ion concentration at which cellular activity remains in half, also known as TC50, for the design of Fe-Mn alloys. Iron, with TC50 about 100-1000 µM, is an essential element in ferritin to transport oxygen in tissue for host metabolism [51]. An excess of iron leads to heart and liver failures [52, 53] as well as causing ischemia stroke [54]. However, it is manganese that is of most concern because excess of Mn ions in low quantities (TC50 about 10-100 µM) can result in neurotoxicity linked to Parkinson's disease [51,55]. In addition, Mn with ion concentrations higher than 1 mM strongly decreases the proliferation and viability of MG63 osteoblasts as an increased amount of pro-inflammatory cytokine, interleukin 6 (IL-6), was found [56]. The recommended dietary allowance (RDA) of Mn is 2.3 mg/day for men and 1.8 mg/day

for women with the tolerable upper intake level (UL) of 11 mg/day; while the RDA for Fe is 16 mg/day for men and 12 mg/day for women with the UL of 45 mg/day [57].

Although several metal ions such as titanium, chromium, and cobalt from commercial total joint implants activate macrophages to release pro-inflammatory cytokines including interleukin-1β (IL-1β), IL-6, and tumor necrosis factor-α (TNF-α) [58] that induce differentiation of osteoclast lineages into mature osteoclasts to bone resorption [59], there is no study of whether Mn and Fe ions released from Fe-Mn alloys can result in gene expression of TNF-α, IL-1β, and IL-6, neither the cellular differentiation, proliferation, and molecular biological signaling affect the degradation parameters of temporary Fe-Mn implants have been studied. The biocompatibility of Fe-Mn alloys regarding alloy microstructures, numbers of metal particles/ions released as well as their effect on cellular behaviors in respect to degradation behaviors, need to be explored in the future.

1.6   Summary of Chapter 1

Development of bioresorbable metallic implants aims to provide temporary support and induce defected tissue regeneration where bone cells (osteoclasts and osteoblasts) repeat the processes of resorbing degraded alloy particles and secreting bone layers on the active interface, respectively. Due to their suitable microstructures, mechanical properties, and corrosion behavior characteristics, Fe-Mn alloys are considered as a new class of promising degradable metallic biomaterials for temporary orthopedic fixation devices. Despite the cellular metabolic activities of NIH3T3 and proliferation of MC3T3 that have been observed when cells were exposed to Fe-30Mn alloys, standardization and controllable porosity are required to optimize the degradation rate in this material system. Simultaneously, cell-based investigations of Fe-Mn alloys that focus on cellular gene expression and differentiation induced by metal degradation products, either ions or particles,

must be considered. Thus, designing transient orthopedic materials is an undertaking displaying a

high level of complexity of the investigations of the proposed material systems.

CHAPTER 2.   INVESTIGATION OF POROSITY ON MECHANICAL PROPERTIES, DEGRADATION AND *IN-VITRO* CYTOTOXICITY LIMIT OF FE30MN USING SPACE HOLDER TECHNIQUE

Experimental work and analysis were performed by Sabrina Huang. The writing was performed by Sabrina with the editing by Dr. Lia Stanciu. The work was submitted and published in Materials & Engineering C.

2.1   Background

Biodegradable, or bioresorbable, materials are temporary, nontoxic, and capable of being degraded and reabsorbed in human body within a designed period. Criteria for a successful transient implant include providing structural support, maintaining desired degradation and resorption rates as well as promoting appropriate interactions between cells, the extra-cellular matrix (ECM), and the implant itself. Other than mechanical properties, corrosion behavior, and biocompatibility of materials, the biological environment such as body temperature, level of pH, and local or systemic inclusions also affect the performance of materials after implantation. For orthopedic fixation implants such as bone pins, bone screws, and bone plates, etc., that require significant mechanical properties, metallic biomaterials are more suitable than polymers and ceramics owing to their strong structural support and high fatigue limit. Present biodegradable metals investigated are either iron-based or magnesium-based alloys because iron and magnesium already exist in minor quantities within the human body, which highlights them as highly biocompatible at low concentrations [60].

Pure iron is more attractive than magnesium in terms of its superior mechanical properties and stability when contacted with human plasma; magnesium corrodes and reacts with water rapidly,

creating undesirable hydrogen gas that prolongs tissue inflammation after implantation [61]. Iron also serves as a component of hemoglobin, a complex protein in erythrocytes, which plays a vital role in transporting oxygen from plasma to surrounding tissues [18]. Previous *in vivo* studies of stents composed of pure iron displayed no pronounced inflammation or significant toxicity at local or systematic tissues, making pure iron a feasible material for a degradable medical implant [14,15]. Nevertheless, reports showed that the *in vivo* degradation rates of pure iron were significantly slower than those expected *in vitro* due to complex surface phenomena [6,7]. Therefore, research on iron-based alloys concentrated on developing new methods to speed up their corrosion behaviors.

Studies focused on improving the overall degradation rate via alloying with other chemical elements such as manganese, palladium, carbon, phosphorus, and silicon, to create intermetallic phases, which can enhance galvanic corrosion while preserving mechanical properties compatible to host tissues [3,24,37,62–64]. Performing deformation on the alloys also increase their degradation rates. Li et. al. improved the degradation rates of Fe-20Mn alloy by introducing slip bandings using the accumulative cryo-rolling (ACR) at 77 K, followed by forming Fe_5C_2 phase along slip bandings in subsequently annealing [65]. Heiden et. al. found a 140% increase in degradation rate of Fe33Mn alloys when the alloy was subjected to large-strain machining (LSM) at a rake angle of $\alpha = 0°$ compared to the as cast alloy [66]. Another approach to increase degradation rate of Fe-based biomaterials is to create porosity that not only provides a large surface area, accelerating electrochemical reactions, but also allows the transport of body fluids, nutrients and waste, thus enhancing tissue regeneration [67]. Methods to fabricate porous Fe-based scaffolds include solid free-form fabrication processes such as inkjet 3D printing [33] and powder

metallurgy, such as space holder technique using ammonium bicarbonate as a porogen material [32]. Space-holders, or porogens, include materials like sodium chloride, ammonium bicarbonate, and carbamide, which have been successful for the production of porous metallic materials including stainless steel [68], titanium [69,70], magnesium-based alloy [71,72], and aluminum foams [73]. Vojtěch et. al. demonstrated porous iron scaffolds using ammonium bicarbonate (NH_4HCO_3) as a space-holder material, which exhibited mechanical properties comparable to natural bone and significantly higher than those of porous magnesium [74]. We aim to understand how inducing porosity in an on iron-based scaffold to increase degradation rate can affect the mechanical properties and cellular compatibility for potential use in orthopedic and cardiovascular applications.

In this study, we investigated the microstructure, degradation behaviors, metal toxicity, mechanical properties, and biocompatibility of the porous Fe-30Mn alloy using ammonium bicarbonate as a space-holder material where the porogen particle size was selected between 355 µm and 500 µm for the purpose of bone cell penetration and tissue ingrowth [75]. The composition of Fe-30Mn was selected because of its remarkable mechanical properties and biocompatibility. From the standpoint of mechanical properties, the austenite γ phase is prevalent in alloys having a Mn content above 27 wt.% [76] and the ductility of the alloy increases with increasing Mn content. Furthermore, when alloyed with more than 29 wt.% Mn, Fe-Mn alloys exhibit antiferromagnetic behavior [77]. This can be a great advantage for magnetic resonance imaging in clinical use. From the standpoint of biocompatibility, the murine fibroblast cells (NIH3T3) expressed the highest relative metabolic activity when they were exposed to Fe-30Mn powders at a concentration of 1 mg/ml [37]. Four experimental groups, Fe30Mn alloys containing 0 vol.%, 5 vol.%, 10 vol.%, and

60 vol.% of ammonium bicarbonate, were conducted in the present work. The experimental design of scaffold containing 60 vol.% ammonium bicarbonate was chosen as an extreme case for the purpose of showing that whether high levels of transition metal ions especially Mn^{2+}, would result in cytotoxic effects even if an extremely large porosity would show a high corrosion rate. The tissue culture polystyrene (TCPS) was the reference in the study of indirect and direct cytotoxicity tests. Furthermore, the relationship between alloy corrosion behaviors and metallic ion-released concentrations was evaluated over a period of 30 days.

2.2   Material and Methods

2.2.1   Sample Fabrication

Figure 2.1 showed the process flow chart for the sample fabrication. A mixture of iron (IRON325, Chemical Store, New Jersey) and manganese powders (MN-101, Atlantic Equipment Engineers, New Jersey) in a weight ratio of 7:3 was mixed with designed volume percentage of NH_4HCO_3 (Sigma-Aldrich, Missouri), that is, a. Fe-30Mn with -no pores, b. Fe-30Mn with -5 vol.% NH_4HCO_3, c. Fe-30Mn with -10 vol.% NH_4HCO_3, and d. Fe-30Mn with -60 vol.% NH_4HCO_3, in a high speed mixer (FlackTek, South Carolina) where ethanol with 10 wt.% of the total mixture was added for lubrication. Ammonium bicarbonate was sieved to -35+45 mesh (355-500µm) before mixing. The mixture was spun at 800 rpm for 15 mins and cold pressed at 600 MPa using a hydraulic press (Carver, New Jersey) to obtain cylindrical-shaped compacts with an average size of 12.7 mm in diameter and 25 mm in length for compression testing and disc-shaped compacts with a green body diameter of 12.7 mm and thickness of 1.3 mm for rest of the tests. The green compacts were loaded in a muffle furnace (Lindberg, Wisconsin), heat treated at 120 °C for 2 hours to decompose the ammonium bicarbonate in the compacts, subsequently heat treated at 1200 °C for 3 hours, and finally cooled to the room temperature. All samples were sintered with a heating rate of 10 °C/min under argon atmosphere. The sintered samples were mechanically ground with silicon carbide papers in a grit size of 2000 and stored in a desiccator for further examinations.
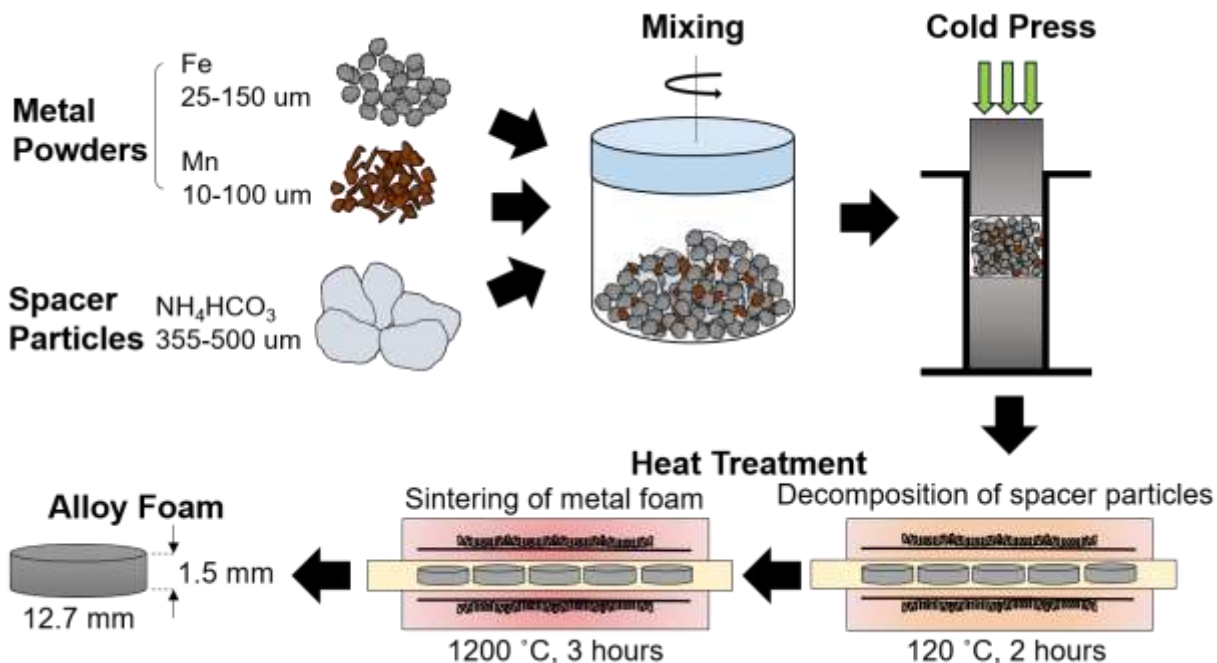
Figure 2.1 Schematic illustration of the sample fabrication using the space holder technique

2.2.2   Material Characterization

Surface microstructures and alloy compositions of the sintered samples were examined using an optical microscope and a scanning electron microscope (SEM; FEI Philips XL-40) coupled with energy dispersive x-ray spectroscopy (EDS). Densities and open porosity of the samples were obtained through the Archimedes' principle followed by ASTM standard B962-17 and Hrubovčáková, et. al. [78,79]. Phase crystalline structures of the bulk samples were determined using an X-ray diffractometer (XRD; Bruker D8 Focus) with a monochromatic Cu-K$_\alpha$ source, operating at 40 kV, 40 mA with a scanning rate of 5°/min.

2.2.3 Compression Test

Standard compression test of the non-porous and porous Fe-30Mn alloys (n = 3) were performed according to ASTM standard E9-09. Cylindrical sintered specimens with an average size of 12.5 mm in diameter and 25 mm in length were loaded on an electromechanical compression machine (MTS Insight 100) and compressed by a loading cell (100 kN MTS, Minnesota) with a compressive speed of 0.25 mm/min. The test came to a halt as the loaded sample broke or when the loaded force reached to 100 kN, thereafter the compressive stress, strain, and elastic modulus of the specimens were recorded.

2.2.4 Potentiodynamic Polarization Testing

Reproducible corrosion potentials and corrosion current densities of the polished non-porous and porous disk-shaped samples (n = 4) were measured followed by ASTM standard E59-97. A cell culture medium, alpha minimum essential medium eagle modification (α-MEM; Sigma-Aldrich, Missouri), was chosen as the electrolyte for both potentiodynamic polarization and immersion tests because of its replicable standardized preparation [80] and consistency to compare results in *in-vitro* cytotoxicity tests. Every sample was mounted with thermoplastic acrylic resins so that only one side of the sample area was exposed to the electrolyte at 37 ± 1 °C. All mounted samples were cleansed with ethanol prior to the electrochemical polarization test, of which the experimental setup consists a saturated calomel electrode (SCE) as the reference electrode, a platinum wire as the counter electrode, and the sample as the working electrode. A small potential scan, which represented the potential between the sample and the reference electrode, was applied to the sample, sweeping linearly from -0.15 V to +0.15 V at a rate of 0.1667 mV/s. Meanwhile, the resulted current at the sample was recorded using EC-Lab v-10.19 BioLogic Science Instruments software.

The corrosion potential and corrosion current density of each sample were determined on the obtained Tafel plot. Consequently, the corrosion rate (CR_P) was obtained in millimeter per year (mmpy) using the following equation:

$$Corrosion\ rate\ (mmpy)\ = 3.27 \times 10^{-3}\ \frac{i_{corr} \times EW}{\rho}\ --- Eq.\,2.1$$

, where EW is equivalent weight of the specimen in g, i_{corr} is corrosion current density in $\mu A/cm^2$, and ρ is density of the specimen in g/cm^3.

The average surface area containing porosity of each group was calculated using ImageJ [81] with adjusted binary threshold. The surface area (SA) of each sample was calculated in the following equation:

$$SA\ (mm^2)\ = \frac{1}{2}\pi d^2\ + \pi dt +\ \pi Ip\ --- Eq.\,2.2$$

, where d is diameter of the specimen in mm, t is thickness of the specimen in mm, I is average pore depth in mm, and p is sum of pore feret diameter in mm.

2.2.5   Static Immersion Test

Porous and non-porous Fe30Mn specimens (n = 3) were submerged into the α-MEM solution and incubated at 37°C for 1 day, 7 days, 15 days, and 30 days, and were removed at each checked point. The ion concentrations of the sample extract were examined in ppb using an inductively coupled plasma mass spectrometer (ICP-MS; Perkin Elmer Elan DRC II) by diluting the sample extract 100-fold with DI water containing 0.5% nitric acid. Average Mn ion release rates in mg/day from each sample group was calculated assuming 3L of plasma from a 70kg young adult man. Samples were rinsed with PBS followed by ethanol and the surface corrosion products were examined under an optical microscope and SEM. Afterwards, corrosion products were

mechanically and chemically cleaned according to the ASTM standard G1-03. The corrosion rate

of each sample was measured according to the ASTM standard G31-12a in the following equation:

$$Corrosion\ rate\ (mmpy)\ = \frac{K \times W}{A \times T \times D} --- Eq.\ 2.3$$

, where K is a constant 8.76×10^4, T is time of exposure in hours, A is area in cm^2, W is mass loss

in g, and D is density of the specimen in g/cm^3.

2.2.6   Indirect Cytotoxicity Test

The indirect cytotoxic effect of porous (5-vol.%, 10-vol.%, and 60-vol.% NH_4HCO_3) and non-

porous Fe30Mn specimens (n = 3) was examined according to the ISO 10993-5 protocol.

Degradable samples were immersed in a cell culture media, α-MEM supplemented with 10% fetal

bovine serum, 5% Penicillin Streptomycin, and 0.5% Fungizone, and placed inside an incubator

mimicking the physiological environment (pH = 7, 5% CO_2, $37.5 \pm 0.5°C$) for 24 hours.

Consequently, the test sample extract was collected, diluted into 75%, 50% and 25% of its original

concentration, and stored in the incubator under the same physiological environment as mentioned

above. Mouse bone marrow stromal cells (BMSC; ATCC, D1 ORL UVA) were cultured in a 96-

well plate with a density of 10^4 cells / 100 µl of cell culture media; after 1 day of culturing, the

culture media was replaced with the 4 concentrations of test sample extract. The BMSC treated

with test sample extracts were incubated for another 24 hours and their viability were examined

by conducting an MTS assay (Promega, CellTiter 96 AQueous One Solution Cell Proliferation

Assay). According to the manufacturer's protocol, the absorbance reading of formazan product

reduced   from   a   tetrazolium   compound   [3-(4,5-dimethylthiazol-2-yl)-5-(3-

carboxymethoxyphenyl)-2-(4-sulfophenyl)-2H-tetrazolium, inner salt; MTS] was measured using

a VersamaxTM absorbance microplate reader (Molecular Devices). Quantity of the formazan

product is proportional to the cell number on absorbance at 490nm. Cellular viability of each group is normalized to that of the reference TCPS.

2.2.7   Direct In-Vitro Cytotoxicity Test

The direct cytotoxic effect of porous (5-vol.%, 10-vol.%, and 60-vol.% NH_4HCO_3) and non-porous Fe30Mn specimens (n = 3) was examined via seeding BMSC directly on samples in a density of $10,000/cm^2$ under the same physiological environment. After 1 and 7 days of incubation, cellular viability of each group was observed by labelling cellular membrane with 10 µM fluorescent marker CellTracker Green CMFDA Dye (Life Technologies, Grand Island, NY) and 0.1 ug/ml Hoechst Fluorescent Stain (ThermoFisher Scientific, Waltham, MA). After 30 minutes, samples were rinsed with PBS three times to wash the excessive dye. Since Fe ions released from the samples interfered strongly with the absorbance reading of the MTS assay, only cellular morphology was examined in the direct in-vitro cytotoxicity test.

2.2.8   Statistical Analysis

A minimum of three replicates of the sample group (n = 3) were conducted for every experiment except the potentiodynamic polarization test (n = 4). Quantitative data from each test were collected and evaluated through the analysis of variance (ANOVA) in Microsoft Excel. A threshold of p = 0.05 was set to determine statistical significance.

2.3   Results and Discussion

2.3.1   Microstructures

Figure 2.2 shows the morphology of Fe-30Mn mixed with 0-vol%, 5-vol.%, 10-vol.% and 60-vol.% ammonium bicarbonate and their corresponding SEM images at higher magnifications. Polygonal pores, created from the decomposition of ammonium bicarbonate during sintering, revealed similar

microstructures among all porous groups, in which micro-voids formed within the scaffold cell walls along grain boundaries. Micro-voids formation along the grain boundaries during the final stage of sintering is a well-known phenomenon [82] and these voids significantly enlarge the scaffold surface areas to expose the scaffold to the fluid penetration, consequently increasing the corrosion rate. Also, pores are distributed homogeneously so that replicable scaffold mechanical properties can be obtained.

The density of each group measured from Archimedes' principle is shown in Table 2.1. As we expected, the density of Fe-30Mn alloy decreases as the volume fraction of ammonium bicarbonate increases; an average density of 6.6 g/cm^3 was obtained for the non-porogen group whereas the average density of 5.2 g/cm^3 was obtained for the 60-vol.% porogen group. This is because the density of ammonium bicarbonate is lower than that of Fe and Mn powders, as a result, the density of the green compact decreased with increasing volume fraction of ammonium bicarbonate after powder mixing, compaction, and sintering. Similar results of increasing space holder volume fraction decreases the scaffold density, or increases total porosity, were found in several studies [32,69,83].
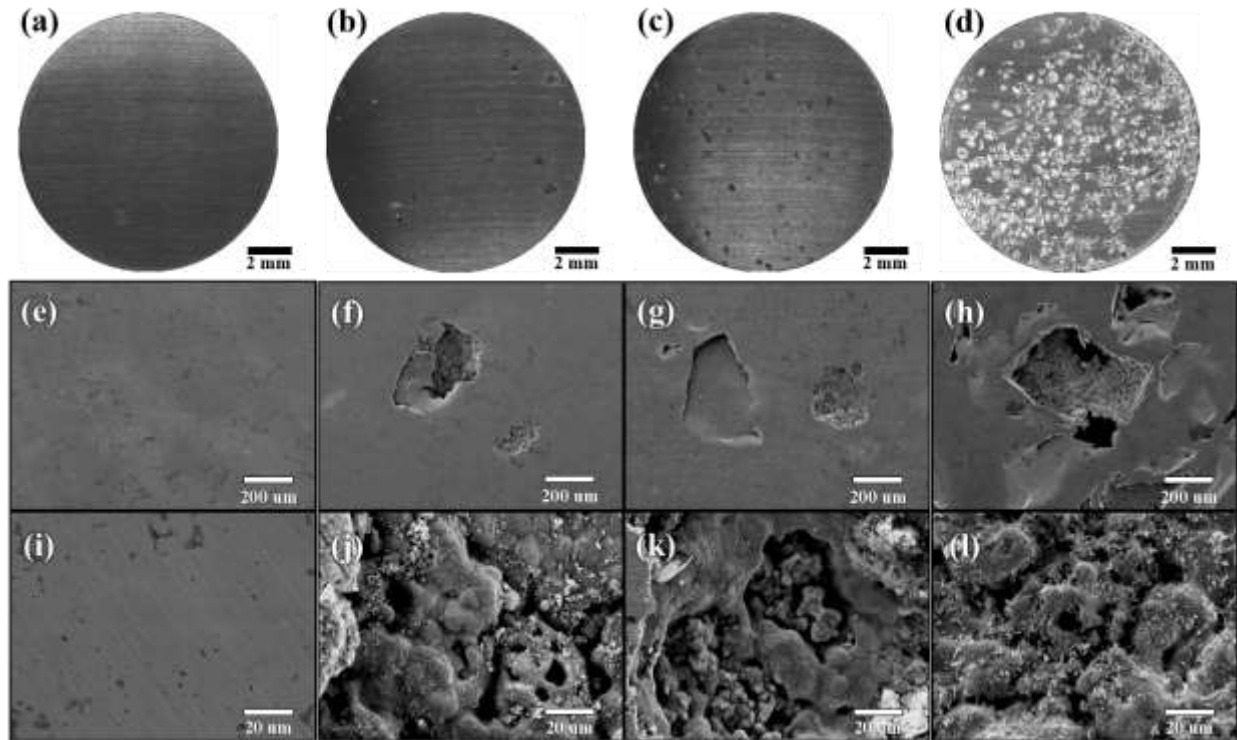
Figure 2.2 Optical and SEM images of sintered Fe30Mn alloys with no pore (a, e, i), 5-vol% pore (b, f, j), 10-vol% pore (c, g, k), and 60-vol% pore (d, h, l) under different magnifications

In Figure 2.2 (f-h), cracks propagated along the pore edge, which phenomenon was caused by the fracture of ammonium bicarbonate during the compaction process. Laptev et. al. reported that fracture of ammonium bicarbonate was observed when subjected to a compaction pressure of 350MPa in preparing porous titanium scaffolds [84]. Deformation of ammonium bicarbonate leads to anisotropic properties of scaffolds [85] and trapped space holder residues [86], leading the sintered scaffolds more vulnerable to impurities. This explains the observation of needle-like impurities of C and O on the surface in the samples mixed with 5-vol.%, 10-vol.% and 60-vol.% ammonium bicarbonate in Figure 2.2 (j-l). The contamination can be limited through better mixing and vacuum sintering. However, the high compaction pressure we used in this study is to increase the strength of the scaffold and to reduce the shrinkage after sintering. Further optimization of the

compaction pressure that would prevent ammonium bicarbonate distortion while maintaining scaffold strength and limited shrinkage is necessary.

Table 2.1 Porosity and mechanical properties of Fe-30Mn

Group	Density (g/cm^3)	Total Porosity (%)	Open Porosity (%)	Compressive Elastic Modulus (GPa)	Ultimate Compressive Strength (MPa)	Ultimate Compressive Strain (%)
0% Pore	6.6 ± .1	14.4 ± 1	5.7 ± 1	3.50 ± .3	702 ± 36	54.0 ± 1
5% Pore	6.5 ± .1	15.8 ± 2	9.1 ± 1	4.01 ± .1	741 ± 5	52.8 ± 2
10% Pore	6.4 ± .1	17.0 ± 2	8.8 ± 2	3.73 ± .2	737 ± 19*	52.9 ± 3
60% Pore	5.2 ± .3	32.5 ± 3	13.0 ± 2	1.42 ± .5	381 ± 138	55.8 ± 8

* Test was stopped because the applied load was close to the machine limit

The porosity is not necessarily homogenous or interconnected by using this processing method, which is not ideal for tissue engineering applications. However, fracture fixation devices such as bone pins or screws are usually made of stainless steel and are not porous. Sometimes, porosity or roughness at the surface is just induced by coating implants with hydroxyapatite. Inducing any kind of porosity into the Fe-Mn scaffold is expected to have an effect on surface roughness, transition metal leaching rates, as well as on the mechanical properties, thus giving valuable information regarding whether or not including porosity is a valid avenue for increasing degradation rate of Fe-Mn alloys, while still rendering the material usable for implantation.

2.3.2   Phase Constituents, Elastic Modulus, and Compressive Strengths

Figure 2.3 shows the x-ray diffraction patterns and compressive stress-strain curves of Fe-30Mn with different volume fractions of ammonium bicarbonate. All studied materials consisted of a duplex structure of austenite (γ) and martensite (ε) phases resulting from the sample martensitic

transformation ($\gamma \rightarrow \varepsilon$) upon cooling [87,88]. This indicates neither additional chemical reactions occurred in sintering nor NH4HCO3 had an impact on the phase transformation of the alloy. With increasing porosity, lower and broader peaks were observed due to lesser degree of crystallinity.
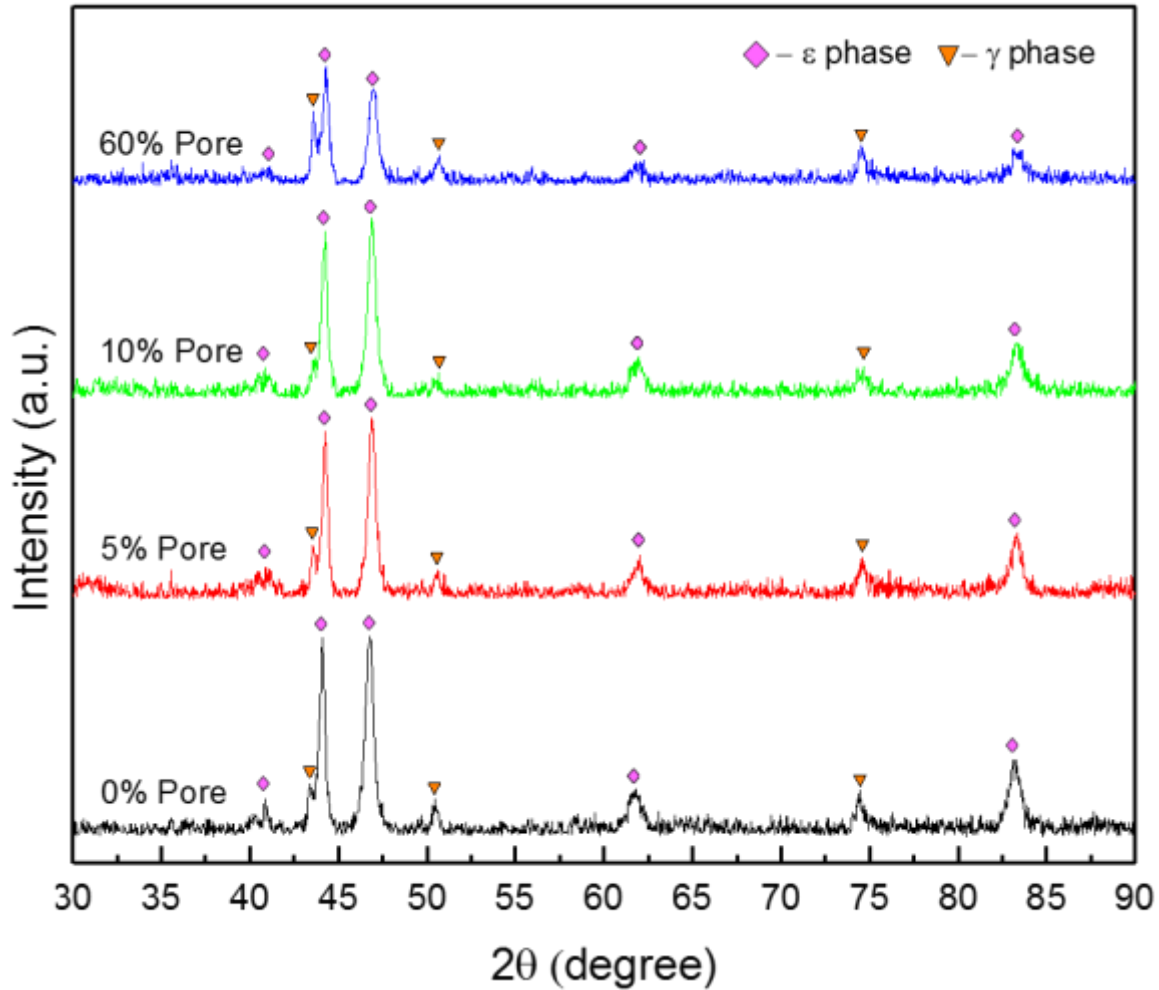
Figure 2.3 XRD diffraction pattern of Fe-30Mn with 0-, 5-, 10- and 60-vol.% pore

Diffraction peaks of studied scaffolds slightly shifted toward higher 2θ angles as the volume fraction of ammonium bicarbonate increased. Specifically, the epsilon ε peak at 44.08° in the no space holder sample shifted to 44.30° in the sample mixed with 60-vol.% ammonium bicarbonate. Similarly, the gamma γ peak at 50.45° in the no porogen sample shifted to 50.71° in the sample

mixed with 60-vol% ammonium bicarbonate. The peak shifting phenomenon is considered to be a result of the increase of the internal stress in the matrix cell wall due to the formation of macro pores. With a larger amount of space holder content, the lattice distortion and plastic deformation between matrix powders increased as the mixed powders were subjected to high-pressure compaction. These stacking and twin faults in the γ matrix acted as ε phase nucleation sites [89] as the scaffold underwent martensitic transformation in the sintering process. Consequently, the increasing number of ε phase reduced the lattice parameters of ε phase in the scaffold [90], which corresponded to the ε phase peak shifting toward higher 2θ angles. In addition, the austenite γ phase adjacent to the ε phase suffered higher tensile stress as the amount of ε phase increased, leading to γ phase peak shifting toward higher 2θ angles as well [90].

Compressive stress-strain curves of the studied scaffolds are shown in Figure 2.4. A replicate of three samples in each studied group was tested and their average values of compressive elastic modulus, ultimate compressive strength as well as compressive strain corresponding to the ultimate compressive strength were presented in Table 2.1. Among the studied materials, scaffolds mixed with 60-vol.% ammonium bicarbonate exhibited the lowest average value of compressive elastic modulus and ultimate compressive strength at 1.29 GPa and 381 MPa, respectively. However, its low ultimate compressive strength, comparing to the other tested groups, is still higher than a typical human wet compact bone [91]. Increased porogen contents resulted in increased porosity of sintered scaffolds. As indicated in Table 2.1, the highest average value of overall porosity among the tested scaffolds was observed in scaffolds mixed with 60-vol.% ammonium bicarbonate. These macro-pores in the matrix were the source of stress concentration during deformation [92,93], leading micro-cracks formation and propagation fracture failure under

low compressive strength. Furthermore, a 116% increase in pore size from scaffolds mixed with 5-vol.% porogen to scaffolds mixed with 60-vol.% porogen was observed, as shown in Figure 2.2 (h), demonstrating the formation of interconnected pores developed in scaffolds mixed with high porogen content [92,94]. These irregular polygonal interconnected pores deviated scaffold compressive stress-strain behavior significantly, as shown in Figure 2.4 (d). This is due to non-uniform scaffold relative density [95] and micro-pore formation along grain boundaries in the macro-pore cell walls.

Notice in Table 2.1, compared to non-porous scaffolds, scaffolds mixed with 5-vol.% and 10-vol.% ammonium bicarbonate showed greater average values of compressive elastic modulus and ultimate compressive strength. This can be attributed to the degree of packing efficiency of the matrix powders and space holder during compaction. Fine matrix powders tend to agglomerate, resulting in poor flowability and low packing density, consequently leaving micro-voids within matrix cell walls after sintering, as shown in Figure 2.2 (i). A mixture mixed with both large and small particles presented a higher packing density, flowability and sintered density than the mixture mixed with mono-sized fine particles [96]. Since ammonium bicarbonate particulates were one order of magnitude larger than the matrix powders, an addition of ammonium bicarbonate increased the number of inter-particle contacts and enhanced necking growth [97] during sintering, which greatly improved the compressive elastic modulus and ultimate compressive strength. As a result, scaffolds mixed with 5-vol.% and 10-vol.% ammonium bicarbonate presented stronger mechanical properties than those without ammonium bicarbonate.
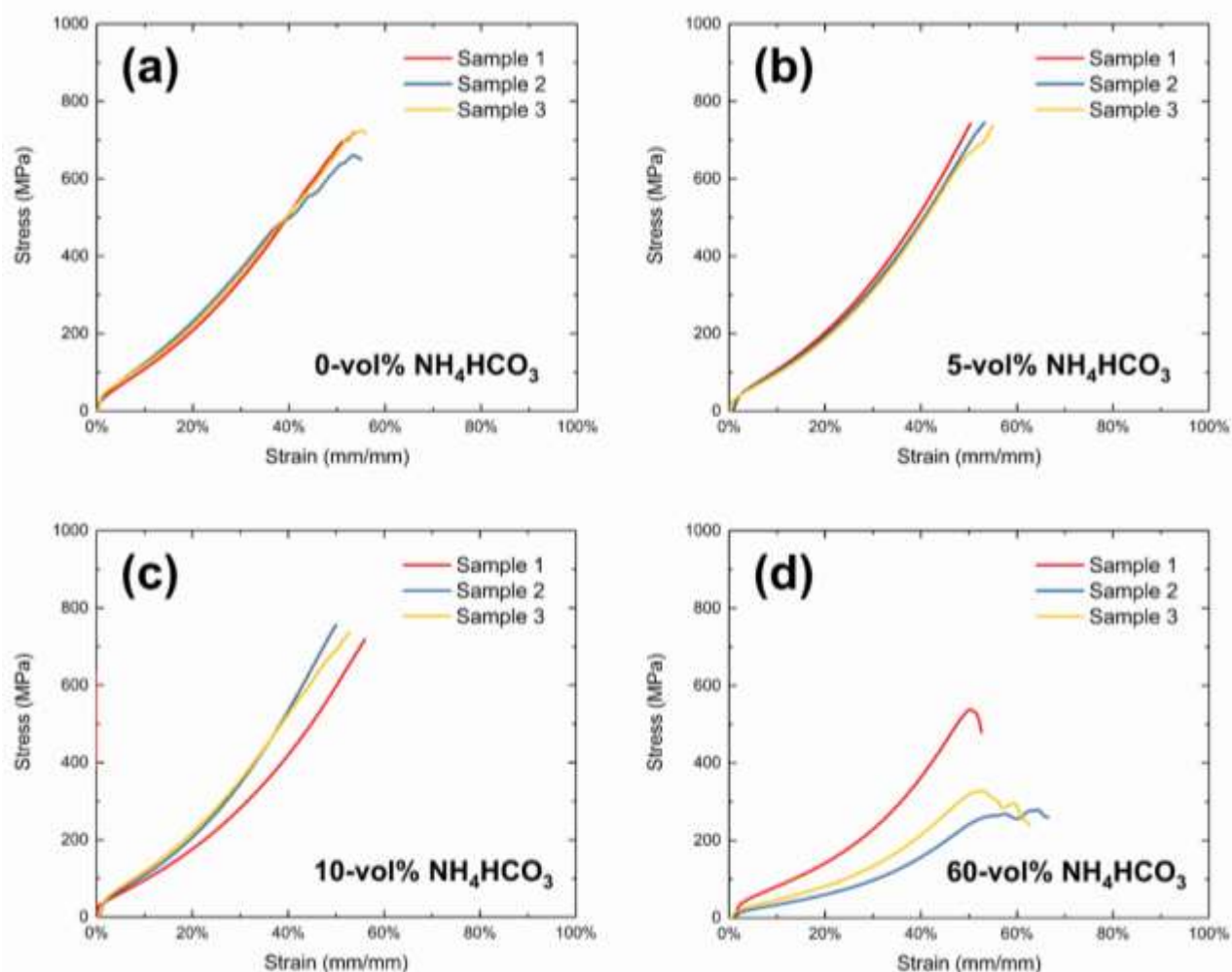
Figure 2.4 Compressive stress-strain curves of the corresponding studied samples

2.3.3   Potentiodynamic Test

Potentiodynamic polarization curves of the studied materials were shown in Figure 2.5; their corresponded average values of corrosion potentials (E_{corr}), corrosion current densities (i_{corr}), and corrosion rates (CR_P) obtained from Tafel extrapolation were indicated in Table 2.2.
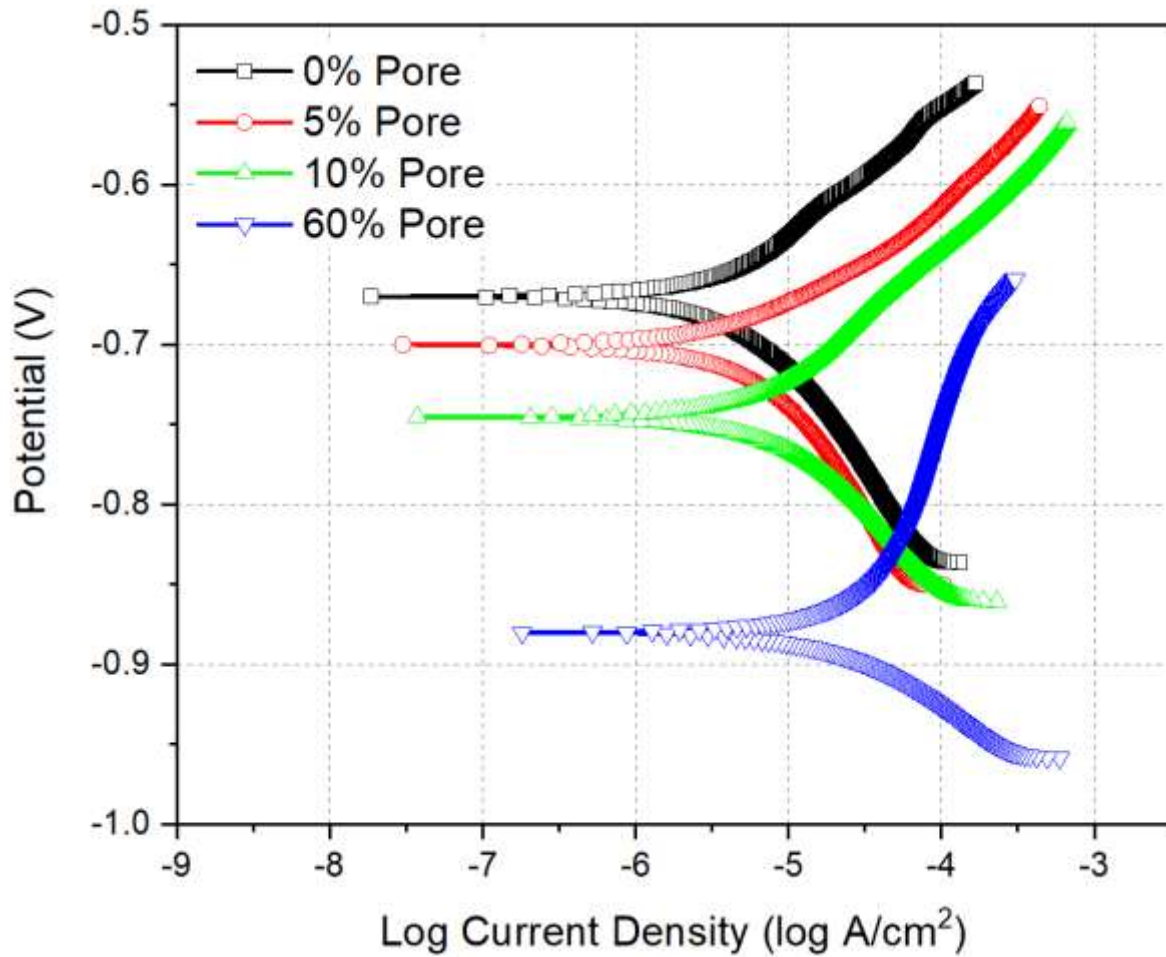
Figure 2.5 Potentiodynamic polarization curves of the sintered Fe30Mn samples in α-MEM solution (pH 7.4) at 37 ± 1 °C

Table 2.2 Average sample corrosion potentials (E_{corr}), corrosion current densities (I_{corr}), corrosion rates (CR_p) obtained from the potentiodynamic polarization curves and corrosion rates obtained from the static immersion test (CR_{i30}) after 30 days of incubation in α-MEM solution (pH 7.4) at 37 ± 1 °C with 5% CO_2

Group	E_{corr} (mV)	I_{corr} ($\mu A/cm^2$)	CR_p (mmpy)	CR_{i30} (mmpy)
0% Pore	-663 ± 22	10 ± 5	$0.134 \pm .07$	$0.074 \pm .03$
5% Pore	-720 ± 59	11 ± 5	$0.144 \pm .07$	$0.135 \pm .03$
10% Pore	-730 ± 34	20 ± 7	$0.260 \pm .09$	$0.147 \pm .05$
60% Pore	-869 ± 16	58 ± 12	$0.980 \pm .20$	$0.389 \pm .05$

There was a decrease of 206 mV in potential and an increase of 48 $\mu A/cm^2$ in current density from non-porogen scaffolds to scaffolds mixed with 60-vol.% ammonium bicarbonate, indicating scaffold corrosion rates increased with increasing amount of ammonium bicarbonate. The increased amount of ammonium bicarbonate not only provided large surface areas for electrochemical reactions to occur in the presence of electrolyte but also increased the amount of martensite phases, as mentioned in section 2.3.2. These martensite phases, along with adjacent austenite phases, became micro-galvanic corrosion couples [24,98,99], further facilitating the corrosion reaction in the matrix. Notice that the average corrosion rate of non-porous scaffolds ~ 0.13 mm/year was calculated from Eq. 2.1, and was lower than the majority of literature data, ~ 0.29-0.7 mm/year [24,99], due to the differences in selected electrolytes. The conventional α-MEM consists of lower chloride (Cl^-) and higher carbonate (CO_3^{2-}) ion concentrations than the Kokubo's simulated body fluid and Hank's balanced salt solutions [80,100], which significantly abated surface dissolution caused by Cl^- ions attack and expedited the formation of metal carbonates, respectively. As a result, a lower average corrosion rate of non-porous scaffolds was obtained.

2.3.4   Immersion Mass Loss Test

Average corrosion rates of the studied materials are depicted as a function of incubation time in Figure 2.6 and their numerical values after 30 days of incubation (CR_{i30}) are listed in Table 2.2.
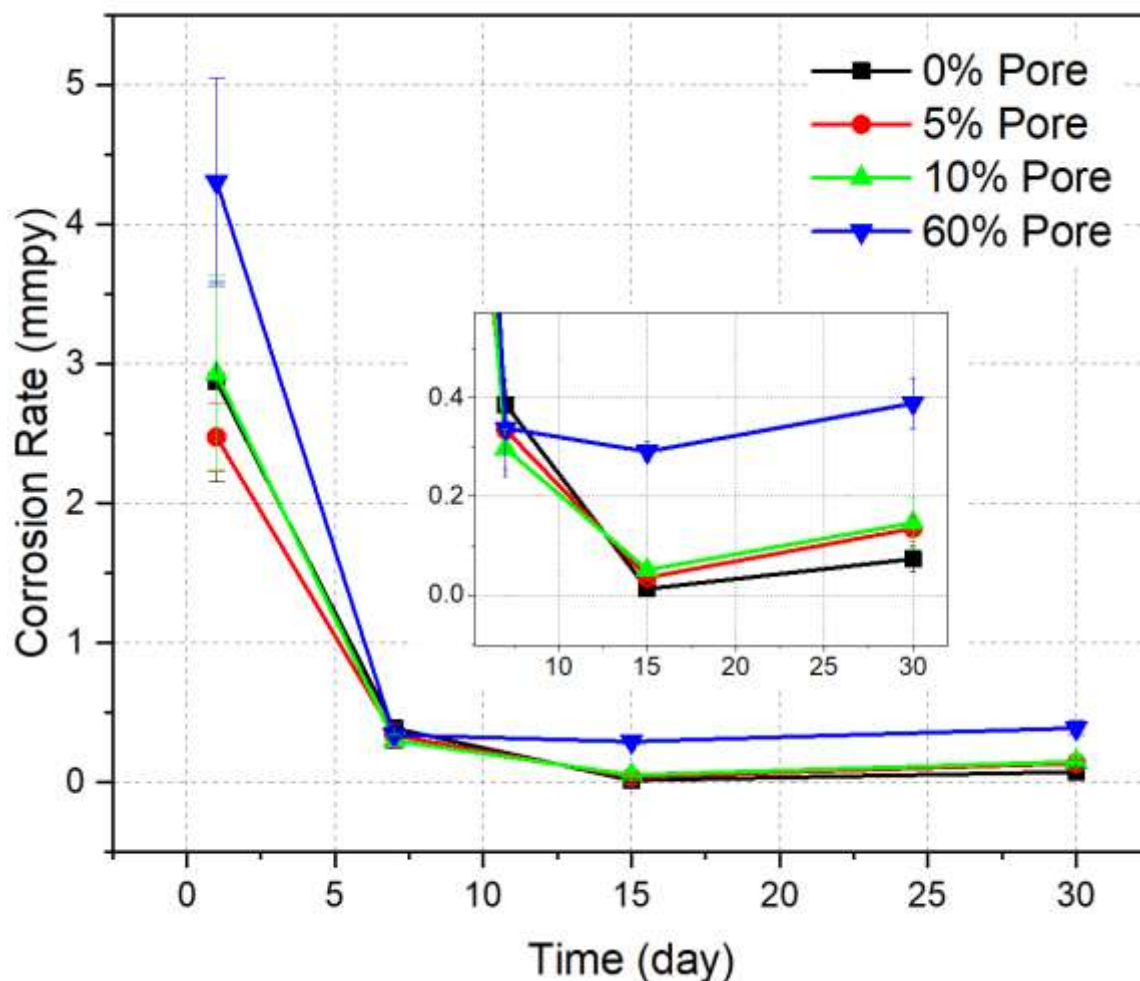
Figure 2.6 The average sample corrosion rates over a period of 1 day, 7 days, 15 days, and 30 days of incubation through the immersion static test

The highest average value of CR_{i30} was observed in scaffolds mixed with 60-vol.% ammonium bicarbonate, which is consistent with the trend that high porosity enhances the corrosion rate, similar to the results observed in the potentiodynamic polarization test. However, comparing both results obtained from potentiodynamic polarization and immersion mass loss tests, much lower corrosion rates were observed in the mass loss test because extended exposure time allowed scaffolds to interact with the medium, which greatly affected local pH and chemical composition at the scaffold-medium interface, leading to both pitting and formation of oxide layers. Also, with

the increasing incubation time, the corrosion rates of all studied materials decreased due to the formation of corrosion products on scaffold surfaces, as shown in Figure 2.7, preventing bulk metal from being exposed to the fluid.

The mass loss corrosion test is more desirable than the potentiodynamic polarization test because the mass loss test mimics the physiologic environment due to real-time pitting formation in addition to the galvanic corrosion. Furthermore, the electrochemical reaction of Fe involves at least 3 steps which may interfere the result of the Tafel curve. However, for the purpose of the present study, which is to just compare the effect of porosity on properties, the electrochemical test is a time-efficient method to test corrosion rates within the groups (i.e. testing the trend of porosity effect on corrosion rates) for the purpose of comparison.
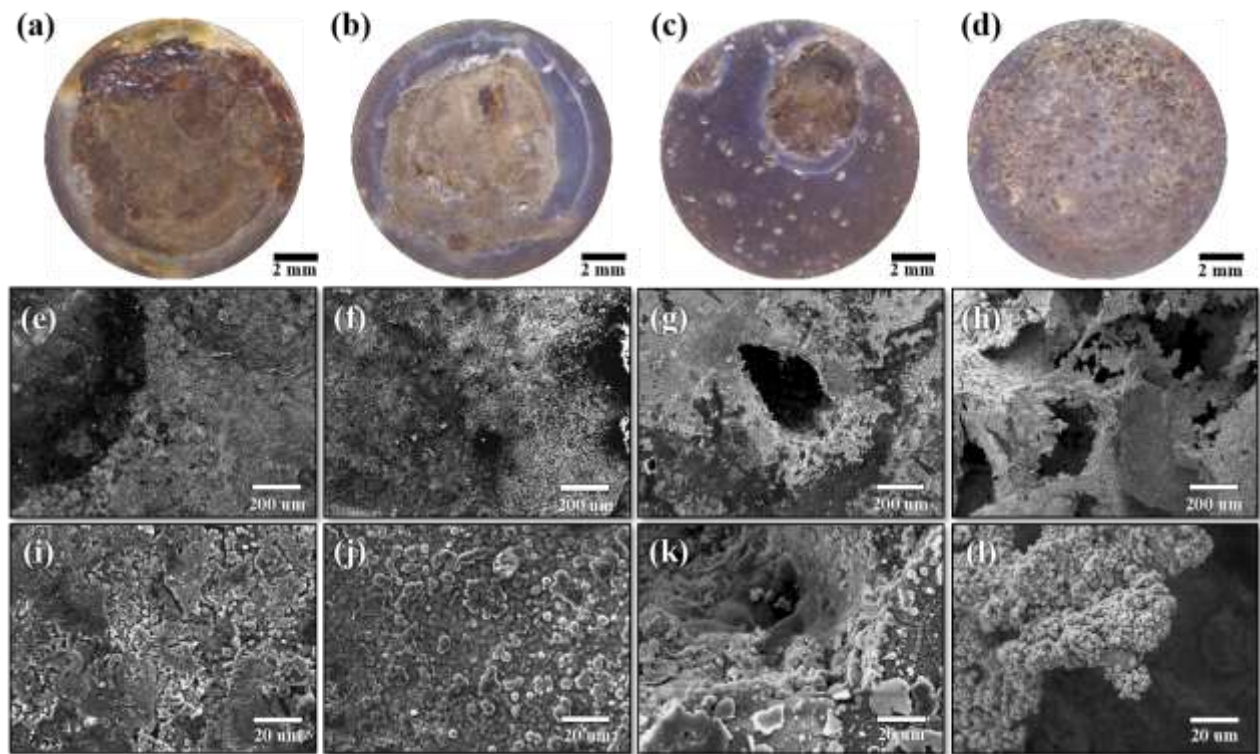
Figure 2.7 Optical and SEM images of corroded sintered Fe-30Mn alloys with no pore (a, e, i), 5-vol.% pore (b, f, j), 10-vol.% pore (c, g, k), and 60-vol.% pore (d, h, l) after 30 days of immersion in α-MEM solution (pH 7.4) at 37°C with 5% CO_2

After 30 days of incubation, flake-like oxide layers were observed in non-porous scaffolds and scaffolds mixed with 5-vol.% ammonium bicarbonate whereas localized pitting and crevice corrosion was detected in scaffolds containing higher porosity. These corrosion products were composed of metal hydroxides, metal carbonates, and calcium-phosphorus clusters analyzed quantitatively from the EDX in Figure 2.8 and Figure 2.9, which were similar to the results found in literature [37,101]. Notice that higher oxygen and calcium concentrations were observed in the non-porous group (Figure 2.8) compared to the scaffolds mixed with 10-vol.% ammonium bicarbonate (Figure 2.9), indicating that the passivating flake-like oxide layers inhibited oxygen transport to the scaffold surface, yet broke down with reducing corrosion potential values and increasing corrosion densities as a result of increasing amounts of interconnected macro-pores and mico-pores within cell wall. Furthermore, preferential release of manganese into the medium was observed in Figure 2.9, which corresponded to the review that manganese is more thermodynamically favorable in aqueous state than iron within pH range of 6-10 [102]. The toxicity effect of manganese ions within the solution was therefore the interest in this study.

Element	Wt%	At%
CK	6.23	15.91
OK	17.87	34.26
PK	3.14	3.11
CaK	30.43	23.30
MnK	17.09	9.54
FeK	25.24	13.87

Element	Wt%	At%
CK	5.31	14.80
OK	14.06	29.42
PK	1.41	1.52
CaK	27.73	23.16
MnK	22.43	13.67
FeK	29.07	17.43
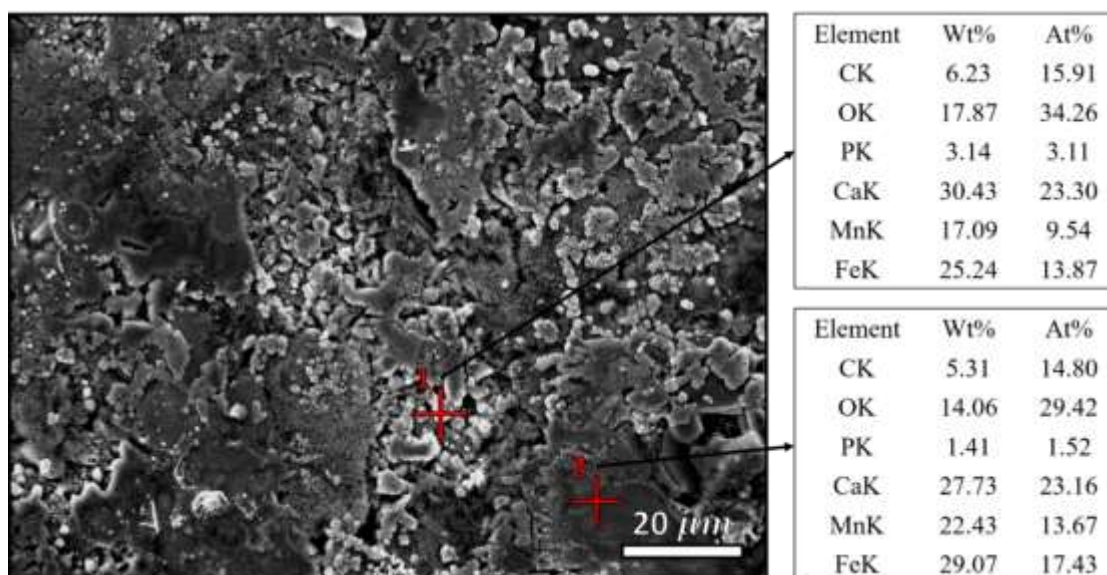
Figure 2.8 Concentrations of the oxidized surface layer on non-porous scaffolds after 30 days of incubation. Data retrieved from Figure 2.6 (i) using the EDS

Element	Wt%	At%
CK	4.54	15.07
OK	5.80	14.45
PK	6.87	8.84
CaK	8.94	8.89
MnK	6.00	4.35
FeK	67.84	48.39

Element	Wt%	At%
CK	3.40	11.69
OK	5.50	14.21
PK	7.10	9.46
CaK	8.31	8.56
MnK	6.93	5.21
FeK	68.76	50.85

Element	Wt%	At%
CK	4.45	15.10
OK	5.33	13.59
PK	6.40	8.42
CaK	5.80	5.89
MnK	6.22	4.61
FeK	71.79	52.38

Element	Wt%	At%
CK	5.93	12.10
OK	25.36	38.86
MgK	19.93	20.10
CaK	43.51	26.62
MnK	1.44	0.64
FeK	3.83	1.68
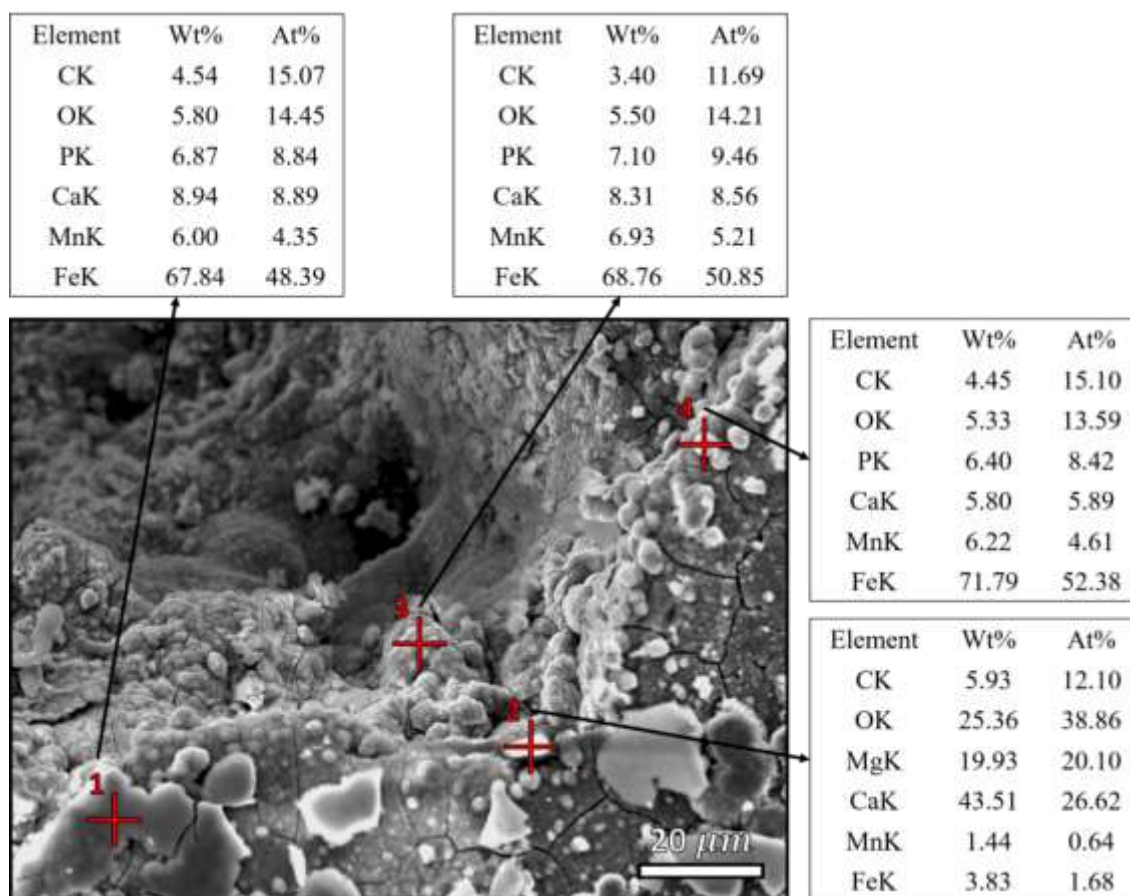
Figure 2.9 Concentrations of the oxidized surface layer on scaffolds mixed with 10-vol.% NH_4HCO_3 after 30 days of incubation. Data retrieved from Figure 2.7 (k) using the EDS

2.3.5   Ion Release Study & Indirect Cytotoxicity Test

Since Mn has a lower standard reduction potential than Fe, Mn^{2+} ions release preferentially than Fe^{2+}/Fe^{3+} ions into the cell culture media. The EDS result in the scaffold mixed with 10-vol.% ammonium bicarbonate after 30 days of incubation (Figure 2.9) shows a significant reduced amount of Mn (~70% reduction from its original 30-wt.%). The amount of Fe after 30 days of incubation remained almost the same as that prior to the incubation, which also confirms the preferential release of Mn from the sample to the electrolyte (i.e. α-MEM). Therefore, only the Mn^{2+} release concentration was taken into account for the ion release study.

Rates of Mn^{2+} ions leached out from the studied groups into α-MEM over 30 days were plotted in Figure 2.10. With increasing incubation time, the ion-released rates decreased daily due to the increasing corrosion products forming on top of the samples; as a result, lower corrosion rates of the studied groups were observed, as shown in Figure 2.6. This demonstrates the consistency and accountability of both immersion mass loss and ion release tests. Notice that on the incubation of Day 30, Mn ions released from the non-porous group was close to that from the 60-vol.% pore group. One possible answer is that the oxide layer on non-porous sample became too thick and layers of oxide flaked off from the sample (flake-like structure is observed in Figure 2.7), resulting in the fresh surface exposed to the media directly and consequently evokes further corrosion. This also tells why large deviations of Mn releasing is observed from the non-porous samples.
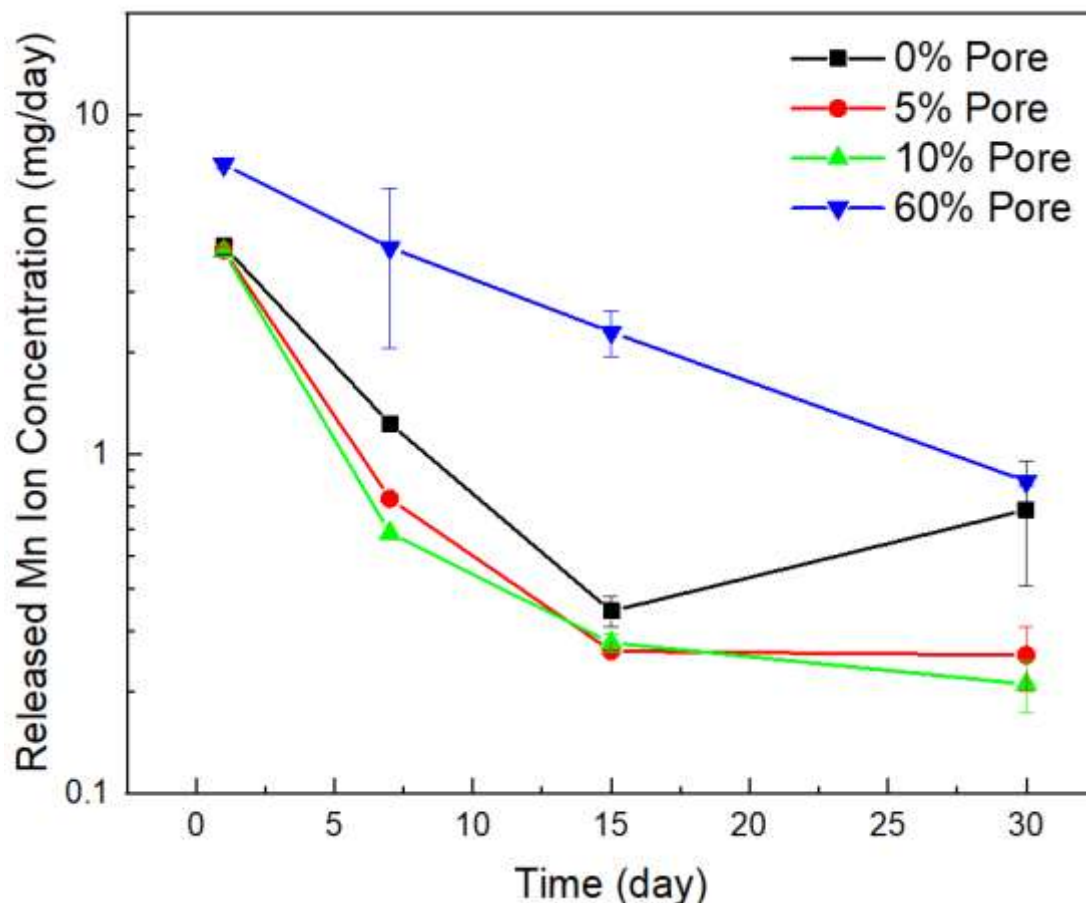
Figure 2.10 Mn ion release of the studied groups over a period of 30 days

Since Mn ions dispersed significantly on the first day of incubation, cell viability resulted from acute exposure of the studied groups in 100% extract was also examined, as depicted in Figure 2.11. According to the standard ISO10993-5 [103], a reduction of cellular viability by more than 30% of the negative control group is considered a cytotoxic effect. Extract from scaffolds contained 0%, 5% and 10% ammonium bicarbonate were not toxic to the cells, while the extract from the 60% pore group has a cytotoxicity effect. This cytotoxic effect corresponds to the highest Mn released rate observed in scaffolds containing 60-vol.% ammonium bicarbonate at a value of 7.14 mg/day while the other sample groups presented similar Mn released rates with the values around 4 mg/day after 1 day of incubation, as shown in Table 2.3.
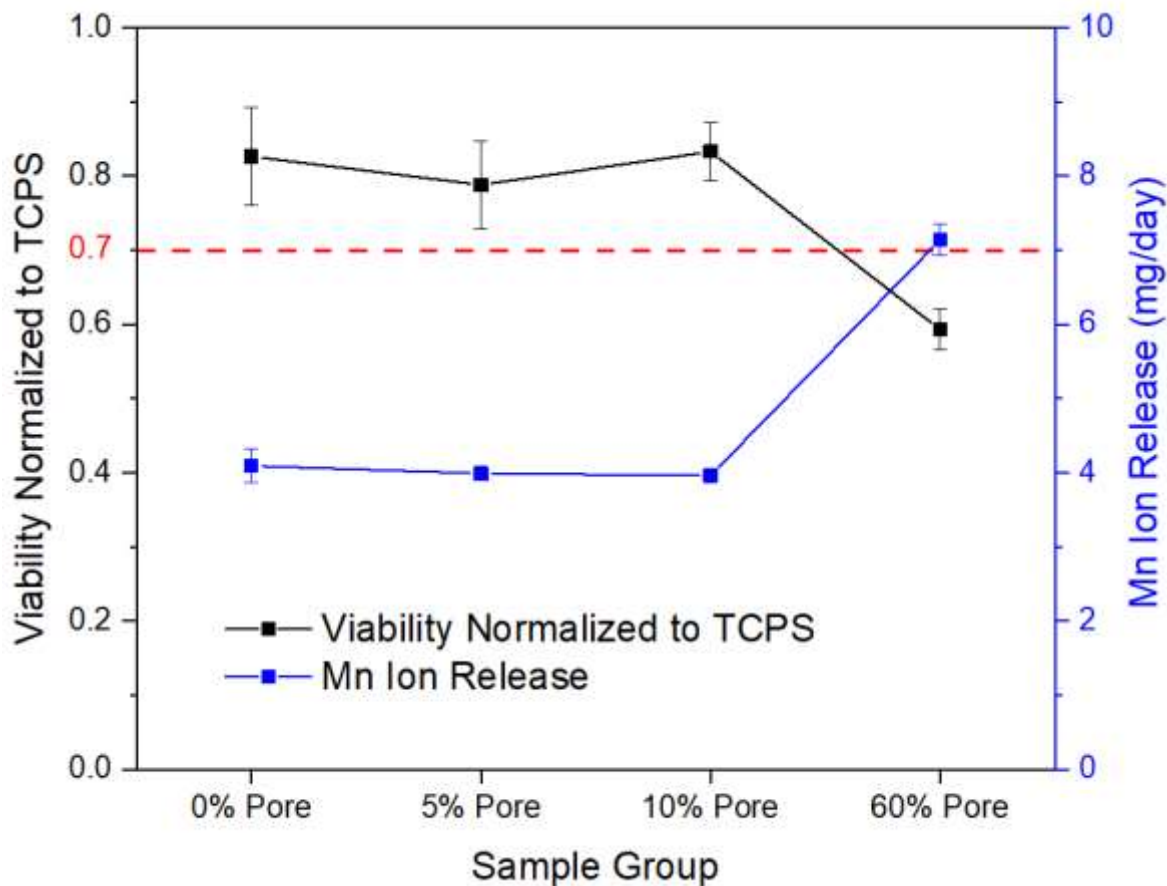
Figure 2.11 Viability of each sample group normalized to TCPS and released Mn ion concentrations corresponding to the group after 1 day of incubation with bone marrow stem cells

A high concentration of Mn ions in low quantities (TC$_{50}$ about 10-100 µM) can result in neurotoxicity linked to Parkinson's disease [51,104]. The recommended dietary allowance (RDA) of Mn is 2.3 mg/day for men and 1.8 mg/day for women [105] with the upper intake level of 5 mg/day [106]. Mn^{2+} release concentration in the 60% pore group is higher than those in the other three groups, which also exceeds the RDA and upper intake level of Mn. Increasing the porosity of the alloy increased the ion release of the alloy and consequently cellular viability decreased. This inverse relationship of ion release and cellular viability needs to be considered when designing an ideal biodegradable metal implant. Although the 60% pore group exhibited a high corrosion rate, leading to a burst release of metal ions leaching into the solution, it caused cellular

toxicity, which hindered its biocompatibility to real applications. On the contrary, the other three groups showed similar ion release rates without cytotoxicity effect. From the combination of ion release rate and cellular viability, scaffolds with 10% porosity presented promising biocompatibility to real applications.

Table 2.3 Average Mn ion release immersed in α-MEM for 1 day and 30 days as well as the normalized cellular viability exposed to 100% and 25% of extract volume

Group	Mn Ion Release (mg/day)		Normalized Viability to TCPS (%)	
	Day 1	Day 30	100% extract volume	25% extract volume
No Pore	$4.10 \pm .2$	$0.68 \pm .28$	86.3 ± 2	137.7 ± 5
5% Pore	$3.99 \pm .1$	$0.26 \pm .05$	75.5 ± 2	93.7 ± 4
10% Pore	$3.96 \pm .0$	$0.21 \pm .04$	85.5 ± 1	61.5 ± 2
60% Pore	$7.14 \pm .2$	$0.83 \pm .03$	57.7 ± 1	51.2 ± 0

2.3.6   Direct Cytotoxicity

Fluorescent cellular morphology after 1 day and 7 days of incubation was shown in Figure 2.12, as a result of direct cytotoxicity test where BMSCs were seeded directly on the sample groups.
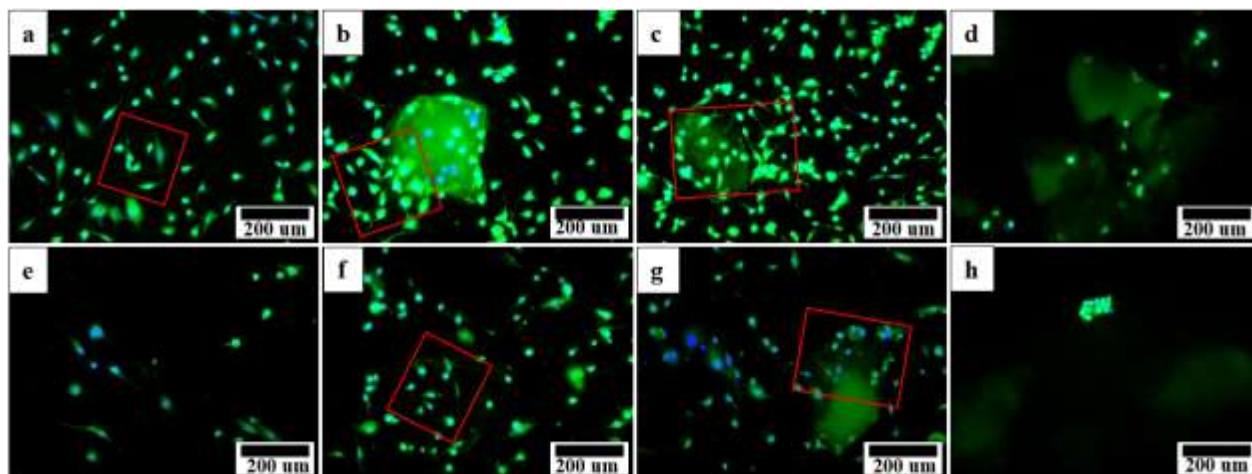
Figure 2.12 Fluorescent images of BMSCs on scaffolds with no pore (a, e), 5-vol% pore (b, f), 10-vol% pore (c, g) and 60-vol% pore (d, h) after 1 day (a-d) and 7 days (e-h) of incubation

After 1 day of incubation, the cell looked healthy on scaffolds that contained porosity no great than 10-vol%, as indicated in Figure 2.12 (a-c), by extending their "arms" or dendrites to reach the other cells. Furthermore, cells penetrated and laid inside macro-pores in the 5% pore and 10% pore group, demonstrating their high affinity to 3D structure than 2D surface like the no-pore group. In contrast, the cells exhibited round shapes in scaffolds contained 60-vol% porosity and were only found inside the pores; the communication activity of cells in scaffolds with 60% porosity appeared to be less than those in scaffolds within 10% porosity.

After 7 days of incubation, 5% pore and 10% pore groups showed higher amounts of cells than the no-pore group and 60% pore group. With increasing porosity, cells looked healthier when there are pores inside the matrix because there are more contact surface points for cells to attach. However, in high porous samples, metal ions and particulates leached out at rates there were too high, so cells were negatively affected. It is also noticeable that number of cells seemed to decrease after 7 days of incubation. However, we speculate that fluorescent dye labelling was hindered or

interfered with calcium-phosphate products depositing on cells and scaffolds. Cellular viability observed in the 5% and 10% pore groups showed promising results and both groups suited for further investigation.

2.4   Summary of Chapter 2

The development of bioresorbable metallic implants aims to provide temporary support and induce defected tissue regeneration where bone cells (osteoclasts and osteoblasts) repeat the processes of resorbing degraded alloy particles and secreting bone layers on the active interface, respectively. We investigated the effect of porosity on properties and biocompatibility of bioresorbable Fe-Mn alloys, a new class of biomaterials for the development of transient orthopedic fixation devices. Similar diffraction patterns of Fe30Mn with various pore concentrations proved the reliability and reproducibility of powder metallurgy techniques. A combination of phase constituents, particle packing factors and degree of porosity affected mechanical properties of the sample groups; scaffolds that contained 10-vol.% NH_4HCO_3 showed greater average values of compressive elastic modulus and ultimate compressive strength compared to the no porosity and 60-vol% porosity groups. Corrosion rates of tested samples increased as the porosity increased and decreased as the incubation time increased. The inverse relationship between corrosion rates and time follows the results from the ion release concentration study, demonstrating the reliability of the study. No cytotoxicity effect appeared to Fe-30%Mn alloys mixed with 5-vol.% and 10-vol.% NH_4HCO_3 through cytotoxicity studies. Scaffolds that contained 60-vol.% porosity exhibited the highest corrosion rates but lowest cell viability. Due to their suitable microstructure, mechanical properties as well as corrosion behavior characteristics, Fe-Mn alloys with 10-vol.% porosity are found to be a new class of promising degradable metallic biomaterials for temporary orthopedic fixation devices.

CHAPTER 3.   ENHANCING OSTEO-INTEGRATION OF FE-30%MN ALLOYS COATED WITH TYPE I COLLAGEN

3.1   Background

Metals have been used in fields of dental, orthopedic, and cardiovascular systems due to their strong mechanical support including high fracture toughness and fatigue limit in tissue anchoring, replacement and regeneration. In recent decades, researchers and scientists focused on developing bioresorbable or biodegradable metals, especially for orthopedic fixation devices such as bone pins, rods, screws, or wires, based on the idea of providing structural support while degrading at a desired period to promote healthy native tissue ingrowth after implantation [107–112]. Magnesium-based alloys and iron-based alloys are the primary biodegradable metals being investigated. Magnesium-based alloys have an elastic moduli and compressive yield strength comparable to natural bone [113]. Nevertheless, magnesium-based alloys exhibit high corrosion rates and create hydrogen bubbles at local sites before complete regeneration in the physiological environment [114]. On the other hand, Fe-based alloys have demonstrated superior mechanical properties that are comparable to 316L stainless steel [115,116], yet their slow degradation [63] limited clinical applications.

Adding 30-wt.% manganese into an iron matrix enhances the corrosion rate, while maintaining mechanical properties of the Fe-30Mn alloy and allows the stabilization of austenitic structure. This is beneficial to obtain an antiferromagnetic behavior [117] that is suitable for magnetic resonance imaging. Incorporation of porosity into the alloy can further speed up the degradation rate of Fe-30Mn alloys. Besides enhancing degradation rates, porosity also helps promoting transport of oxygen and fluid nutrients, encouraging osteointegration and vascular invasion

[118,119]. In the authors' previous study, the effect of the degree of porosity on microstructure, mechanical properties, and corrosion behaviors of Fe-30Mn alloy was investigated, and Fe-30Mn alloys containing 10-vol.% porosity showed suitable mechanical and cytotoxicity compatibility characteristics for use into transient orthopedic fixation devices [120]. However, the Fe-30Mn alloy is inherently bioinert, which only provides non-specific cell adhesion through van der Waals, ionic, and electrostatic forces [110]. Consequently, low osteointegration or cell-alloy interaction is still an issue that needs to be addressed. Improving the osteointegration is therefore the focus of this section of the work.

Several studies have shown that osteointegration can be stimulated by using osteogenic factors, proteins involved in bone healing or components of the extracellular matrix (ECM) [121–123]. The ECM provides specific cell adhesion, which promotes a series of biological cellular activities [124,125] that result in the formation of focal adhesion plaques. The ECM not only improves the cell-alloy adhesion, but it also transduces the chemical signals into the cells [126]. Type I collagen is one of the components in ECM and it is the most abundant protein of the human body consisting of three polypeptide chains. Each polypeptide chain is composed of at least one Gly–X–Y sequence where the X and Y positions are usually proline and hydroxyproline, respectively, in a left-handed α-like helices structure [127]. These three α-like helices are organized together to form the characteristic structure of collagen, a right-handed triple helix. Coating of Type I collagen on titanium- and cobalt-based alloys has been found to accelerate initial adhesion of osteoblasts and promote cellular spreading [128–130]. Depending on the effectiveness of collagen coating, it promotes cell-implant interactions on permanent titanium- and cobalt-based implants, and the hypothesis is that coating of Type I collagen can enhance the osteointegration of Fe-30Mn alloys.

In this study, we performed two tests that aim to understand the role of collagen coating on Fe-30Mn alloys using two different techniques – drop deposition and spin coating. Subsequently, we evaluated the quantitative cytotoxicity level of degradable non-porous and porous Fe-30Mn alloys with and without collagen coating after one day of incubation. Furthermore, cell adhesion, spreading, proliferation and morphology on alloys was also qualitatively investigated for a period of 7 days. This study, to the authors' knowledge, is the first to investigate the effectiveness of collagen coating on Fe-30Mn alloys towards understanding of the interactions of bone marrow stromal cells (BMSCs) with Fe-Mn alloys.

3.2   Materials and Methods

3.2.1   Sample Fabrication

The fabrication of non-porous and porous Fe-30Mn alloy substrates was demonstrated in the authors' previous paper [120]. A mixture of iron and manganese powders in a weight ratio of 7:3 was mixed and spun in a high-speed mixer at 800 rpm for 15 mins. To prepare non-porous Fe-30Mn samples, half of the mixture was aliquoted and cold pressed. To prepare porous Fe-30Mn samples, the other half of the mixture was mixed with 10-vol.% of ammonium bicarbonate, spun with an addition of 10-wt.% of ethanol, and then aliquoted and followed by cold pressed. In the sintering process, the green compacts for porous Fe-30Mn samples were loaded in a muffle furnace, heat treated at 120°C for 2 hours, subsequently treated at 1200°C for 3 hours, and finally cooled to room temperature. The green compacts for non-porous Fe-30Mn samples were sintered at 1200°C for 3 hours and cooled to room temperature. All samples were sintered with a heating rate of 10°C/min under argon atmosphere. After sintering, all Fe-30Mn samples were mechanically ground with silicon carbide paper in a grit size of 2000, ultrasonically cleaned in ethanol for 10 minutes, and stored in a desiccator for further testing.

For the reference Ti6Al4V samples, standard Grade 5 Ti6Al4V (ASM Aerospace Specification Metals; Florida) rods were cut and ground to obtain a disk-shaped sample size of 12.7 mm in diameter and 1.3 mm in thickness. The Ti6Al4V samples were also mechanically ground to 2000 grit, ultrasonically cleaned in ethanol, and stored in a desiccator for further testing.

3.2.2   Collagen Coating Solution Preparation

The collagen-fibril solution was prepared according to the study of Loo et. al. [131]. In brief, monomer Type I collagen solution (Advanced Biomatrix; California) was added to a buffer solution containing deionized water, 200 mM sodium phosphate dibasic adjusted to pH 7 with hydrochloric acid, and 400 mM potassium chloride, to achieve a concentration of ~0.3 mg/ml monomer collagen solution.

3.2.2.1   Collagen Coating via Physical Drop Deposition

The solution containing monomer collagen was placed in a heat block maintaining at 37°C for at least 6 hours for the assembly of fibrillar collagen. After collagen fibrils formed in solution, porous Fe-30Mn samples were coated by dropping the solution "freely" on top of the alloy surface and allowed the solution to dry overnight so that only collagen fibrils remained on the alloy surface. We named this technique physical drop deposition (DD). Table 1 the optimization parameters for the DD coating of Type I collagen on porous Fe-30Mn substrates. Infrared absorption spectra of the coated samples prepared from Table 1 were obtained using a Fourier-transform infrared spectroscopy (FTIR; Spectrum 100). Surface microstructures and compositions of the coated samples were examined using an optical microscope and a scanning electron microscope (SEM; FEI Philips XL-40) coupled with energy dispersive x-ray spectroscopy (EDS).

3.2.2.2   Collagen Coating via Spin Coating

In another set of experiments, porous Fe30Mn samples were coated with Type I collagen using the

spin coating (SC). These experiments were performed to eliminate the interference of buffer

solution on samples, which was observed for the physical drop deposition. Table 2 shows the spin

coating parameters. Every Fe-30Mn porous sample was centered on a spin coater and 100 µl of

collagen fibrils solution was dispensed on the substrate carefully to achieve a full coverage. After

spin coating, samples were examined using the SEM. Based on the homogenous collagen coating

observed in SC2 and SC3 groups, four additional sample groups were spun coated at a spin speed

of 4000, 4250, 4500, and 5000 rpm, respectively, for 30 seconds. These additional samples were

examined in a cell culture test after one day of incubation. The spin speed of 4250 rpm for 30

seconds was selected as final spin coating parameters for both experimental Fe-30Mn and control

Ti6Al4V samples for electrochemical corrosion and in-vitro cytotoxicity testing.

3.2.3   Potentiodynamic Polarization Test

Four experimental groups, non-porous (NP-NC), porous (10P-NC), collagen-coated non-porous

(NP-C), and collagen-coated porous (10P-C) Fe30Mn samples were prepared by the methods

described in Sections 2.1 and 2.2. The potentiodynamic corrosion testing was conducted using the

same method demonstrated in the previous study [120]. In brief, every sample was mounted,

cleaned with DI water, and exposed to the electrolyte McCoy's 5A (ATCC, Virginia) at 37 ± 2 °C.

The current at the sample was recorded when the sample was applied to the potential scan from -

0.15 V to + 0.15 V at a rate of 0.1667 mV/s. Using the Tafel curve, the corrosion potential and

corrosion current were determined. Consequently, the corrosion rate of each sample was calculated

using equation Eq. 2.1. The average surface area containing porosity of each group was calculated

using ImageJ [81] with adjusted binary threshold. The surface area (SA) of each sample was calculated using equation Eq. 2.2.

3.2.4 *In-Vitro* Cell Culture

Four experimental Fe30Mn groups (NP-NC, 10P-NC, NP-C, 10P-C) and two control Ti6Al4V groups (CT-NC, CT-C) were tested in the direct cytotoxicity test. All samples were exposed to UV light for 1.5 hours (1 hour for the seeding surface and 0.5 hour for the opposite side) for sterilization. Each sample was placed in a 24-well plate and rinsed with cell culture media (McCoy's 5A supplemented with 10% fetal bovine serum, 5% Penicillin Streptomycin, and 0.5% Fungizone) prior to cell seeding. Mouse bone marrow stromal cells (BMSC; ATCC, D1 ORL UVA) within passage number 10-15 were seeded on each sample in a density of 5×10^4 cells/well and the cell-scaffold composite was subsequently placed inside an incubator mimicking the physiological environment (pH = 7, 5% CO_2, $37.5 \pm 0.5°C$) for 1, 3, and 7 days.

3.2.4.1 Direct Cytotoxicity Test

After one day of incubation, the cytotoxicity level was evaluated by conducting a colorimetric cytotoxicity assay kit (Promega, CytoTox96® Non-Radioactive Cytotoxicity Assay). The assay measured quantitatively the amount of lactate dehydrogenase (LDH) in the culture supernatants by measuring the optical density (OD) reading of a formazan product, which was the reduction form of a tetrazolium compound [iodonitro-tetrazolium violet; INT] using a VersamaxTM absorbance microplate reader (Molecular Devices; California). The quantity of the formazan product was proportional to the number of lysed cells on OD at 490nm. According to the manufacturer's protocol, the toxicity of every sample was calculated by the following equation:

$$Percent\ Cytoxicity = 100 \times \frac{\text{Experimental LDH Release (OD)}}{\text{Maximum LDH Release (OD)}} --- Eq.\ 3.1$$

, where maximum LDH release is the absorbance of lysis solution provided from the kit.

3.2.4.2 Fluorescent Staining

After 1, 3, and 7 days of incubation, the cellular morphology and viability were observed by labelling plasma membrane with 1X of CellMask™ Plasma Membrane Stain (Life Technologies, Grand Island, NY) and nuclei with 0.1 ug/ml of Hoechst Fluorescent Stain (ThermoFisher Scientific, Waltham, MA). Samples were stained for 30 minutes and rinsed with Live Cell Imaging Solution (ThermoFisher Scientific, Waltham, MA) three times to wash the excessive dye. The samples were examined using a fluorescent microscope where the plasma membrane and nuclei of cells were observed in fluorescence emission spectra of green and blue, respectively. The cell count and size for each group were measured using ImageJ where the image sample size was 20 (n = 20) and the count was normalized to the number of cells per square millimeter.

3.2.4.3 Sample Processing for SEM

On the third day of incubation, the experimental groups were rinsed with PBS three times and filled with 2.5% glutaraldehyde for fixation. The samples were then processed into DI water rinse, 1% osmium tetroxide, DI water rinse, ethanolic dehydration, and critical point drying as the final step. Consequently, samples that preserved cellular morphology were sputter coated with platinum and examined using a SEM microscope (Nova NanoSEM™; FEI).

3.2.5 Statistical Analysis

A minimum of three replicates of the sample group (n = 3) were conducted for every experiment. Quantitative data from each test were collected and compared using Student's t-test. The differences between the studied groups were evaluated through a one-way analysis of variance

(ANOVA) in a statistical analysis software (jmp). A threshold of $\alpha = 0.05$ was set to determine statistical significance.

3.3 Results

3.3.1 Type I Collagen Coating Characterization

3.3.1.1 Drop Deposition Coating

Infrared absorption spectrum of Type 1 collagen on which Fe-30Mn substrates coated was displayed in Figure 3.1.
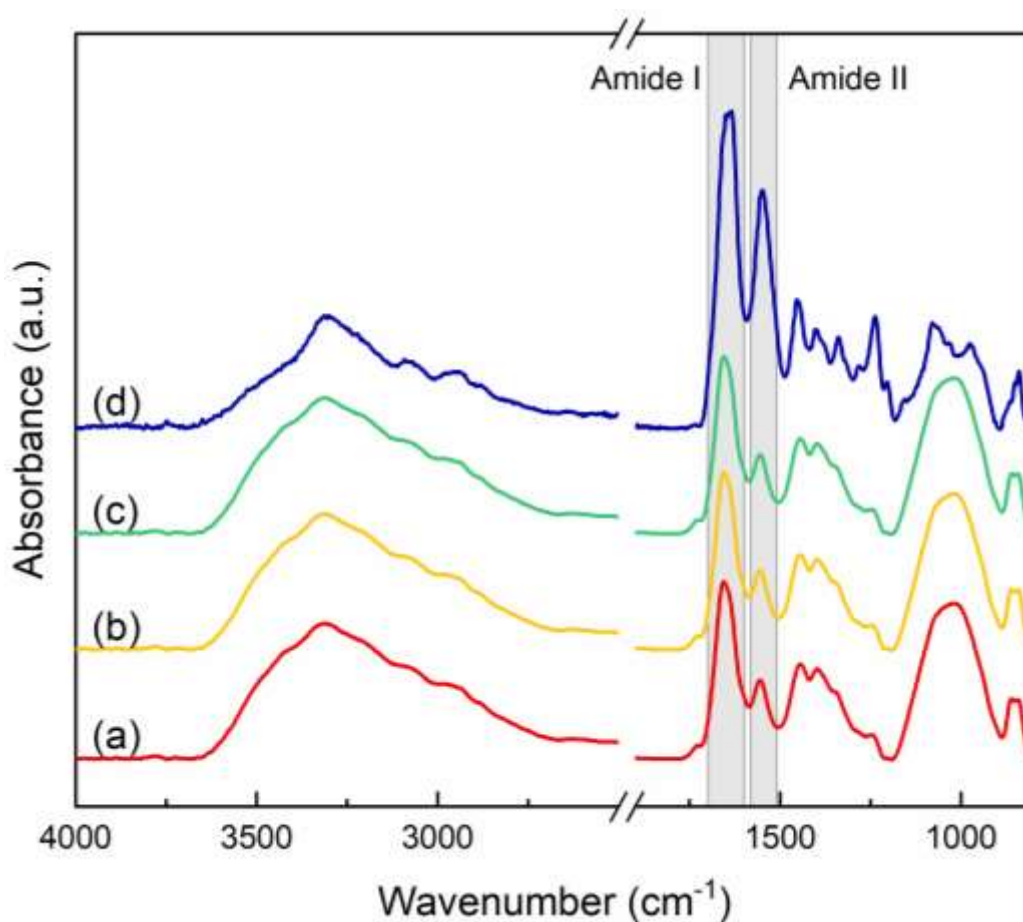
Figure 3.1 FTIR spectrum of collagen-coated samples prepared from Table 3.1: (a) DD1; 6 hours of fibril collagen self-assembled time and 90 μl of drop solution drying at 4 ˚C, (b) DD2; 6 hours of fibril collagen self-assembled time and 90 μl of drop solution drying at 25 ˚C, (c) DD3; 12 hours of fibril collagen self-assembled time and 90 μl of drop solution drying at 25 ˚C, and (d) DD4; 12 hours of fibril collagen self-assembled time and 200 μl of drop solution drying at 25 ˚C

All samples prepared by different coating parameters listed in Table 3.1 showed consistent amide I band and amide II band peaks at 1637 cm^{-1} and 1546 cm^{-1} wavenumbers, respectively. Observation of both amide I and amide II band peaks in this study follows observation of those in references [132,133].

Table 3.1 Collagen coating design for Fe-30Mn substrates using the physical drop deposition (DD) technique; all coated Fe-30Mn samples contained 10% pore

Sample Group	Self-Assembly Time (hours)	Drying Temperature after Coating (˚C)	Volume of Solution Drop (µl)
DD1	6	4	90
DD2	6	25	90
DD3	12	25	90
DD4	12	25	200

Since similar edge morphology of each group was observed using SEM, only the edging surface and chemical composition of DD2 (6 hours of fibril collagen self-assembled time and 90 µl of drop solution drying at 25 ˚C) was displayed as representative in Figure 3.2. At the top-left corner of the SEM image in Figure 3.2, the edge of the sample was iron (Fe) and manganese (Mn) rich, representing the original Fe-30Mn substrate. Toward the edge of the sample, cracks or fragments of bumps were observed. Those bumps were particularly sodium (Na) and phosphorus (P) rich, which were the main elements in the buffer solution that contained the fibrillar collagen. Since bumps on Fe-30Mn samples were observed after coating, and those bumps resulted from the collagen buffer solution, we concluded that the excess of buffer solution interacted with the surface of Fe-30Mn sample during the overnight drying process.
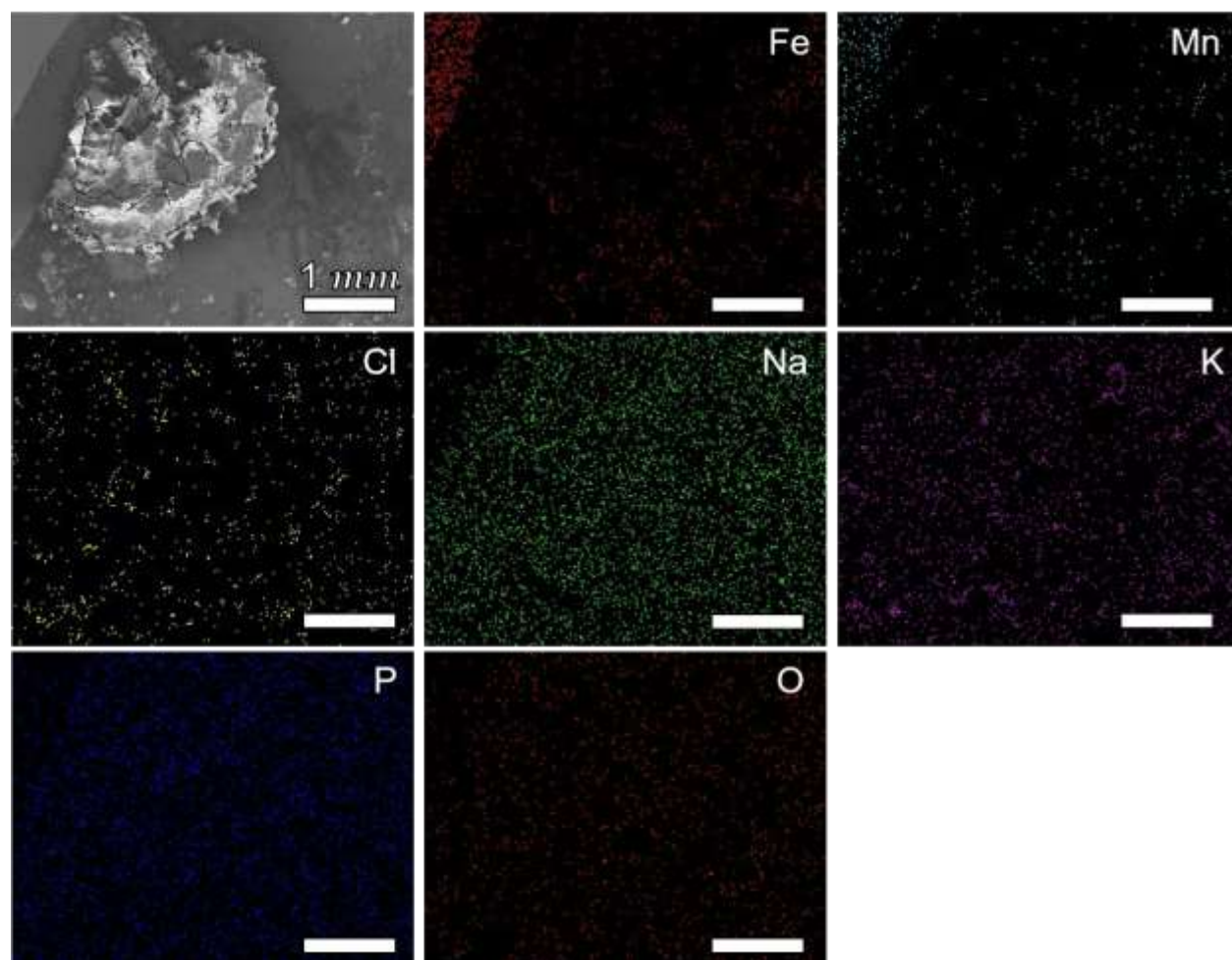
Figure 3.2 EDS map analysis of DD2 sample (Fe-30Mn substrate coated with Type I collagen; 6 hours of fibril collagen self-assembled time and 90 μl of drop solution drying at 25 ˚C). Cracking bumps on the surface of the sample were sodium and phosphorus rich. The length of each scale bar is 1 mm

3.3.1.2   Spin Coating

Figure 3.3 showed SEM images of collagen-coated Fe-30Mn samples using the spin coating technique. Collagen was observed in all samples prepared by different spinning time and speeds according to Table 3.2. However, homogeneous collagen bundles were only observed in SC2 (spun at a spinning speed of 5000 rpm for 30 seconds) and SC3 (spun at a spinning speed of 4000 rpm for 30 seconds) samples. At a high spin speed of 6000 rpm, bundles of fibrillar collagen were observed in Figure 3. (a). In Figure 3.3. (d), amorphous "coral" and "mat" structures of collagen were observed for the sample spun at a combination of low spin speed of 3000 rpm and high spin speed of 6000 rpm.

Table 3.2 Collagen coating design for Fe-30Mn substrates using the spin coating (SC) technique. All coated Fe-30Mn samples contained 10-vol.% pore and were spun with 100 μl of solution that contained fibril collagen prepared after 12 hours of self-assembled time

Sample Group	Solution Spinning Time (s)	Solution Spinning Speed (rpm)
SC1	30	6000
SC2	30	5000
SC3	30	4000
SC4	20/40	3000/6000

To identify the ideal spin coating parameters that are most likely to promote cellular viability, a cell culture test for porous Fe-30Mn samples spun coated at 4000, 4250, 4500, and 5000 rpm for 30 seconds was conducted. In Figure 3.4, fluorescent images of bone marrow stems cells (BMSCs) are visible on Fe30Mn samples. Here, the Fe-30Mn samples spun coated at 4250 rpm for 30 seconds showed the highest cellular activity of the group. For the Fe-30Mn sample spun coated at

4250 rpm, BMSCs extended their dendrites (plasma membrane labeled in green) out to communicate with the other cells, indicating promising cellular interaction.
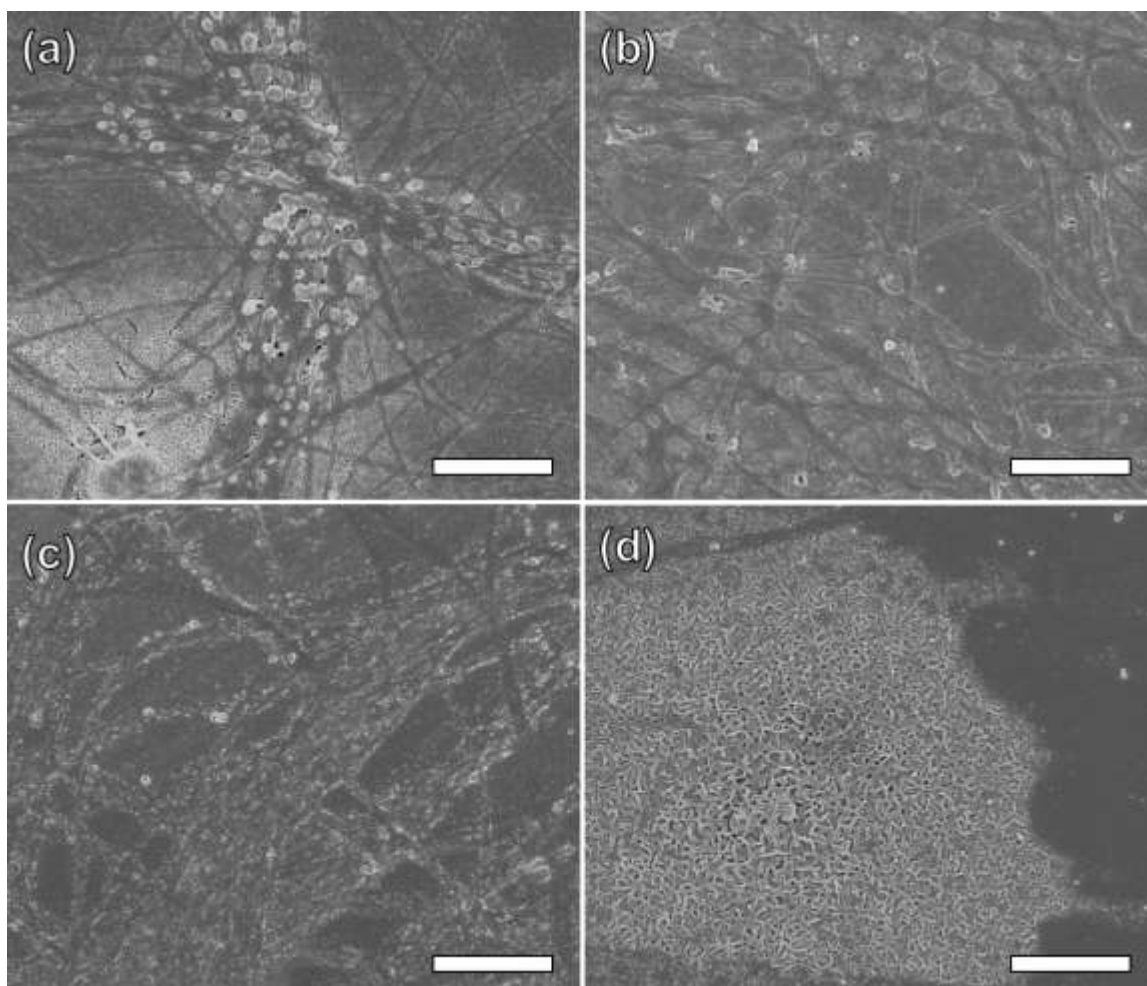
Figure 3.3 SEM images of collagen-coated Fe-30Mn samples prepared from Table 3.2: (a) SC1; spun at a spinning speed of 6000 rpm for 30 seconds, (b) SC2; spun at a spinning speed of 5000 rpm for 30 seconds, (c) SC3; spun at a spinning speed of 4000 rpm for 30 seconds, and (d) SC4; spun at a spinning speed of 3000 rpm for 20 seconds and subsequently spun at a spinning speed of 6000 rpm for 40 seconds. The length of each scale bar is 3 µm
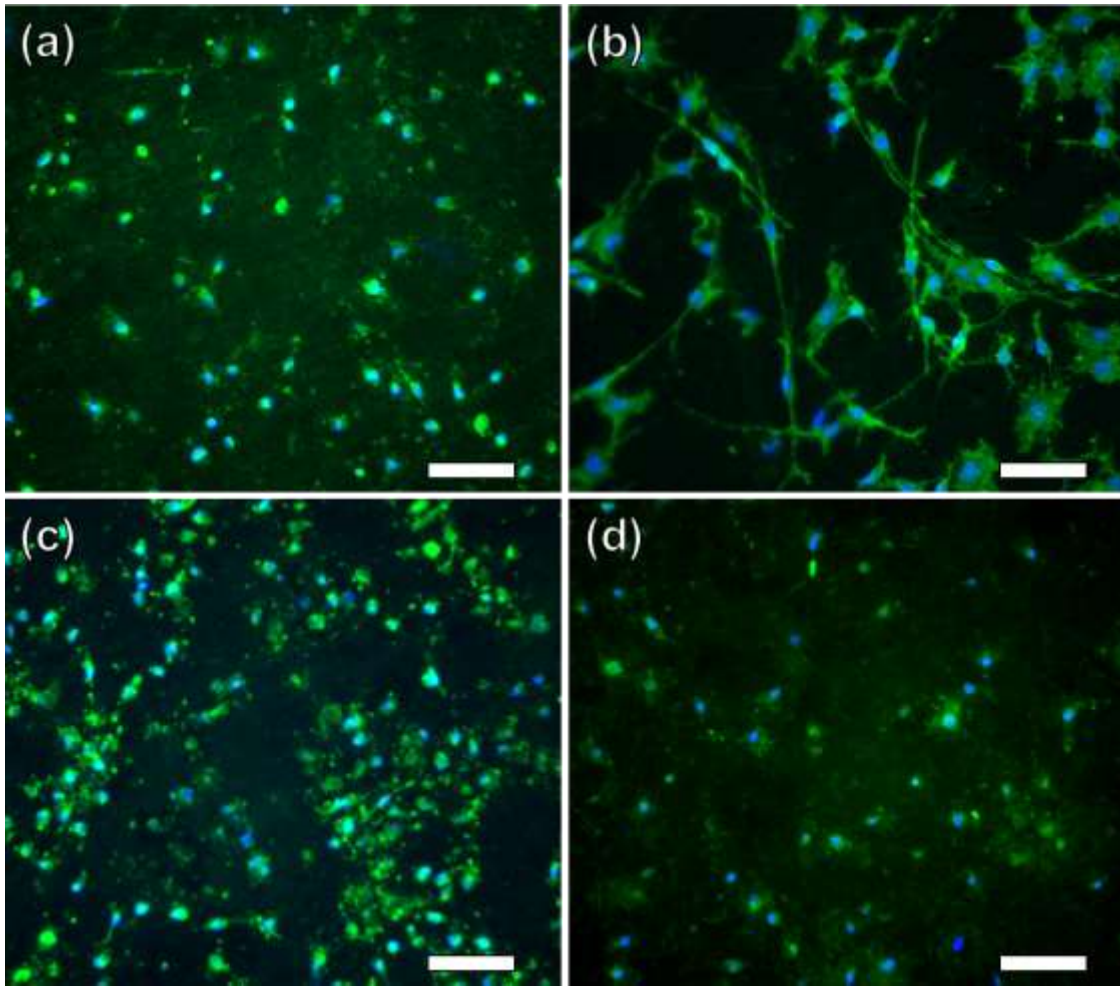
Figure 3.4 Fluorescent images of bone marrow stem cells (BMSCs) on porous Fe-30Mn samples coated with Type I collagen at the spinning speed of (a) 4000 rpm, (b) 4250 rpm, (c) 4500 rpm, and (d) 5000 rpm after 1 day of incubation. The length of each scale bar is 100 µm

3.3.2   Potentiodynamic Polarization Test

Once the coating parameter was determined, the electrochemical corrosion test was conducted to examine the effect of collagen coating on the corrosion rate of Fe-30Mn samples. Figure 3.5 showed the representative Tafel curves of experimental Fe30Mn groups: Fe-30Mn without collagen coating (NP-NC), porous Fe30Mn without collagen coating (10P-NC), Fe-30Mn with collagen coating (NP-C), and porous Fe30Mn with collagen coating (10P-C).

Figure 3.5 Representative potentiodynamic polarization curves of the experimental Fe-30Mn groups in McCoy's 5A medium (pH 7.4) at 37 ± 2 °C. The squares represented Fe30Mn without collagen coating (NP-NC), circles represented Fe-30Mn with collagen coating (NP-C), upward triangles represented porous Fe-30Mn without collagen coating (10P-NC), and downward triangles represented porous Fe-30Mn with collagen coating (10P-C)

The average corrosion potential (E_{corr}), corrosion current density (I_{corr}), and corrosion rate (CR) for the experimental Fe30Mn groups were also listed in Table 3.3. Average corrosion rate ranked from high to low was 10P-NC > 10P-C > NP-NC > NP-C. Although corrosion rates of collagen-coated samples were lower than those of non-collagen coated ones, this decrease in corrosion rate was not significant at the 0.05 level, indicating coating collagen did not have significant effect on corrosion rate for Fe30Mn samples.

Table 3.3 Average sample corrosion potentials (E_{corr}), corrosion current densities (I_{corr}), corrosion rates (CR_p) obtained from the potentiodynamic polarization curves.

Sample Group	Description	E_{corr} (V)	I_{corr} ($\mu A/cm^2$)	CR (mmpy)
NP-NC	Non-porous, no collagen coating Fe-30Mn	-0.741 ± .07	1.57 ± 1.1	0.022 ± .02
10P-NC	10% pore, no collagen coating Fe-30Mn	-0.802 ± .06	2.84 ± 1.6	0.040 ± .02
NP-C	Non-porous, collagen coated Fe-30Mn	-0.947 ± .47	1.47 ± 0.8	0.020 ± .01
10P-C	10% pore, collagen coated Fe-30Mn	-0.921 ± .19	1.96 ± 0.8	0.028 ± .01

3.3.3   Direct *In-Vitro* Cytotoxicity Test

For the cytotoxicity test, four experimental Fe30Mn groups (NP-NC, 10P-NC, NP-C, and 10P-C) as well as two control Ti6Al4V groups (CT-NC and CT-C) were investigated after one day of incubation with BMSCs.

3.3.3.1   Cytotox96 Cytotoxicity Test

After 1 day of incubation, the cytotoxicity effect of the four experimental Fe-30Mn groups and two control Ti6Al4V groups on BMSCs were evaluated and compared. The numerical average and standard deviation values of percent cytotoxicity for each group were listed in Table 3.4 and plotted in Figure 3.6.

Table 3.4 Average sample cytotoxicity levels after 1 day of incubation as well as average cell counts and sizes after 1 and 3 days of incubation

Sample Group	Cytotoxicity Level (%)	Count (# / mm^2)		Size (µm)	
		Day 1	Day 3	Day 1	Day 3
NP-NC	6.20 ± 2.4	855 ± 277	3622 ± 736	67 ± 16	76 ± 16
NP-C	1.80 ± 1.8	2599 ± 266	6273 ± 454	82 ± 13	56 ± 9
10P-NC	14.97 ± 5.3	650 ± 567	1599 ± 663	54 ± 10	72 ± 22
10P-C	9.08 ± 3.5	2376 ± 401	3984 ± 673	66 ± 10	38 ± 7
CT-NC	3.56 ± 0.9	703 ± 299	6856 ± 514	57 ± 11	39 ± 8
CT-C	2.57 ± 2.0	892 ± 180	6712 ± 1098	84 ± 10	40 ± 2.0
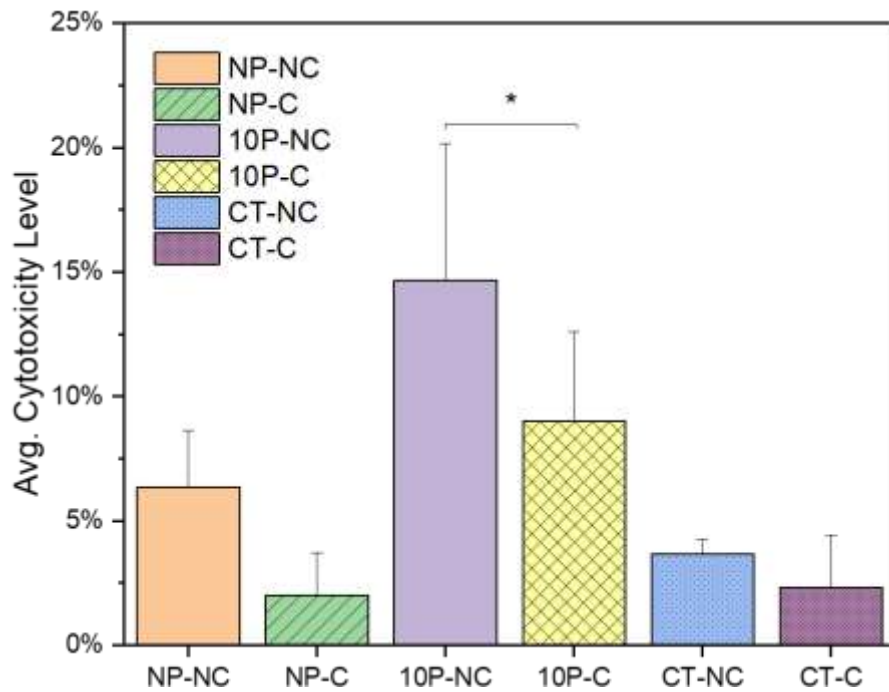
Figure 3.6 Cytotoxicity level of the studied groups on bone marrow stem cells (BMSCs) after 1 day of incubation. The experimental groups were Fe-30Mn without collagen coating (NP-NC), Fe-30Mn with collagen coating (NP-C), porous Fe-30Mn without collagen coating (10P-NC), and por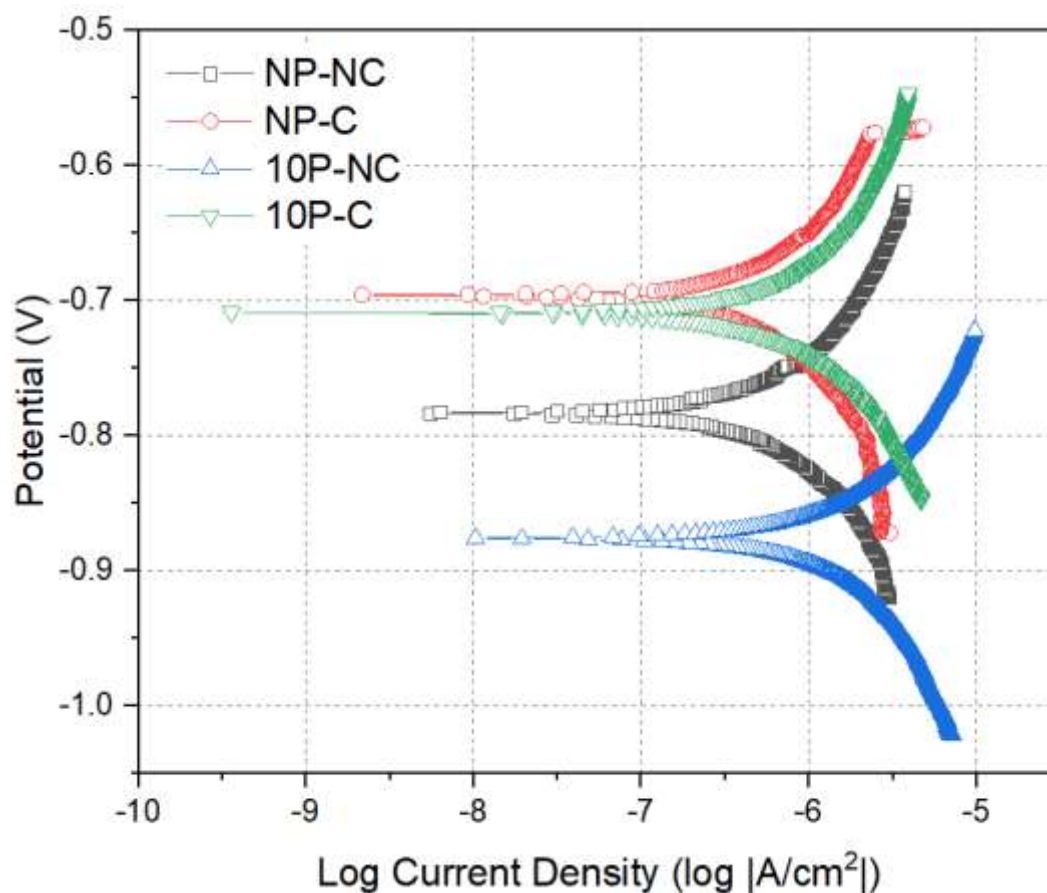ous Fe-30Mn with collagen coating (10P-C). The control groups were Ti6Al4V without and with collagen coating (CT-NC and CT-C, respectively). The bracket with the asterisk mark indicated the significant difference between the 10P-NC and 10P-C groups ($\alpha < 0.05$)

The average cytotoxicity level was 14.97 % for the non-coated porous group (10P-NC), representing the highest level of cytotoxicity effect, and 1.80 % for the coated non-porous group (NP-C), representing the lowest level of cytotoxicity effect. A significant decrease in the cytotoxicity level from the non-coated porous group (10P-NC) to the coated porous group (10P-C) was found. There was no significant difference between the non-porous Fe-30Mn groups (NP-NC and NP-C) in the cytotoxicity level, neither was the significant difference between the control Ti6Al4V groups (CT-NC and CT-C).

3.3.3.2   Cellular Behavior

Qualitative evaluation of cell morphology, detachment, and membrane integrity for each experimental group were examined after 1, 3 and 7 days of incubation, as displayed in Figure 3.7. On day 1, cells appeared to be the healthiest on the coated non-porous group (NP-C) and the unhealthiest on the non-coated porous group (10P-NC). On day 3, BMSCs seeded on the collagen-coated Fe-30Mn groups (NP-C and 10P-C) were grown to achieve a higher confluency than those seeded on the non-coated groups (NP-NC and 10P-NC), respectively. As the culture time reached to day 7, BMSCs were grown to 100% confluency for all Fe30Mn groups except for the 10P-NC group.

Figure 3.8 shows the average cell count (a) and size (b) after 1 and 3 days of incubation. The corresponding numerical values are listed in Table 3.4. Compared to the non-coated Fe-30Mn groups, the collagen-coated Fe-30Mn groups showed significant increases in the average cell count and size within 24 hours. After 3 days of incubation, there was no significant difference in the cell count between the coated non-porous Fe30Mn group (NP-C) and the control Ti6Al4V groups (CT-NC and CT-C).
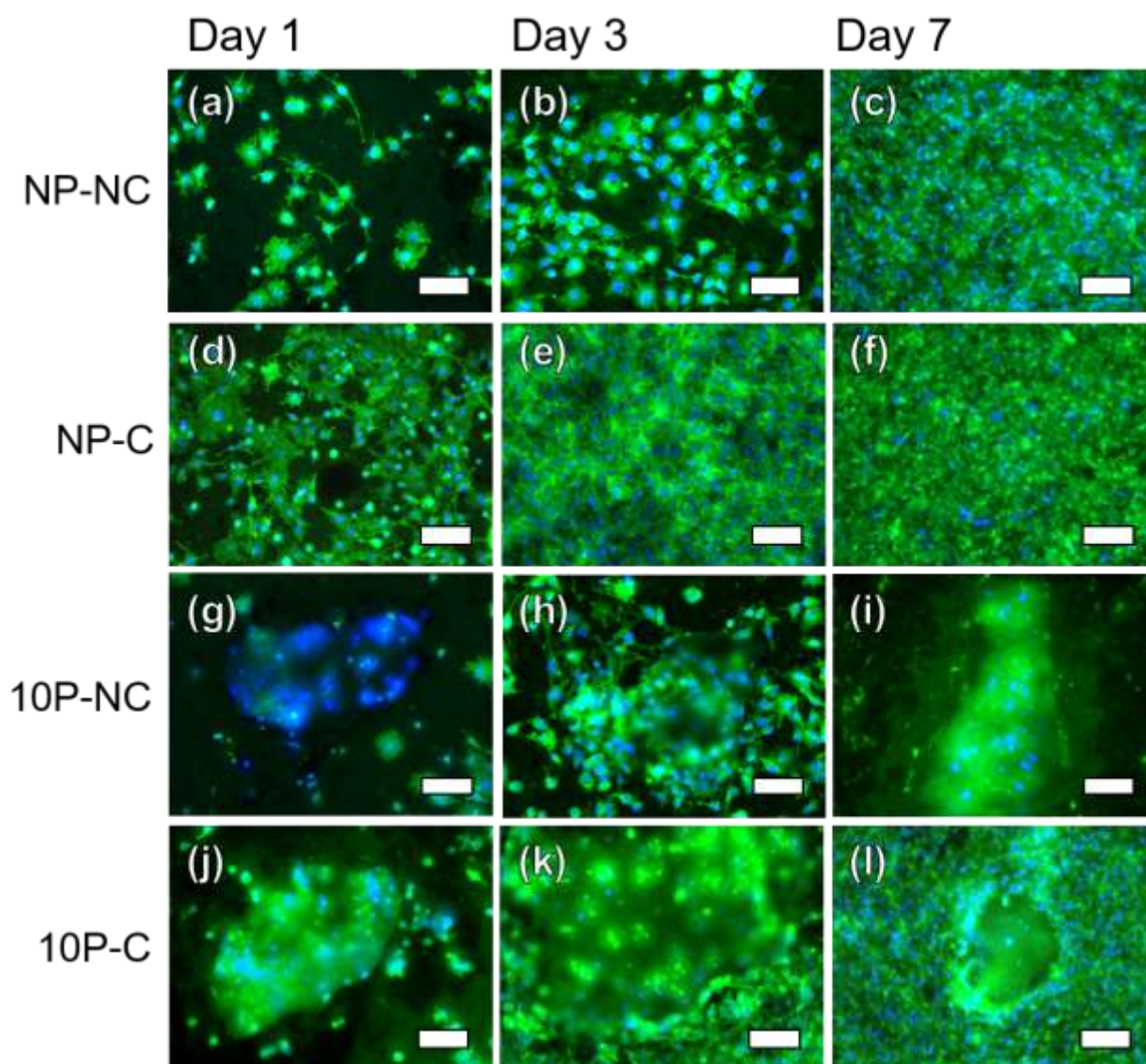
Figure 3.7 Fluorescent images of BMSCs on the studied experimental groups: (a-c) NP-NC, (d-f) NP-C, (g-i) 10P-NC, and (j-l) 10P-C scaffolds after 1 day (a, d g, j), 3 days (b, e, h, k), and 7 days (c, f, i, l) of incubation. The length of each scale bar is 100 µm
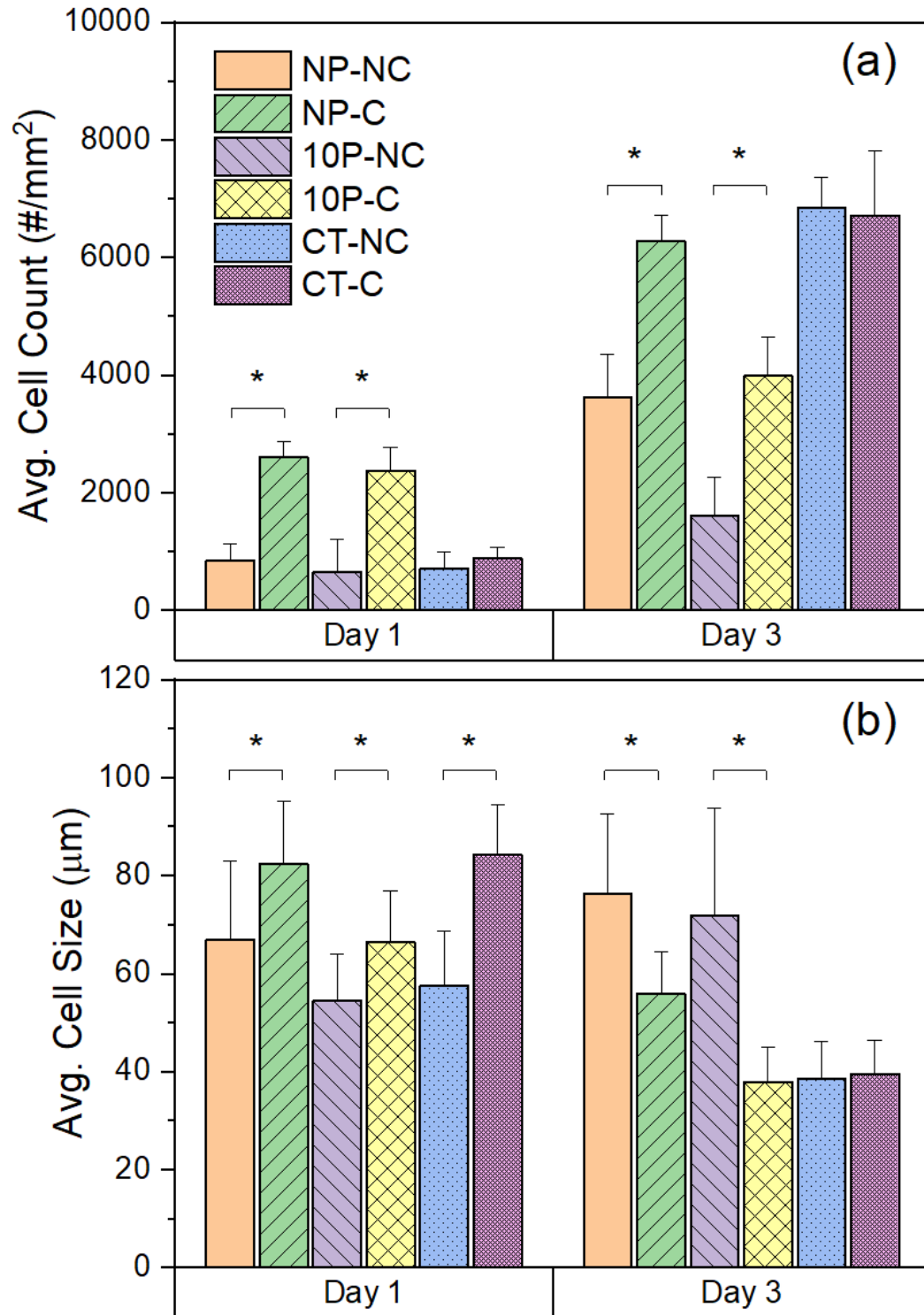
Figure 3.8 Average bone marrow stem cell count (a) and size (b) distributed on the studied groups after 1 and 3 days. The bracket with the asterisk mark indicated the significant differences among the collagen-coated and non-coated groups ($\alpha < 0.05$)

Figure 3.9 shows qualitative SEM images of cells on each experimental group after 3 days of incubation. Cells adhered to the NP-NC, NP-C and 10P-C groups appeared flattened, spreading thin extensions to reach out other cells. For the 10P-NC group, cells sat erect on the surface of scaffold, indicating loose-attachment.
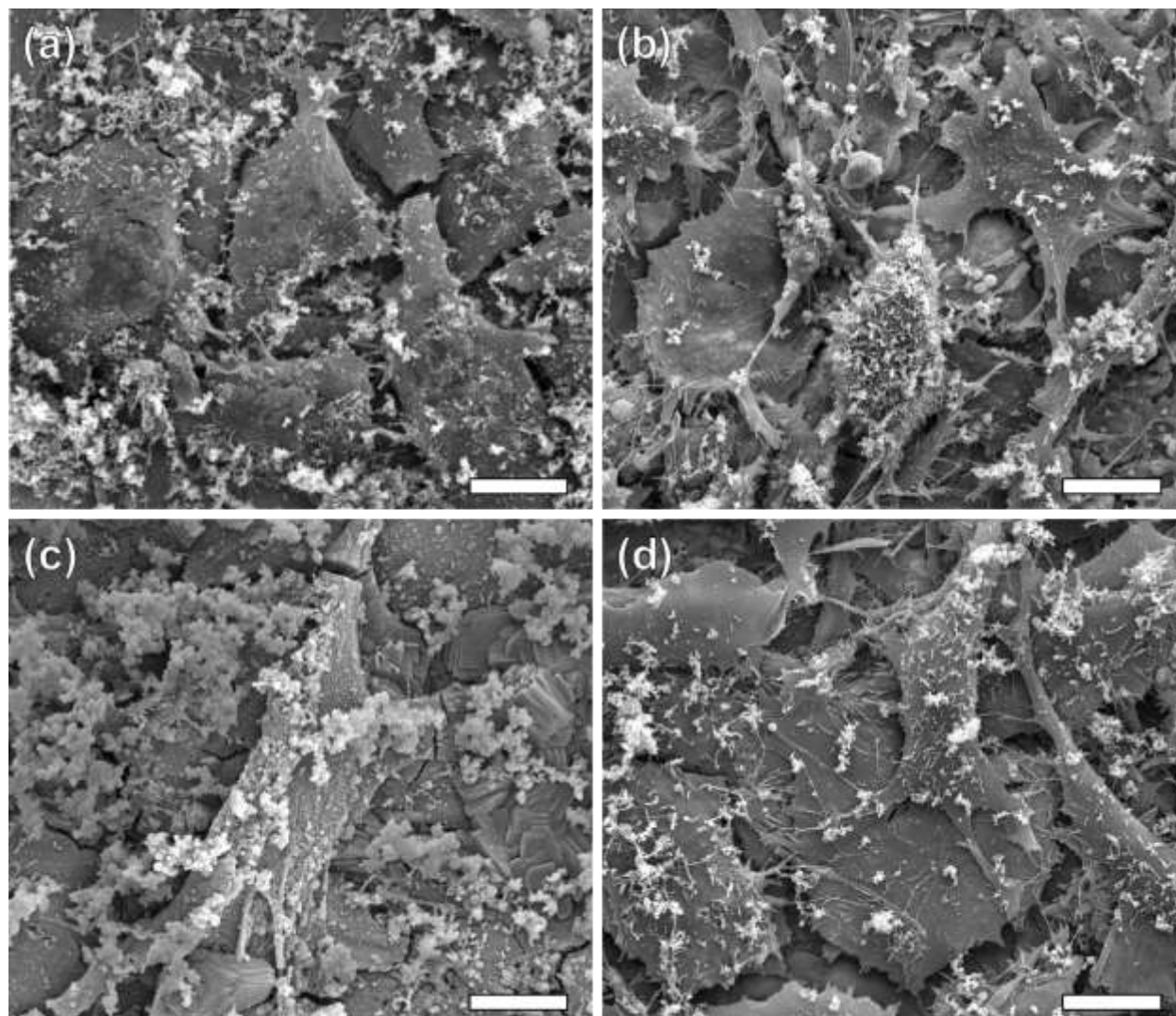
Figure 3.9 SEM images of BMSCs on the experimental groups: (a) NP-NC, (b) NP-C, (c) 10P-NC, and (d) 10P-C scaffolds after 3 days of incubation. The length of each scale bar is 10 µm

Further comparison of cell morphology on the 10P-NC and 10P-C groups is displayed in Figure 3.10. No cell was observed at the edge of the pore on the 10P-NC sample (Figure 3.10a), while flattened cells were observed surrounding and even covering the entire pore (Figure 3.10c). The profound difference in cell morphology between the porous non-collagen-coated group (10P-NC) and porous collagen-coated group (10P-C) demonstrated that the collagen coating was necessary for porous Fe30Mn to make cells show healthy discrete intracytoplasmatic granules.
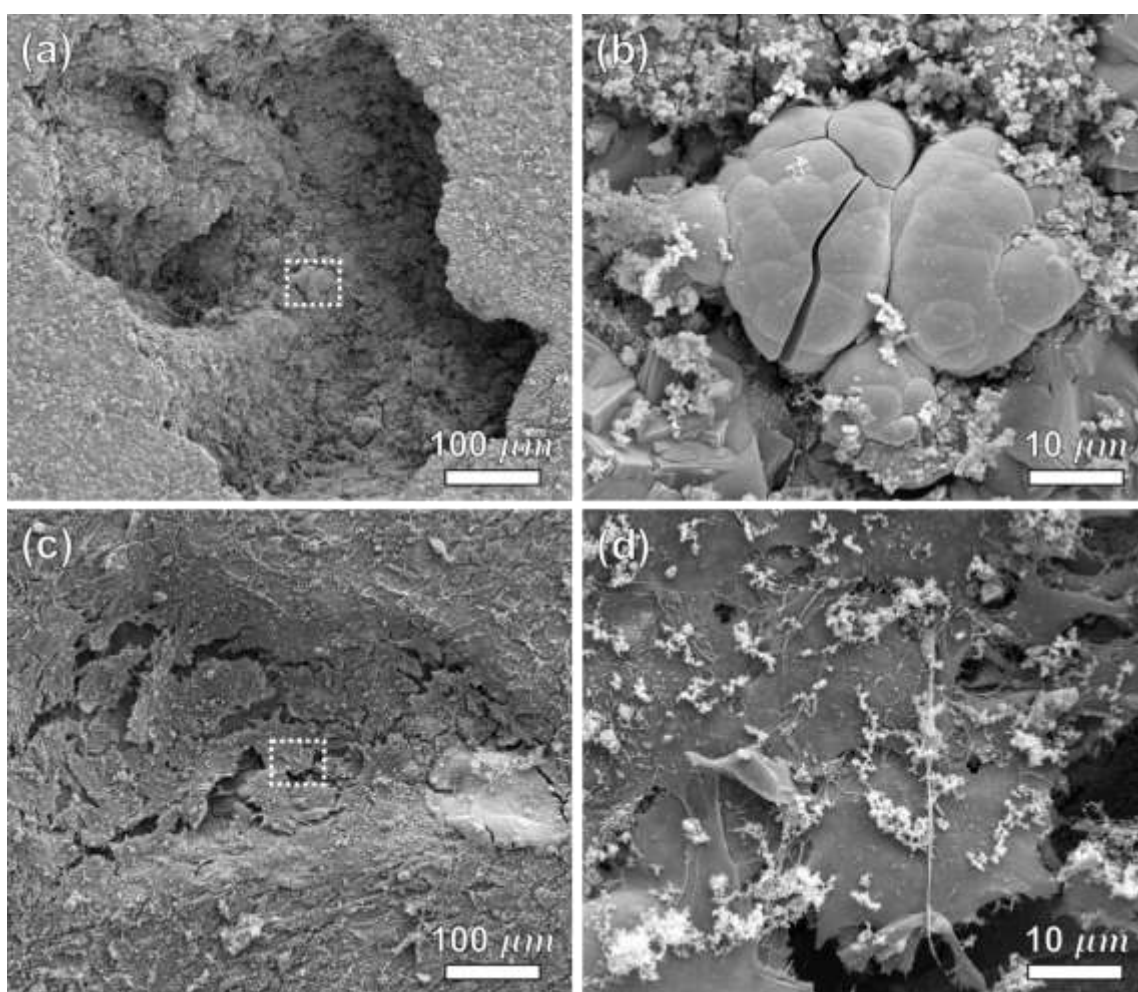
Figure 3.10 SEM images of BMSCs on (a-b) 10P-NC and (c-d) 10P-C scaffolds after 3 days of incubation at different magnifications. The dashed white boxes inside (a) and (b) were zoomed to (c) and (d), respectively, to show different morphologies of BMSCs

3.4   Discussion

Fe-30Mn samples coated by fibrillar Type I collagen using the drop deposition technique showed similar absorption IR spectrum containing both amide I and amide II band peaks. Detection of amide I and amide II peaks on all collagen-coated samples using the drop deposition technique demonstrated that collagen adsorbed on the alloy substrate successfully. Nevertheless, flaky cracks appeared close to the edge of the sample after coating and drying overnight. The authors initially suspected the cracks were metal hydroxides [6,36] resulting from the electrochemical reactions between the alloy and buffer solution. However, EDS results showed that the cracks were sodium and phosphate rich instead of iron and manganese rich, suggesting that the occurrence of cracks was merely caused by the buffer solution. The excess of fibrillar collagen buffer solution returned salts to their anhydrous forms after allowing the solution to dry naturally, leaving segregated salts on the surface of the sample.

Since samples prepared from drop deposition showed inhomogeneous coating due to excess of buffer solution, spin coating was used to quickly remove the buffer solution and obtain homogenous collagen Type I coverage. Although spin coating prevented salt residues remaining on samples, coating uniformity was complex and difficult to achieve. For samples spun at high spin speed, the centripetal force pulled collagen solution flow toward the edge of the sample, which made few collagen molecules stay in the middle of the sample. Reducing the spin speed can keep collagen molecules in the middle, yet the coating may not cover the entire substrate because of poor centripetal force and the crystallization of solution that may occur [134]. The authors chose spin speed at 4250 rpm as the final coating speed, which offered the most uniform coating and high cellular response.

The electrochemical corrosion test showed a reduction in corrosion rates for both non-porous and porous collagen-coated samples comparing to samples without collagen coating (NP-C < NP-NC; 10P-NC < 10P-C) in Table 3.3. Collagen coating reduced the corrosion rate of Fe-30Mn because it prevented the direct exposure of alloy surface to the electrolyte, hence reducing oxidation. Nevertheless, there was no statistically significant difference in corrosion rates between the collagen-coated and non-coated groups, demonstrating that collagen coating only minimally hindered the overall corrosion rates of Fe-30Mn.

Collagen coating of the Fe-Mn alloys significantly reduced the cytotoxicity level of the porous Fe-30Mn groups (10P-C < 10P-NC), as shown in Table 3.4 and Figure 3.6. The coating served as an intermediate layer between cells and the substrate. It contained high level of amino acids including glycine, proline, and hydroxyproline [135] that provided binding sites to cell-surface receptors or integrins on the cell membrane, which greatly reduced the occurrence of anoikis or cell-detachment-apoptosis. Consequently, increasing number of binding sites facilitated cell attachment, metabolic activity and mobility which enabled cell-to-cell communication. This was demonstrated by the significant increase of the day 1 average cell size, which was proportional to the cell adhesion, from the non-coated groups (NP-NC, 10P-NC, and CT-NC) to the collagen-coated groups (NP-C, 10P-C, and CT-C), respectively (Figure 3.8b and Table 3.4). Furthermore, the average cell count values for the collagen-coated Fe-30Mn groups were significantly higher than those for the non-coated Fe-30Mn groups, indicating that the collagen coating improved the initial cellular viability on Fe-30Mn. The average cell size decreased from day 1 to day 3 for the collagen-coated Fe-30Mn groups because the cells nearly reached full confluency, squeezing themselves to cover the entire surface. On the other hand, the average cell size for the non-coated

Fe-30Mn groups at day 3 increased because the cells still had room to extend their dendrites to communicate to the other cells.

The porous Fe-30Mn groups (10P-NC and 10P-C) showed a higher toxicity level than the non-porous Fe30Mn groups (NP-NC and NP-C) because a higher concentration level of metal ions (i.e. $Fe^{2+/3+}$ and Mn^{2+}) leached into the environment which eventually lead to cell necrosis. Even the average cytotoxicity level for the 10P-NC group showed the highest among those for all groups, however, it was still within 30% of the average cytotoxicity level for the negative control Ti6Al4V group, and according to the standard ISO10993-5 [103], the 10P-NC group was not considered severe cytotoxic. Although the coated non-porous group (NP-C) showed higher cell viability and adhesion than the coated porous group (10P-C), the coated porous group was more desirable because it provided three-dimensional environment for cells to facilitate their phenotypes and cell-to-cell interactions, mimicking the physiological environment closer to tissues and organs [136,137]. Since there was no statistically significant difference between the 10P-C and 10P-NC group in the corrosion test, yet the 10P-C group showed a significant lower cytotoxicity level than the 10P-NC group in the cytotoxicity test, we can conclude that collagen coating is a valid route towards increasing the osteointegration for porous Fe-30Mn without hindering the alloy degradation rate.

3.5   Summary of Chapter 3

Fe-30Mn is a promising biodegradable material for transient orthopedic fixation devices, but further improvements in osteointegration of these materials are necessary. The spin coating technique was used to obtain homogeneous coating of fibrillar Type I collagen on the surface of Fe-Mn alloys with different porosity levels. According to the potentiodynamic polarization test,

there were no significant differences between the collagen-coated groups (NP-C and 10P-C) and the non-coated groups (NP-NC and 10P-NC) in terms of corrosion rates. However, after 1 day of incubation, the porous collagen-coated group (10P-C) showed a significantly lower level of cytotoxicity than the porous non-coated group (10P-NC). The quantitative results of the average corrosion rates and cytotoxicity levels, combined with the qualitative results of cell count values, sizes, and morphology obtained from the fluorescence microscopy and SEM images, showed that the collagen coating improved the initial cell adhesion and viability significantly without hindering the degradation behavior of porous Fe-30Mn.

CHAPTER 4.   FUTURE DIRECTIONS

Bioresorbable Fe-30Mn alloys have shown strong mechanical properties that are comparable to stainless steel. With the incorporation of porosity and surface coating of Type I collagen, these alloys showed enhanced corrosion rates and *in-vitro* biocompatibility, rendering them as promising materials for temporary orthopedic fixation devices.

In **Error! Reference source not found.** "**Error! Reference source not found.**," we investigated the Fe-30Mn samples containing 0% to 10% porosity, as well as samples containing 60% porosity to explore both the very low and the very high end of the porosity spectrum. The mechanical properties, corrosion behavior and cytotoxicity of Fe30Mn alloys with porosities in-between the 10-vol% and 60-vol% have not been studied. Although the Fe30Mn samples with 60% porosity showed the highest average corrosion rate among the studied samples, we found that they caused a cytotoxic effect to the cells that makes this group not biocompatible enough for use in bioresorbable implants. Both the 10% and 60% porosity samples showed compatible ultimate compressive strengths, stronger than a native natural cortical bone, while the former group displayed minimal cytotoxic effects. Thus, it is highly possible that the Fe-Mn alloy with ideal porosity in terms of both corrosion rate and low cytotoxicity, will be found in the porosity interval laying in between 10% and 60% porosity. Investigations in this porosity range is recommended to evaluate the tradeoff between the biocompatibility and corrosion behavior in Fe30Mn alloys.

In CHAPTER 3 "ENHANCING OSTEO-INTEGRATION of FE-30%MN ALLOYS COATED WITH TYPE I COLLAGEN," we evaluated the effectiveness of collagen coating onto cell viability, adhesion and alloy corrosion behavior. Results showed that coating Fe30Mn containing

10% porosity with Type I collagen significantly decreased their cytotoxic effect and significantly improved the cellular adhesion without significantly reducing the corrosion rate. Future studies for coated Fe30Mn should aim to achieve a homogeneous and consistent coating using different coating parameters and techniques. The mechanisms of the degradation process between the alloy and the coating, as well as the degradation process between the coating and the cells are aspects of high interest for future studies. Furthermore, a long term *in-vitro* study to study the osteogenic differentiation of stem cells, and an *in-vivo* study to evaluate the real-time corrosion behavior occurring in the body are proposed for further improvements of Fe30Mn alloys to be used in transient implants.

After a long incubation time, irregular corrosion derived particles including metal hydroxides such as $Fe(OH)_3$ and $Mn(OH)_2$, as well as phosphates such as $Mn_3(PO_4)_2$ and $FePO_4$, may occasionally break off from the surface to the surrounding media. These particles may cause a non-specific foreign body response, resulting in a series of chronic inflammation reactions and stimulating infection [138]. Therefore, quantitative and qualitative characterizations of the corrosion products break-off over time are also recommended.

Although iron, manganese, and ammonium bicarbonate powders were all well blended in a high-speed mixer, the powders were distributed unevenly upon filling the cavity of the die during the compaction. The porogen ammonium bicarbonate powders were found dominating the bottom of the die cavity, whereas the alloy powders were found dominating the top of the cavity. Different powder flowing rates of the powders due to powder properties (i.e. powder size and shape) upon filling resulted in the graded distribution of ammonium bicarbonate powders along the direction

of the compacting force. Consequently, graded porosity in the alloy was observed after sintering. The observed graded porosity in the alloy provided no major problems for the studies shown in **Error! Reference source not found.** and CHAPTER 3 because: (1) the purpose of the studies was to improve the degradation rate and biocompatibility of the Fe30Mn alloy through incorporating the porosity and coating of Type I collagen, and (2) the fabricated samples were compacted to the shape of the tablet form where the graded porosity had little influence to the corrosion rate and biocompatibility of the alloy. Nevertheless, characterization of the powder production, powder properties, as well as powder friction and flow, etc., are suggested in the future.

CHAPTER 5.   CONCLUSIONS

The idea of bioresorbable metals has drawn increasing attention in the fields of orthopedic, cardiovascular, and pediatrics. Researchers and scientists have already found that, with the addition of manganese as the alloying element, the Fe-30Mn alloy showed great mechanical properties comparable to the stainless steel 316L, as well as an improved corrosion rate and high relative metabolic activity comparing to pure iron. Powder metallurgy is the most common method to prepare the Fe-30Mn alloy due to its flexibility, reliability, and low price, without further machining. By using the space holder technique in the powder metallurgy, porous Fe-30Mn alloys with various porosity can be obtained. The porous structure of Fe-30Mn alloys is helpful to increase the corrosion rate, and it is necessary for the cell microenvironment for nutrients transport, extracellular matrix formation, and angiogenesis. However, the biggest challenge is to design a porous Fe-30Mn scaffold that shows a desirable corrosion rate at the same time with great biocompatibility and osteointegration. The porous Fe-30Mn alloy must show good biocompatibility so that the alloy does not cause any severe cytotoxic effect, and the alloy should also show good osteointegration to improve the cell-alloy interactions including stem cell adhesion, proliferation, and differentiation.

The mechanical properties, corrosion behavior, and cytotoxicity limit of the Fe-30Mn alloys with 0-, 5-, 10-, and 60-volume percent porosity were studied in CHAPTER 2. The Fe-30Mn alloys mixed with 60-vol% ammonium bicarbonate showed good mechanical properties comparable to the natural cortical bone and they displayed the highest average value of corrosion rate in the potentiodynamic polarization test among the four groups. Nevertheless, the high concentration of metal ions, particularly Mn^{2+}, released into the surrounding media caused a negative cytotoxic

effect in both the indirect and direct cytotoxicity studies. The Fe-30Mn alloys containing 10-vol% porosity showed minimal cytotoxicity effect, demonstrating their good biocompatibility, while exhibiting the average corrosion rate 2-fold higher than the non-porous group. Even the porous Fe-30Mn alloys with 10-vol% porosity showed suitable biocompatibility, the inherent material properties of the Fe-30%Mn alloys provided limited osteointegration that requires further improvement for the applications of transient orthopedic fixation devices.

The focus in CHAPTER 3 was to improve the osteo-integration of the Fe-30Mn alloys by coating the alloy surface with Type I collagen. The potentiodynamic polarization and direct cytotoxicity test were conducted onto four experimental Fe-30Mn groups that contained either 0- or 10-vol% porosity with a combination of with or without collagen coating. The porous collagen-coated Fe-30Mn group showed statistically significant decrease in the cytotoxicity level yet exhibited no statistically significant difference in the corrosion rate when it compared to the porous non-coated Fe-30Mn group. Furthermore, only cells seeded on the collagen-coated groups displayed focal adhesion plaques which played a crucial role in cell adhesion, spreading, migration, proliferation, differentiation, and apoptosis through different chemical signal pathways. The study proved that coating of collagen greatly enhanced the osteo-integration of the Fe30Mn alloys without inhibiting the degradation rate of the alloys.

With the incorporation of porosity and surface coating of Type I collagen, the bioresorbable Fe-30Mn alloy has shown enhanced degradability, biocompatibility, and osteo-integration which is considered as a promising bone biomaterial for fixation medical devices. However, further investigations in alloy processing and porosity control to obtain consistent mechanical properties,

as well as finding the tradeoff between the biocompatibility and corrosion behaviors for the Fe-30Mn alloys containing porosities between 10-vol% and 60-vol% are recommended. In addition, the uniformity and stability of the Type I collagen surface coating will need to be improved to achieve a high level of osteo-integration for the Fe-30Mn alloy. Further developments in long-term in vitro studies and in vivo studies are also encouraged.

REFERENCES

[1]   W.A. Lane, Clinical remarks on the operative treatment of simple fractures, Br. Med. J. (1905). doi:10.1136/bmj.2.2342.1325.

[2]   A.C. Hänzi, I. Gerber, M. Schinhammer, J.F. Löffler, P.J. Uggowitzer, On the in vitro and in vivo degradation performance and biological response of new biodegradable Mg-Y-Zn alloys, Acta Biomater. (2010). doi:10.1016/j.actbio.2009.10.008.

[3]   B. Liu, Y.F. Zheng, Effects of alloying elements (Mn, Co, Al, W, Sn, B, C and S) on biodegradability and in vitro biocompatibility of pure iron, Acta Biomater. 7 (2011) 1407–1420. doi:10.1016/j.actbio.2010.11.001.

[4]   M. Moravej, F. Prima, M. Fiset, D. Mantovani, Electroformed iron as new biomaterial for degradable stents: Development process and structure-properties relationship, Acta Biomater. 6 (2010) 1726–1735. doi:10.1016/j.actbio.2010.01.010.

[5]   F.L. Nie, Y.F. Zheng, S.C. Wei, C. Hu, G. Yang, In vitro corrosion, cytotoxicity and hemocompatibility of bulk nanocrystalline pure iron, Biomed. Mater. 5 (2010) 065015. doi:10.1088/1748-6041/5/6/065015.

[6]   E. Zhang, H. Chen, F. Shen, Biocorrosion properties and blood and cell compatibility of pure iron as a biodegradable biomaterial, J. Mater. Sci. Mater. Med. 21 (2010) 2151–2163. doi:10.1007/s10856-010-4070-0.

[7]   S. Zhu, N. Huang, L. Xu, Y. Zhang, H. Liu, H. Sun, Y. Leng, Biocompatibility of pure iron: In vitro assessment of degradation kinetics and cytotoxicity on endothelial cells, Mater. Sci. Eng. C. 29 (2009) 1589–1592. doi:10.1016/j.msec.2008.12.019.

[8]   H. Hermawan, D. Ramdan, J.R.P. Djuansjah, Metals for biomedical applications, in: Biomed. Eng. - From Theory to Appl., 2011. doi:10.5772/19033.

[9]   H. Uhthoff, D. Bardos, M. Liskova-Kiar, The advantages of titanium alloy over stainless steel plates for the internal fixation of fractures. An experimental study in dogs, J. Bone Jt. Surg. 63-B (1981) 427–484. doi:10.1302/0301-620X.63B3.7263759.

[10]   H. Shimizu, S. Inoue, H. Miyauchi, K. Watanabe, Y. Takahashi, Mould filling of Ag-Pd-Cu-Au and Ag-Zn-Sn-In alloy castings made using a rapidly prepared gypsum-bonded investment material., Eur. J. Prosthodont. Restor. Dent. 16 (2008) 177–80.

[11]   Centers for Disease Control and Prevention, National ambulatory medical care survey (NAMCS) factsheet for orthopedic surgery, 2010. www.cdc.gov/namcs (accessed March 5, 2019).

[12]   M. Heiden, E. Walker, E. Nauman, L. Stanciu, Evolution of novel bioresorbable iron-manganese implant surfaces and their degradation behaviors in vitro, J. Biomed. Mater. Res. Part A. 103 (2015) 185–193. doi:10.1002/jbm.a.35155.

[13]   E.D. McBride, Absorbable metal in bone surgery, J. Am. Med. Assoc. 111 (1938) 2464. doi:10.1001/jama.1938.02790530018007.

[14]   M. Peuster, P. Wohlsein, M. Brügmann, M. Ehlerding, K. Seidler, C. Fink, H. Brauer, a Fischer, G. Hausdorf, A novel approach to temporary stenting: degradable cardiovascular stents produced from corrodible metal-results 6-18 months after implantation into New Zealand white rabbits., Heart. 86 (2001) 563–569. doi:10.1136/heart.86.5.563.

[15]   M. Peuster, C. Hesse, T. Schloo, C. Fink, P. Beerbaum, C. von Schnakenburg, Long-term biocompatibility of a corrodible peripheral iron stent in the porcine descending aorta, Biomaterials. 27 (2006) 4955–4962. doi:10.1016/j.biomaterials.2006.05.029.

[16]   J.E. Schaffer, E.A. Nauman, L.A. Stanciu, Cold-Drawn Bioabsorbable Ferrous and Ferrous Composite Wires: An Evaluation of Mechanical Strength and Fatigue Durability, Metall. Mater. Trans. B. 43 (2012) 984–994. doi:10.1007/s11663-012-9661-3.

[17]   C.P. McCord, J.J. Prendergast, S.F. Meek, G.C. Harrold, Chemical gas gangrene from metallic magnesium, Ind. Med. 11 (1942) 71–75.

[18]   Institute of Medicine, Dietary reference intakes: vitamin A, vitamin K, arsenic, boron, chromium, copper, iodine, iron, manganese, molybdenum, nickel, silicon, vanadium, and zinc., J. Am. Diet. Assoc. 101 (2001) 294–301. doi:10.1016/S0002-8223(01)00078-5.

[19]   H. Hermawan, H. Alamdari, D. Mantovani, D. Dubé, Iron–manganese: new class of metallic degradable biomaterials prepared by powder metallurgy, Powder Metall. 51 (2008) 38–45. doi:10.1179/174329008X284868.

[20]   H. Mueller, J. Loeffler, P. Uggowitzer, Implant with a base body of a biocorrodible iron alloy, US Pat. (2009).

[21]   S. Cotes, M. Sade, A. Guillermet, Fcc/Hcp martensitic transformation in the Fe-Mn system: Experimental study and thermodynamic analysis of phase stability, Metall. Mater. Trans. A. 26 (1995) 1957–1969. doi:10.1007/BF02670667.

[22]   S.M. Cotes, A.F. Guillermet, M. Sade, Fcc/Hcp martensitic transformation in the Fe-Mn system: Part II. Driving force and thermodynamics of the nucleation process, Metall. Mater. Trans. A. 35 (2004) 83–91. doi:10.1007/s11661-004-0111-y.

[23]   J. Martínez, S.M. Cotes, A.F. Cabrera, J. Desimoni, A. Fernández Guillermet, On the relative fraction of ε martensite in γ-Fe-Mn alloys, Mater. Sci. Eng. A. 408 (2005) 26–32. doi:10.1016/j.msea.2005.06.019.

[24]   H. Hermawan, D. Dubé, D. Mantovani, Degradable metallic biomaterials: Design and development of Fe-Mn alloys for stents, J. Biomed. Mater. Res. - Part A. 93 (2010) 1–11. doi:10.1002/jbm.a.32224.

[25]   F. Trichter, A. Rabinkin, M. Ron, A. Sharfstein, A study of γ → ε phase transformation in Fe-Mn alloys induced by high pressure and plastic deformation, Scr. Metall. 12 (1978) 431–434. doi:10.1016/0036-9748(78)90251-X.

[26]   A. Rabinkin, On magnetic contributions to γ → ε phase transformations in Fe-Mn alloys, Calphad. 3 (1979) 77–84. doi:10.1016/0364-5916(79)90008-7.

[27]   J.-L. Strudel, Mechanical Properties of Multiphase Alloys, Phys. Metall. (1996) 2105–2206. doi:10.1016/B978-044489875-3/50030-2.

[28]   R.F. Allen, N.C. Baldini, P.E. Donofrio, others, {Standard Specification for Wrought 18 Chromium-14 Nickle-2.5 Molybdenum Stainless Steel Bar and Wire for Surgical Implants (F138)}, {Annual B. ASTM Stand. Med. Devices Serv. (1998) 21–23.

[29]   A. F136-02a, Standard Specification for Wrought Titanium-6 Aluminum-4 Vanadium ELI (Extra Low Interstitial) Alloy for Surgical Implant Applications (UNS R56401), (2002).

[30]   W.F. Gale, T.C. Totemeier, Equilibrium diagrams, in: Smithells Met. Ref. B., Butterworth-Heinemann, 2004: pp. 11–1. doi:10.1016/B978-075067509-3/50014-2.

[31]   M. Heiden, A. Kustas, K. Chaput, E. Nauman, D. Johnson, L. Stanciu, Effect of microstructure and strain on the degradation behavior of novel bioresorbable iron-manganese alloy implants, J. Biomed. Mater. Res. - Part A. 103 (2015) 738–745. doi:10.1002/jbm.a.35220.

[32]   Q. Zhang, P. Cao, Degradable porous Fe-35wt.%Mn produced via powder sintering from NH_4HCO_3 porogen, Mater. Chem. Phys. 163 (2015) 394–401. doi:10.1016/j.matchemphys.2015.07.056.

[33] D.T. Chou, D. Wells, D. Hong, B. Lee, H. Kuhn, P.N. Kumta, Novel processing of iron-manganese alloy-based biomaterials by inkjet 3-D printing, Acta Biomater. 9 (2013) 8593–8603. doi:10.1016/j.actbio.2013.04.016.

[34] I. (Isaac T.H. Chang, Y. Zhao, Advances in powder metallurgy : properties, processing and applications, n.d. https://www.sciencedirect.com/book/9780857094209/advances-in-powder-metallurgy (accessed May 17, 2019).

[35] A. Schömig, A. Kastrati, H. Mudra, R. Blasini, H. Schühlen, V. Klauss, G. Richardt, F.J. Neumann, Four-year experience with Palmaz-Schatz stenting in coronary angioplasty complicated by dissection with threatened or present vessel closure., Circulation. 90 (1994) 2716–24. http://www.ncbi.nlm.nih.gov/pubmed/7994813 (accessed May 17, 2019).

[36] Y.F. Zheng, X.N. Gu, F. Witte, Biodegradable metals, Mater. Sci. Eng. R Reports. 77 (2014) 1–34. doi:10.1016/j.mser.2014.01.001.

[37] H. Hermawan, A. Purnama, D. Dube, J. Couet, D. Mantovani, Fe-Mn alloys for metallic biodegradable stents: Degradation and cell viability studies, Acta Biomater. 6 (2010) 1852–1860. doi:10.1016/j.actbio.2009.11.025.

[38] A. G59-97, {Standard Test Method for Conducting Potentiodynamic Polarization Resistance Measurements}, (2009).

[39] A. G31-72, {Standard Practice for Laboratory Immersion Corrosion Testing of Metals}, (2004).

[40] D.A. Dickerson, T.N. Misk, D.C. Van Sickle, G.J. Breur, E.A. Nauman, In vitro and in vivo evaluation of orthopedic interface repair using a tissue scaffold with a continuous hard tissue-soft tissue transition., J. Orthop. Surg. Res. 8 (2013) 18. doi:10.1186/1749-799X-8-18.

[41] D.D. Williams, Definitions in biomaterials : proceedings of a consensus conference of the European Society for Biomaterials, Chester, England, March 3-5, 1986, (1987).

[42] J.M. Anderson, A. Rodriguez, D.T. Chang, Foreign body reaction to biomaterials, Semin. Immunol. 20 (2008) 86–100. doi:10.1016/j.smim.2007.11.004.

[43] L. Vroman, A.L. Adams, Adsorption of proteins out of plasma and solutions in narrow spaces, J. Colloid Interface Sci. 111 (1986) 391–402. doi:10.1016/0021-9797(86)90042-1.

[44] M. Kalbacova, S. Roessler, U. Hempel, R. Tsaryk, K. Peters, D. Scharnweber, J.C. Kirkpatrick, P. Dieter, The effect of electrochemically simulated titanium cathodic corrosion products on ROS production and metabolic activity of osteoblasts and monocytes/macrophages, Biomaterials. 28 (2007) 3263–3272. doi:10.1016/J.BIOMATERIALS.2007.02.026.

[45] C.T. Hanks, J.C. Wataha, Z. Sun, In vitro models of biocompatibility: A review, Dent. Mater. 12 (1996) 186–193. doi:10.1016/S0109-5641(96)80020-0.

[46] D.F. Williams, On the mechanisms of biocompatibility, Biomaterials. 29 (2008) 2941–2953. doi:10.1016/j.biomaterials.2008.04.023.

[47] B. Sommer, R. Felix, C. Sprecher, M. Leunig, R. Ganz, W. Hofstetter, Wear particles and surface topographies are modulators of osteoclastogenesis in vitro, J. Biomed. Mater. Res. - Part A. 72 (2005) 67–76. doi:10.1002/jbm.a.30202.

[48] T. Hirayama, Y. Fujikawa, I. Itonaga, T. Torisu, Effect of particle size on macrophage-osteoclast differentiation in vitro, J. Orthop. Sci. 6 (2001) 53–58. doi:10.1007/S007760170025.

[49] P.F. Doorn, P.A. Campbell, J. Worrall, P.D. Benya, H.A. McKellop, H.C. Amstutz, Metal wear particle characterization from metal on metal total hip replacements: transmission electron microscopy study of periprosthetic tissues and isolated particles., J. Biomed. Mater. Res. 42 (1998) 103–11. http://www.ncbi.nlm.nih.gov/pubmed/9740012 (accessed May 17, 2019).

[50] S.D. Neale, D.R. Haynes, D.W. Howie, D.W. Murray, N.A. Athanasou, The effect of particle phagocytosis and metallic wear particles on osteoclast formation and bone resorption in vitro., J. Arthroplasty. 15 (2000) 654–62. doi:10.1054/arth.2000.6622.

[51] A. Yamamoto, R. Honma, M. Sumita, Cytotoxicity evaluation of 43 metal salts using murine fibroblasts and osteoblastic cells, J. Biomed. Mater. Res. 39 (1998) 331–340. doi:10.1002/(SICI)1097-4636(199802)39:2<331::AID-JBM22>3.0.CO;2-E.

[52] Q. Chen, G.A. Thouas, Metallic implant biomaterials, Mater. Sci. Eng. R Reports. 87 (2015) 1–57. doi:10.1016/J.MSER.2014.10.001.

[53] J.A. Roth, M.D. Garrick, Iron interactions and other biological reactions mediating the physiological and toxic actions of manganese, Biochem. Pharmacol. 66 (2003) 1–13. doi:10.1016/S0006-2952(03)00145-X.

[54]   M.H. Selim, R.R. Ratan, The role of iron neurotoxicity in ischemic stroke, Ageing Res. Rev. 3 (2004) 345–353. doi:10.1016/j.arr.2004.04.001.

[55]   D. Mergler, M. Baldwin, Early Manifestations of Manganese Neurotoxicity in Humans: An Update, Environ. Res. 73 (1997) 92–100. doi:10.1006/enrs.1997.3710.

[56]   N.J. Hallab, C. Vermes, C. Messina, K.A. Roebuck, T.T. Glant, J.J. Jacobs, Concentration-and composition-dependent effects of metal ions on human MG-63 osteoblasts., J. Biomed. Mater. Res. 60 (2002) 420–33. http://www.ncbi.nlm.nih.gov/pubmed/11920666 (accessed May 17, 2019).

[57]   D.R. Intakes, Dietary Reference Intakes (DRIs): Recommended Dietary Allowances and Adequate Intakes , Vitamins Food and Nutrition Board , Institute of Medicine , National Academies, Food Nutr. Board. (2011) 10–12. doi:10.1111/j.1753-4887.2004.tb00011.x.

[58]   J.Y. Wang, B.H. Wicklund, R.B. Gustilo, D.T. Tsukayama, Titanium, chromium and cobalt ions modulate the release of bone-associated cytokines by human monocytes/macrophages in vitro., Biomaterials. 17 (1996) 2233–40. http://www.ncbi.nlm.nih.gov/pubmed/8968517 (accessed May 17, 2019).

[59]   O. Kudo, Y. Fujikawa, I. Itonaga, A. Sabokbar, T. Torisu, N.A. Athanasou, Proinflammatory cytokine (TNFα/IL-1α) induction of human osteoclast formation, J. Pathol. 198 (2002) 220–227. doi:10.1002/path.1190.

[60]   M. Heiden, E. Walker, E. Nauman, L. Stanciu, Evolution of novel bioresorbable iron-manganese implant surfaces and their degradation behaviors in vitro, J. Biomed. Mater. Res. - Part A. 103 (2015) 185–193. doi:10.1002/jbm.a.35155.

[61]   A.C. Hänzi, I. Gerber, M. Schinhammer, J.F. Löffler, P.J. Uggowitzer, On the in vitro and in vivo degradation performance and biological response of new biodegradable Mg-Y-Zn alloys, Acta Biomater. 6 (2010) 1824–1833. doi:10.1016/j.actbio.2009.10.008.

[62]   M. Schinhammer, P. Steiger, F. Moszner, J.F. Löffler, P.J. Uggowitzer, Degradation performance of biodegradable FeMnC(Pd) alloys, Mater. Sci. Eng. C. 33 (2013) 1882–1893. doi:10.1016/j.msec.2012.10.013.

[63]   M. Schinhammer, A.C. Hänzi, J.F. Löffler, P.J. Uggowitzer, Design strategy for biodegradable Fe-based alloys for medical applications, Acta Biomater. 6 (2010) 1705–1713. doi:10.1016/j.actbio.2009.07.039.

[64] Z. Xu, M.A. Hodgson, P. Cao, A comparative study of powder metallurgical (PM) and wrought Fe-Mn-Si alloys, Mater. Sci. Eng. A. 630 (2015) 116–124. doi:10.1016/j.msea.2015.02.021.

[65] H. Li, Y. Wang, Q. Peng, High degradation rate of Fe-20Mn-based bio-alloys by accumulative cryo-rolling and annealing, Mater. Sci. Eng. C. 79 (2017) 37–44. doi:10.1016/j.msec.2017.05.004.

[66] M. Heiden, A. Kustas, K. Chaput, E. Nauman, D. Johnson, L. Stanciu, Effect of microstructure and strain on the degradation behavior of novel bioresorbable iron-manganese alloy implants, J. Biomed. Mater. Res. PART A. 103 (2015) 738–745. doi:10.1002/jbm.a.35220.

[67] M.M.C.G. Silva, L.A. Cyster, J.J.A. Barry, X.B. Yang, R.O.C. Oreffo, D.M. Grant, C.A. Scotchford, S.M. Howdle, K.M. Shakesheff, F.R.A.J. Rose, The effect of anisotropic architecture on cell and tissue infiltration into tissue engineering scaffolds, Biomaterials. 27 (2006) 5909–5917. doi:10.1016/j.biomaterials.2006.08.010.

[68] H.I. Bakan, A novel water leaching and sintering process for manufacturing highly porous stainless steel, Scr. Mater. 55 (2006) 203–206. doi:10.1016/j.scriptamat.2006.03.039.

[69] S. Muñoz, J. Pavón, J.A. Rodríguez-Ortiz, A. Civantos, J.P. Allain, Y. Torres, On the influence of space holder in the development of porous titanium implants: Mechanical, computational and biological evaluation, Mater. Charact. (2015). doi:10.1016/j.matchar.2015.08.019.

[70] Y. Torres, J.J. Pavón, I. Nieto, J.A. Rodríguez, Conventional powder metallurgy process and characterization of porous titanium for biomedical applications, Metall. Mater. Trans. B Process Metall. Mater. Process. Sci. 42 (2011) 891–900. doi:10.1007/s11663-011-9521-6.

[71] J. Čapek, D. Vojtěch, Effect of sintering conditions on the microstructural and mechanical characteristics of porous magnesium materials prepared by powder metallurgy, Mater. Sci. Eng. C. 35 (2014) 21–28. doi:10.1016/j.msec.2013.10.014.

[72] H. Zhuang, Y. Han, A. Feng, Preparation, mechanical properties and in vitro biodegradation of porous magnesium scaffolds, Mater. Sci. Eng. C. 28 (2008) 1462–1466. doi:10.1016/j.msec.2008.04.001.

[73] H. Bafti, A. Habibolahzadeh, Production of aluminum foam by spherical carbamide space holder technique-processing parameters, Mater. Des. 31 (2010) 4122–4129. doi:10.1016/j.matdes.2010.04.038.

[74] J. Čapek, D. Vojtěch, Microstructural and mechanical characteristics of porous iron prepared by powder metallurgy, Mater. Sci. Eng. C. 43 (2014) 494–501. doi:10.1016/j.msec.2014.06.046.

[75] a. Laptev, O. Vyal, M. Bram, H.P. Buchkremer, D. Stöver, Green strength of powder compacts provided for production of highly porous titanium parts, Powder Metall. 48 (2005) 358–364. doi:10.1179/174329005X73838.

[76] F. Application, P. Data, IMPLANT WITH A BASE BODY OF A A : lxo w loco, 2 (2013).

[77] A. Rabinkin, On magnetic contributions to ??????? phase transformations in Fe-Mn alloys, Calphad. 3 (1979) 77–84. doi:10.1016/0364-5916(79)90008-7.

[78] ASTM International, Density of Compacted or Sintered Powder Metallurgy (PM) Products Using Archimedes' Principle, ASTM B962-17. i (2017) 1–7. doi:10.1520/B0962-13.2.

[79] M. Hrubovčáková, M. Kupková, M. Džupon, Fe and Fe-P Foam for Biodegradable Bone Replacement Material: Morphology, Corrosion Behaviour, and Mechanical Properties, Adv. Mater. Sci. Eng. 2016 (2016). doi:10.1155/2016/6257368.

[80] J.T.Y. Lee, Y. Leng, K.L. Chow, F. Ren, X. Ge, K. Wang, X. Lu, Cell culture medium as an alternative to conventional simulated body fluid, Acta Biomater. 7 (2011) 2615–2622. doi:10.1016/j.actbio.2011.02.034.

[81] C.A. Schneider, W.S. Rasband, K.W. Eliceiri, NIH Image to ImageJ: 25 years of image analysis, Nat. Methods. 9 (2012) 671. https://doi.org/10.1038/nmeth.2089.

[82] C. Zhang, H. Li, M.Q. Li, Interaction mechanism between void and interface grain boundary in diffusion bonding, Sci. Technol. Weld. Join. 20 (2014) 123–129. doi:10.1179/1362171814Y.0000000242.

[83] M. Dewidar, H.F. Mohamed, J.-K. Lim, A new approach for manufacturing a high porosity Ti-6Al-4V scaffolds for biomedical applications, J. Mater. Sci. Tenchonology. 24 (2008) 931–935. http://d.wanfangdata.com.cn/periodical_clkxjsxb-e200806021.aspx.

[84]   A. Laptev, M. Bram, H.P. Buchkremer, D. Stöver, A. Laptev, M. Bram, H.P. Buchkremer, D. Sto, Study of production route for titanium parts combining very high porosity and complex shape Study of production route for titanium parts combining very high porosity and complex shape, 5899 (2017). doi:10.1179/003258904225015536.

[85]   S. Won, H. Jung, M. Kang, H. Kim, Y. Koh, Y. Estrin, Fabrication of porous titanium scaffold with controlled porous structure and net-shape using magnesium as spacer, Mater. Sci. Eng. C. 33 (2013) 2808–2815. doi:10.1016/j.msec.2013.03.011.

[86]   Y. Torres, J.J. Pavón, J.A. Rodríguez, Processing and characterization of porous titanium for implants by using NaCl as space holder, J. Mater. Process. Technol. 212 (2012) 1061–1069. doi:10.1016/j.jmatprotec.2011.12.015.

[87]   V.T. Witusiewicz, F. Sommer, E.J. Mittemeijer, Reevaluation of the Fe-Mn phase diagram, J. Phase Equilibria Diffus. 25 (2004) 346–354. doi:10.1007/s11669-004-0152-3.

[88]   P. Marinelli, A. Baru, A.F. Guillermet, M. Sadel, Lattice parameters of metastable structures in quenched Fe-Mn alloys . Part II : hcp phase Lattice Parameters of Metastable Structures in Quenched Fe - Mn Alloys . Part II : hcp Phase, (2016).

[89]   A. Trichter, F., Rabinkin, A., Ron, A., Sharfstin, A study of phase transformation in Fe-Mn Alloys Induced by High Pressure and Plastic Deformation, Scr. Metall. 12 (1978) 431–434.

[90]   P. Sahu, A.S. Hamada, R.N. Ghosh, L.P. Karjalainen, M. Society, X-ray Diffraction Study on Cooling-Rate-Induced c fcc fi e hcp Martensitic Transformation in Cast-Homogenized, 38 (2007). doi:10.1007/s11661-007-9240-4.

[91]   S. Pal, Mechanical Properties of Biological Materials, in: Des. Artif. Hum. Joints Organs, Springer US, Boston, MA, 2014: pp. 23–40. doi:10.1007/978-1-4614-6255-2_2.

[92]   M. Sharma, G.K. Gupta, O.P. Modi, B.K. Prasad, PM processed titanium foam: influence of morphology and content of space holder on microstructure and mechanical properties, Powder Metall. 56 (2013) 55–60. doi:10.1179/1743290112Y.0000000036.

[93]   A. Hattiangadi, A. Bandyopadhyay, Strength Degradation of Nonrandom Porous Ceramic Structures under Uniaxial Compressive Loading, J. Am. Ceram. Soc. 83 (2000) 2730–2736. doi:10.1111/j.1151-2916.2000.tb01624.x.

[94]   M.M. Shbeh, R. Goodall, Open pore titanium foams via metal injection molding of metal powder with a space holder, Met. Powder Rep. 71 (2016) 450–455. doi:10.1016/j.mprp.2016.06.003.

[95] N. Bekoz, E. Oktay, Effects of carbamide shape and content on processing and properties of steel foams, J. Mater. Process. Technol. 212 (2012) 2109–2116. doi:10.1016/j.jmatprotec.2012.05.015.

[96] Y. Bai, G. Wagner, C.B. Williams, Effect of Particle Size Distribution on Powder Packing and Sintering in Binder Jetting Additive Manufacturing of Metals, J. Manuf. Sci. Eng. 139 (2017) 081019. doi:10.1115/1.4036640.

[97] M.E. Dizlek, M. Guden, U. Turkan, A. Tasdemirci, Processing and compression testing of Ti6Al4V foams for biomedical applications, J. Mater. Sci. 44 (2009) 1512–1519. doi:10.1007/s10853-008-3038-7.

[98] B. Liu, Y.F. Zheng, L. Ruan, In vitro investigation of Fe30Mn6Si shape memory alloy as potential biodegradable metallic material, Mater. Lett. 65 (2011) 540–543. doi:10.1016/j.matlet.2010.10.068.

[99] M. Dehestani, K. Trumble, H. Wang, H. Wang, L.A. Stanciu, Effects of microstructure and heat treatment on mechanical properties and corrosion behavior of powder metallurgy derived Fe–30Mn alloy, Mater. Sci. Eng. A. 703 (2017) 214–226. doi:10.1016/j.msea.2017.07.054.

[100] T. Kokubo, H. Takadama, How useful is SBF in predicting in vivo bone bioactivity?, Biomaterials. 27 (2006) 2907–2915. doi:10.1016/j.biomaterials.2006.01.017.

[101] J. Čapek, J. Kubásek, D. Vojtěch, E. Jablonská, J. Lipov, T. Ruml, Microstructural, mechanical, corrosion and cytotoxicity characterization of the hot forged FeMn30(wt.%) alloy, Mater. Sci. Eng. C. 58 (2016) 900–908. doi:10.1016/j.msec.2015.09.049.

[102] S. Martin, Precipitation and Dissolution of Iron and Manganese Oxides, in: Environ. Catal., CRC Press, 2005: pp. 61–82. doi:doi:10.1201/9781420027679.ch3.

[103] International Standard ISO 10993-5 Biological evaluation of medical devices - Part 5: Tests for cytotoxicity: in vitro methods, Int. Stand. ISO. 3 Ed (2009) 42.

[104] M.H. Selim, R.R. Ratan, The role of iron neurotoxicity in ischemic stroke, Ageing Res. Rev. 3 (2004) 345–353. doi:10.1016/j.arr.2004.04.001.

[105] Otten, Jennifer J., Hellwig, Jennifer Pitzi, and Meyers, Linda, eds. Dietary Reference Intakes : The Essential Guide to Nutrient Requirements. Washington, DC, USA: National Academies Press, 2006. ProQuest ebrary. Web. 11 October 2015. Copyright © 2006. Na, (2015).

[106] R. Lucchini, Manganese, in: G.F. Nordberg, B.A. Fowler, M. Nordberg, L.T. Friberg (Eds.), Handb. Toxicol. Met. (Third Ed., Elsevier B.V., 2007: pp. 645–674. doi:10.1016/B978-0-12-369413-3.50087-2.

[107] M. Niinomi, M. Nakai, J. Hieda, Development of new metallic alloys for biomedical applications, Acta Biomater. 8 (2012) 3888–3903. doi:10.1016/j.actbio.2012.06.037.

[108] X. Li, X. Liu, S. Wu, K.W.K. Yeung, Y. Zheng, P.K. Chu, Design of magnesium alloys with controllable degradation for biomedical implants: From bulk to surface, Acta Biomater. 45 (2016) 2–30. doi:10.1016/J.ACTBIO.2016.09.005.

[109] H. Hermawan, D. Dubé, D. Mantovani, Developments in metallic biodegradable stents, Acta Biomater. 6 (2010) 1693–1697. doi:10.1016/J.ACTBIO.2009.10.006.

[110] C. Gao, S. Peng, P. Feng, C. Shuai, Bone biomaterials and interactions with stem cells, Nat. Publ. Gr. 5 (2017). doi:10.1038/boneres.2017.59.

[111] R. Gorejová, L. Haverová, R. Oriňaková, A. Oriňak, M. Oriňak, Recent advancements in Fe-based biodegradable materials for bone repair, J. Mater. Sci. 54 (2019) 1913–1947. doi:10.1007/s10853-018-3011-z.

[112] Y. Jones-Hall, G. Breur, L. Stanciu, M. Heiden, E. Nauman, M. Traverson, In Vivo Evaluation of Biodegradability and Biocompatibility of Fe30Mn Alloy, Vet. Comp. Orthop. Traumatol. 31 (2018) 010–016. doi:10.3415/vcot-17-06-0080.

[113] M.P. Staiger, A.M. Pietak, J. Huadmai, G. Dias, Magnesium and its alloys as orthopedic biomaterials : A review, Biomaterials. 27 (2006) 1728–1734. doi:10.1016/j.biomaterials.2005.10.003.

[114] F. Witte, V. Kaese, H. Haferkamp, E. Switzer, A. Meyer-Lindenberg, C.J. Wirth, H. Windhagen, In vivo corrosion of four magnesium alloys and the associated bone response, Biomaterials. 26 (2005) 3557–3563. doi:10.1016/j.biomaterials.2004.09.049.

[115] J. He, F. He, D. Li, Y. Liu, Y. Liu, Y. Ye, D. Yin, Advances in Fe-based biodegradable metallic materials, RSC Adv. 6 (2016) 112819–112838. doi:10.1039/c6ra20594a.

[116] E. Mouzou, C. Paternoster, R. Tolouei, A. Purnama, P. Chevallier, D. Dubé, F. Prima, D. Mantovani, In vitro degradation behavior of Fe − 20Mn − 1 . 2C alloy in three different pseudo-physiological solutions, Mater. Sci. Eng. C. 61 (2016) 564–573. doi:10.1016/j.msec.2015.12.092.

[117] J. Hufenbach, H. Wendrock, F. Kochta, U. Kühn, A. Gebert, Novel biodegradable Fe-Mn-C-S alloy with superior mechanical and corrosion properties, Mater. Lett. 186 (2017) 330–333. doi:10.1016/j.matlet.2016.10.037.

[118] N. Mohd, N. Boon, A. Hakim, F. Adibah, A. Majid, H. Hermawan, Degradation and in vitro cell-material interaction studies on hydroxyapatite-coated biodegradable porous iron for hard tissue scaffolds, J. Orthop. Transl. 2 (2014) 177–184. doi:10.1016/j.jot.2014.07.001.

[119] M. Heiden, E. Nauman, L. Stanciu, Bioresorbable Fe – Mn and Fe – Mn – HA Materials for Orthopedic Implantation : Enhancing Degradation through Porosity Control, Adv. Healthc. Mater. 6 (2017) 1700120. doi:10.1002/adhm.201700120.

[120] S.M. Huang, E.A. Nauman, L.A. Stanciu, Investigation of porosity on mechanical properties, degradation and in-vitro cytotoxicity limit of Fe30Mn using space holder technique, Mater. Sci. Eng. C. 99 (2019) 1048–1057. doi:10.1016/J.MSEC.2019.02.055.

[121] L.N. Luong, J. Ramaswamy, D.H. Kohn, Effects of osteogenic growth factors on bone marrow stromal cell differentiation in a mineral-based delivery system, Biomaterials. 33 (2012) 283–294. doi:10.1016/j.biomaterials.2011.09.052.

[122] H.S. Alghamdi, R. Bosco, J.J.J.P. Van Den Beucken, X.F. Walboomers, J.A. Jansen, Osteogenicity of titanium implants coated with calcium phosphate or collagen type-I in osteoporotic rats, Biomaterials. 34 (2013) 3747–3757. doi:10.1016/j.biomaterials.2013.02.033.

[123] Y. Förster, R. Bernhardt, V. Hintze, S. Möller, M. Schnabelrauch, D. Scharnweber, S. Rammelt, Collagen / glycosaminoglycan coatings enhance new bone formation in a critical size bone defect — A pilot study in rats, Mater. Sci. Eng. C. 71 (2017) 84–92. doi:10.1016/j.msec.2016.09.071.

[124] Y. Zhukova, C. Hiepen, P. Knaus, M. Osterland, S. Prohaska, J.W.C. Dunlop, P. Fratzl, E. V. Skorb, The Role of Titanium Surface Nanostructuring on Preosteoblast Morphology, Adhesion, and Migration, Adv. Healthc. Mater. 6 (2017) 1601244. doi:10.1002/adhm.201601244.

[125] Y. Sun, C.S. Chen, J. Fu, Forcing stem cells to behave: a biophysical perspective of the cellular microenvironment., Annu. Rev. Biophys. 41 (2012) 519–42. doi:10.1146/annurev-biophys-042910-155306.

[126] H.T. Aiyelabegan, E. Sadroddiny, Fundamentals of protein and cell interactions in biomaterials, Biomed. Pharmacother. 88 (2017) 956–970. doi:10.1016/J.BIOPHA.2017.01.136.

[127] M.D. Shoulders, R.T. Raines, Collagen Structure and Stability, Annu Rev Biochem. 78 (2010) 929–958. doi:10.1146/annurev.biochem.77.032207.120833.COLLAGEN.

[128] R. Müller, J. Abke, E. Schnell, D. Scharnweber, R. Kujat, C. Englert, D. Taheri, M. Nerlich, P. Angele, Influence of surface pretreatment of titanium- and cobalt-based biomaterials on covalent immobilization of fibrillar collagen, Biomaterials. 27 (2006) 4059–4068. doi:10.1016/j.biomaterials.2006.03.019.

[129] S. Rammelt, E. Schulze, R. Bernhardt, U. Hanisch, D. Scharnweber, H. Worch, H. Zwipp, A. Biewener, Coating of titanium implants with type-I collagen, J. Orthop. Res. 22 (2004) 1025–1034.

[130] D.G. Costa, E.P. Ferraz, R.P.F. Abuna, P.T. De Oliveira, M. Morra, M.M. Beloti, A.L. Rosa, The effect of collagen coating on titanium with nanotopography on in vitro osteogenesis, J. Biomed. Mater. Res. - Part A. (2017) 2783–2788. doi:10.1002/jbm.a.36140.

[131] R.W. Loo, J.B. Goh, C.C.H. Cheng, N. Su, M.C. Goh, In vitro Synthesis of Native , Fibrous Long Spacing and Segmental Long Spacing Collagen, (2012). doi:10.3791/4417.

[132] B. De Campos Vidal, M.L.S. Mello, Collagen type I amide I band infrared spectroscopy, Micron. 42 (2011) 283–289. doi:10.1016/j.micron.2010.09.010.

[133] K. Belbachir, R. Noreen, G. Gouspillou, C. Petibois, Collagen types analysis and differentiation by FTIR spectroscopy, Anal. Bioanal. Chem. 395 (2009) 829–837. doi:10.1007/s00216-009-3019-y.

[134] M. Habibi, A. Rahimzadeh, M. Eslamian, On dewetting of thin films due to crystallization (crystallization dewetting), Eur. Phys. J. E. 39 (2016). doi:10.1140/epje/i2016-16030-9.

[135] J.D. Harvey Lodish, Arnold Berk, S Lawrence Zipursky, Paul Matsudaira, David Baltimore, Collagen: The Fibrous Proteins of the Matrix, in: Mol. Cell Biol., 4th ed., New York: W. H. Freeman, 2000.

[136] A.H. Yusop, A.A. Bakir, N.A. Shaharom, M.R. Abdul Kadir, H. Hermawan, Porous biodegradable metals for hard tissue scaffolds: A review, Int. J. Biomater. 2012 (2012). doi:10.1155/2012/641430.

[137] C. Gao, Y. Deng, P. Feng, Z. Mao, P. Li, B. Yang, J. Deng, Y. Cao, C. Shuai, S. Peng, C. Gao, Y. Deng, P. Feng, Z. Mao, P. Li, B. Yang, J. Deng, Y. Cao, C. Shuai, S. Peng, Current Progress in Bioactive Ceramic Scaffolds for Bone Repair and Regeneration, Int. J. Mol. Sci. 15 (2014) 4714–4732. doi:10.3390/ijms15034714.

[138] S.B. Goodman, Wear particles, periprosthetic osteolysis and the immune system., Biomaterials. 28 (2007) 5044–8. doi:10.1016/j.biomaterials.2007.06.035.